Finite element study of flow kinematics and mixing behaviors in granular mixers

Liang Bai

Doctor of Philosophy

A thesis submitted for the degree of Doctor of Philosophy

at Monash University in 2018

Chemical Engineering

Copyright notice

Finite element study of flow kinematics and mixing behaviors in granular mixers

Liang Bai
Monash University , 2018

Supervisor: Prof. Aibing Yu

Abstract

Granular flow and mixing is an important research area which has attracted extensive attentions for more than half a century. The granular mixing has a wide range of applications in industries such as pharmaceutical, food, and cosmetics industries. Developing methodology to predict precisely particle behaviors in granular flow and mixing is of great importance to engineering projects across industries. Currently, the prevailing and full-fledged numerical technique for this purpose is discrete element method (DEM). Although its validation is beyond doubt, it has a sever limitation in computational efficiency. To overcome this obstacle, one promising way is establishing a continuum model that can capture the bulk behaviours of granular material. The finite element method (FEM) based on elastoplastic theory is one of such approach having many desirable advantages.

This thesis aims to utilise this Eulerian FEM approach to establish a continuum model of granular mixing and apply the model to study various mixers such as rotating drums and high shear mixers. It is demonstrated that the Eulerian approach, superior to the traditional Lagrangian method, can overcome the mesh distortion during the process of granular flow. Most features of particle mixing are captured qualitatively and quantitatively. In the first part of this study, a granulator with a complex geometry (bladed-mixer) was used to test the Eulerian FEM validation of flow model. Flow patterns, velocity statistical distributions and mixing pattern evolution derived from FEM are highly consistent with the results from the positron emission particle tracking (PEPT) experiment and the discrete element method (DEM) simulations. The convection mixing model was introduced in the first part of primary study. By this model we find convection plays a dominant rule in the granular mixing process in the bladed mixer. However, diffusion, as an important mechanism to mixing should not be neglected. In the second part of the study, the diffusion mechanism is added to the FEM model via an operator splitting method, by which more convincing and quantitatively accurate results are generated and validated with the DEM results. It is further found that diffusion has a positive effect on accelerating the mixing progress by parametric studies. In the third part of study, mixing with different material properties was focused. Segregation is the main feature in the different-particle mixing process. In order to manifest this feature, two mechanisms (percolation and Cahn-Hilliard equation) representing the segregation of different-sized particles were introduced to the FEM mixing model. The FEM segregation model successfully reproduced some main traditional features in a rotating drum such as the core formation in radial segregation and band formation in the axial direction. In the final part, a general 3D FEM convection-diffusion-segregation mixing model was established and verified in a commercial mixer, Mipro. A wider range of parameters concerning operation and material property were studied in this component. It was demonstrated that the FEM mixing model is strictly validated and a promising way to study a variety of complex granular flow and mixing phenomena in industries.

Finite element study of flow kinematics and mixing behaviors in granular mixers

Declaration

This thesis contains no material which has been accepted for the award of any other degree or diploma at any university or equivalent institution and that, to the best of my knowledge and belief, this thesis contains no material previously published or written by another person, except where due reference is made in the text of the thesis.

Signature: [redacted]

Print Name: Liang Bai

Date: July 28, 2018

Acknowledgments

I would like to express my genuine gratitude to the members in the Lab for Simulation and Modelling of Particulate Systems (SIMPAS) who helped to make this possible. It is not an individual honor but a group's effort to complete the PHD project. I am grateful to my supervisor, Professor Aibing Yu. His professional guidance inspired and enlightened me to make the right choice of research topic. He was always there and encouraged me to continue my project when I felt confused and deeply lost. I was touched by his passion, perseverance and faith on scientific research. I am also grateful to my co-supervisor, Dr. Qijun Zheng for his help and guidance in numerical techniques and suggestions on problem solving. I especially thank Dr. Ruiping Zou who paid close attention to the progress of my work. It has been an incredible journey of self-discovery, and I love every last one of you...

Liang Bai

Monash University

July 2018

Contents

List of Tables

List of Figures

Chapter 1

Introduction

Mixing of particles from initial separate phases into a homogeneous phase is an important process in pharmaceutical, food, cosmetics, and powder metallurgical industries and has been an open area of research for decades. The mixing process is complex and most problems are cracked on an ad hoc basis by engineers (Ottino and Khakhar, 2000) before. The general three mixing mechanisms were attempted to propose based on analogies with fluid mixing (Bridgwater, 2012). “Convection” is highly correlated to flow. It refers to the movement of particles in clumps from one location to elsewhere in mixers. “Diffusion” describes the penetration of different materials to each other’s territory. It is mainly caused by frequent collisions between particles. “Shear” describes the mixing phenomenon at the two materials’ interfacial areas which are usually extended by large shear forces. Of the three mixing mechanisms, convection is commonly important and always play a dominant role in most mixing processes. The study of particles’ flow behaviour is fundamentally important, since the movement of particle groups is an essential factor in accelerating the mixing progress. Previous works on this topic were commonly based on the experiments and numerical simulations of discrete element models (DEM), but neither methods can be satisfactorily applied in industrial sectors. Experiments can be costly and erroneous while DEM is often limited by the computational power when treating billions of particles, which is recognised as the scale-up issue (Chandratilleke et al., 2010; Nguyen et al., 2014). It can be solved either by hardware upgrade or theoretical innovation. This thesis focuses on a new continuum theory which treats particle flow as strange fluid with special characterizations. Granular flow is complex since even within a simple geometry, granular systems can undergo a dual-behavior or tri-behavior process. Three distinctive regions can be recognised: a solid region at the bottom of the pile in which grains do not move or creep very slowly, a liquid region in which a dense layer flows, and a gaseous region in which the beads bounce in all directions creating a dilute chaotic medium. The gas phase can be modelled by the kinetic theory of granular flow (KTGF), where collisions between particles are treated as binary collisions in an ideal gas. This method coupled with frictional stress model can be used to simulate particle flow in different regions of high shear mixers (Darelius et al., 2008a; Ng et al., 2009; Khalilitehrani et al., 2013, 2014, 2015; Nguyen et al., 2014). The case of flow in dense phase is more complicated. Particles usually move in groups and chunks, exhibiting a collective and dual behaviour of mixed solid and liquid. Granular flow in the dense region can be regarded as continuum flow with elesto-plastic characteristics, which has been demonstrated with different constitutive laws and under different geometric circumstances such as pressure dip in a hopper flow (Ai et al., 2013), granular eddies in a chute flow (Kamrin, 2010), and JiangLiu granular elasticity law (Jiang and Liu, 2003). Mohr-Coulomb plasticity was the simplest model widely used in granular materials for industrial purposes. However, its shortcomings were illustrated by some publications (Kamrin, 2010). One disadvantage is the model attributes most of characteristics of granular matter yield condition into a single internal friction angle. In order to manifest some specific features of granular flows, a series of models with various constitutive laws were established (Jop et al., 2006; Henann and Kamrin, 2013; Kamrin and Koval, 2012; Bouzid et al., 2013). However, it is less convincing to add extra degrees of freedom and parameters into the theory frame, because most physical hypotheses introduced stay at the phenomenology level, which is lack of physical insight and first principle based calculations. It may hinder the seeking of the real mechanism behind observed granular phenomena and makes the extra added constitutive laws unnecessarily redundant. Recent investigations indicated that using the Mohr-Coulomb plasticity model to describe granular flow can be valid with the numerical calculation technique of Eulerian finite element method (FEM) (Zheng and Yu, 2014). The Eulerian method overcomes the mesh distortion brought about by the traditional Lagrangian method. Its validation has been tested by studies in various geometries (Zheng and Yu, 2015a,b; Hashemnia and Spelt, 2015). The method is a breakthrough and promising to study granular flows in arbitrary complex geometries. The study of mixing with this method has never been tried by researchers before. In hope of finding a general and effective 3D mixing model based on such the continuum approach, the thesis structure is created based on the Eurerian FEM and the three mixing mechanisms.

Chapter 2 gives a summary of literature survey on the academic histories of study on particle mixing. Particular attention is given to mixing mechanisms, the types of mixers, numerical simulation methods which include molecular dynamics and continuum approaches, and typical examples on the mixing process in the mixers with different geometries.

In Chapter 3, the cylindrical bladed mixer (CBM), owing to its high shear rate and complex flow behaviours, is considered here with focus on the solid flow field and convective mixing. The method is verified by comparing features of the solids flow reproduced by FEM with the results generated by DEM. Many features of solid flow such as the formation of heaps, the recirculating flow around blades and the spatial distributions of velocities are well reproduced by FEM model. However, due to the lack of a physical dispersion law, the simulated mixing index depends largely on the size of computational mesh and thus is only of qualitative implication at present. While much work needs to be done in future, the FEM approach allows considering the general solid flow and convective mixing in large-scale mixers and can serve as a good basis for an ultimately predictive capacity of particle mixing.

In Chapter 4, in order to overcome the problems of absence of diffusion, an operator splitting method is used to couple the diffusion term in form of second order partial differential equation to the convection mixing dynamics. The relationship between diffusivity and shear rate $D = \chi\dot{\gamma}d^2$ is used to determine the diffusivity at a local area. The result is tested by comparison with DEM in a rotating drum. The mesh size dependency on mixing index evolution can be neglected when it reduced under a certain threshold. Parametric studies are carried out concerning the effects of filling levels and internal friction angles on the mixing process with different diffusion coefficients. It is found that diffusion has a positive influence on the enhancing the effects of those parameters. The axial diffusion mainly caused by self diffusion resulting from frequent collisions between particles is also studied by the diffusion model. The axial diffusivity is much smaller than the radial diffusivity which is confirmed by comparing results with DEM. Because the shear rate along the axial direction is almost negligible, diffusion can take more time to make the whole mixing complete than the radial mixing process.

In Chapter 5, focuses are placed on the mixing process with different materials. Segregation is the prominent phenomenon which is complicated for its outstanding mechanism and has interested researchers for several decades. In this chapter, we only study the phenomenon of size segregation in a rotating tumbler. Two mechanisms concerning percolation and spinodal decomposition are added to the earlier mixing model by the operator splitting method. The core formation in the radial segregation and band formation in the axial segregation are successfully reproduced by this approach. However, we only arrived at the qualitative agreement level. For the percolation model, the number of stripes and the band width of large particles can not match the experiment results quantitatively. For the spinodal decomposition model, although the agreement of quantitative surface profile has been reached, it produces nonphysical and undesired results which can not be observed in experiments. More work on the development of segregation model still needs to be done in the future research.

In Chapter 6, parametric studies on a wide range of operational properties are carried out in a three-bladed commercial mixer, Mipro. The 3D convection-diffusion-segregation mixing model is applied in this component. The effects of velocity and stress with different blade speeds, blade rake angles on mixing indexes and statistical distributions are mainly studied. The percolation model is able to reproduce the segregation pattern where sediment of small particles is observed in the inner and bottom region while large particles get together in the top and outer region. It is predicted that the 3D convection-diffusion-segregation mixing model is a promising continuum approach to describe the granular flow and mixing in the future studies and to be applied in industry.

Chapter 7 gives a final summary of investigations and results in the thesis and proposes possible future research and outlook.

Chapter 2

Literature Review

2.1 Introduction

The process of granular mixing is ubiquitous in a variety of industries from pharmaceutical tablets manufacture to blending cosmetic materials with different properties. However, the knowledge of the particle flow and mixing behaviour is quite limited in the process engineering, because granular material has never been a simple subject to investigate. Even in a simple geometry container like hopper or a simple particulate process like sand-pile formation, granular system can show dual-behavior or tri-behaviors. Fig2.1 shows a typical granular flow in a sand pile formation. Usually, Three distinctive regions can be observed: a solid region under the pile in which grains do not move or creep very slowly, a liquid region in which a dense layer flows, and a gaseous region in which the beads bounce in all directions creating a dilute chaotic phenomenon.

The implementation of experimental study has been proven difficult. More emphasises have been put on the simulations of granular flows. Mixing studies provide a useful tool to study and understand granular flows, chances are that mixing flows are able to generate a large variety of patterns and structures, which can be visualized and recognized as a means to track particles. Meanwhile, particle mixing has a large scale of practical implications in a multitude of industry processes such as pharmaceutical industry, food industry, cosmetic industry, product manufacture, building materials industry.

Generally, mixing describes the process from a separate original state to a final homogeneous state. Sometimes mixing process can perform in an opposite way, i.e. segregation. There have been a series of works focusing on granular mixing in various experimental

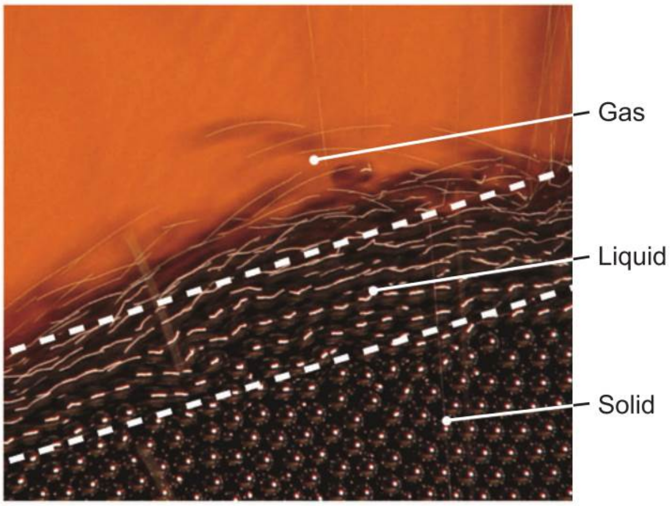

Figure 2.1: An illustration of the solid, liquid, and gas flow regimes obtained by pouring steel beads on a pile.

containers including drums (Yang et al., 2003, 2008; Cleary et al., 1998), high shear mixer (Chandratilleke et al., 2009, 2010, 2012), ribbon mixer (Musha et al., 2013), and shear cell (Wang et al., 2013, 2012). In their works, the discrete element method based on Newton's second law was proved an efficient and accurate way of tracking particle to investigate the mixing process. However, the computational power of today allows the flow of less than a million particles to be modelled using DEM, whereas billions of particles are present in the real mixing process (Goldschmidt et al., 2004). So the limitation of computational power makes it not applicable for large-scale processes. Another approach for modelling multi-phase flows is the Eulerian-Eulerian approach where the particles are not tracked, but instead are treated as a continuous flowing medium with fluid constitutive laws derived from closure models. In dilute region, particle collisions are viewed as molecules collisions in an ideal gas, which is the basically theoretical assumption of the kinetic theory of granular flow (KTGF) (Lun et al., 1984; Ding and Gidaspow, 1990; Gidaspow, 1994), a promising model in the dilute region. As for denser flows, e.g. hopper flow, where particles are in frequent contact and move in a group manner, frictional stress is added to the computing model of KTGF (Ng et al., 2009; Srivastava and Sundaresan, 2003; Savage et al., 1983). Another approach regarding the visco-plastic rheology model developed by Jop et al (Jop et al., 2006) was adopted to investigate granular flows in a disc impeller granulator (Khalilitehrani et al., 2013). However, in all these models above for dense region, discrepancies were still observed when measuring particle velocities. The reason of failing to keep the simulation data consistent with experiments lies in that the transition regime between solid and liquid is always neglected. Assumptions of constant volume fraction was also invalid. In the mean time, the elasto-plastic theory originally dealing with problems in civil engineering achieved a success in granular flows in hoppers (Ai et al., 2013), chute (Kamrin, 2010), and even shear cell (Henann and Kamrin, 2013). The basic idea is based on the Mohr-Coulomb or Drucker-Prager model using finite element method for simulations. However, the method they used is under the theory frame of Lagrangian method, which hardly treat the problem of flows since high mesh distortion is inevitable during the computational calculation. Recently, a new method based on Eulerian approach has been proposed (Zheng and Yu, 2014), which successfully describe the characteristic phenomenon of granular flow that continuum methods failed to obtain before. In this project, we hope to develop the continuum approach proposed by (Zheng and Yu, 2014) and apply the method in various mixers such as drums, high shear mixers and even couette cells.

2.2 Granular Mixing

2.2.1 Mixing mechanisms

Before the discussion of mixers classification, it is useful to introduce the mixing mechanisms, based on which the mixers can be identified and created more reasonably. Basically, there are three kinds of mechanisms in the mixing processes (Bridgwater, 2012): convection mixing, shearing mixing, and diffusion mixing.

Mixing by convection

Driven by the effect of advection, particles in the form of clusters or clumps move or shifted in a group manner to other locations in the mixer, the sizes of chunk are reduced when the process goes on. This method is able to mix particles more efficiently and uniformly to improve homogeneity. A typical example is the flowing mixing in a bladed mixer.

Mixing by shearing

This mechanism is related to convection. During the convective movement, there is a narrow region connecting two kinds of particles called slip zone in which particles get mixed by the effect of momentum exchanges because of the high velocity gradients. Slipping plays an important role in the mixing process since it extends the contact areas where particles are blended in a high efficiency. The breakdown of particle planes promote the mixing at a semi-microscopic scale.

Mixing by diffusion

In the contact area, two group of particles penetrate into the regions of each other by frequent random collisions, which is the main reason for the driven force of diffusion mixing. It is evident that the rate of mixing caused by diffusion is much slower than the two mechanisms aforementioned. However, at a microscopic scale, diffusion is important to the mixing process in certain mixers such as ribbon where a homogeneous phase can be reached in a short time.

2.2.2 Different types of mixers

All types of mixers can be basically classified into two categories based on mechanisms listed above. The first group is characterised by the rotation of external shell. Shear and diffusion are the dominant mixing mechanisms for those mixers which include (Fig.2.2):

The cylindrical drum The vessel rotation gives rise to both radial and axial mixing. These mixers are frequently used for free-flowing or slightly cohesive materials but are less suitable for particles which agglomerate.

The off-centre drum One end of the cylindrical mixer rises and falls with respect to the other. The idea is to improve mixing by making material slop backwards and forwards in the axial direction.

The double cone It is made from two parts, each of which is part of a conical section, the two being joined at the base of the cones. The action rolls and folds material. A bar or blade can be fixed to the axis of rotation to serve as an internal breaker for agglomerates.

The V mixer It has two arms forming a V and has many of the features of the double cone mixer. However, there is a further action of division of material into the two arms followed by inter-meshing when the two bodies of material recombine.

Tote mixers They are in the form of a storage vessel which is sealed, mounted on an axis and then rotated. These may be with an upper rectangular section, or with a circular upper section. This axis can be horizontal or can be inclined at an arbitrary angle. The idea is to use asymmetry to cause more irregular flow patterns to break up the flow in the hope that mixing improves.

In the second main class of mixer, the shell is stationary but there is an internal rotor or rotors fitted with blades causing agitation. Examples of this type are:

The centrifugal mixer with a horizontal axis At low speeds, the mixer contents are pushed circumferentially and then are displaced axially as the blade moves out of the material. At high speeds, the material is centrifuged. The range of materials that can be processed is broad. The mixer can be hard to clean.

The centrifugal mixer with a vertical axis At low speeds, the blades push the contents around the mixer with a surface wave of material being associated with each blade. At high speeds the contents form a toroid next to the wall. This mixer is particularly effective for the formation and treatment of agglomerates. Cleaning can be relatively easy.

Ribbon mixer This mixer can have one or two helical screws as blades. In the two-screw type, one screw pushes in one axial direction close to the centre and simultaneously the other screw pushes in the opposite direction close to the wall. Material is rolled, folded, reversed in direction and radially displaced. The screw makes it easy to push product to an exit although it can make cleaning more difficult. The mixer can be used for a wide range of materials from dry powders to pastes. Radial mixing is good, axial mixing is less so. The ribbon mixer is a good choice for aerating materials.

Planetary mixer Here a bed of material is rotated about a vertical axis, being brought into the zone of action of a mixing blade rotating at a high speed about an offset vertical axis. The mechanism is convection and shear. It is not well suited to adhesive or very cohesive materials.

The draught tube and screw mixer (Fig.2.3 (a)). Here material is conveyed to the free surface under the action of the vertical screw contained within a tube. The material then falls down the free surface and is recycled back to the base of the screw. The recirculation time is a function of radial position in the annulus and thus, overall, axial mixing occurs. The free surface adds diffusion to the mechanisms.

Orbiting screw mixer (Fig.2.3 (b)). These mixers are in the form of an inverted cone with a screw attached at the base of the cone and are generally confined to batch operation. The screw rotates about its own axis while at the same time processing about the vertical axis of the cone. Material is conveyed upwards in the screw with a general flow downwards over the cross-section of the mixer. At the top the screw acts to distribute material onto the surface. The mechanisms here are convection and diffusion. Segregation when using free-flowing materials can be reduced by running the screw during discharge.

2.2.3 Mixing index

Types of mixing state

The earliest discussion of the states of a granular mixture can be attributed to Lacey (Lacey and P.M.C., 1954), where he illustrated the likely arrangements of particles at the end of an ideal mixing process using schematics as shown in Fig.2.4. Fig.2.4 (a) demonstrates the perfect mixture defined as a mixture in which the probability of finding a particle of a constituent of the mixture is the same for all points in the mixture. These probabilities will be different if the mixture is not well mixed. Fig.2.4 (b) demonstrates the random mixing state, in which the probability of finding a particle of one component is not constant through out the mixture. A further description can be illustrated mathematically. There are various sampling methods for characterising the state of a given mixture. One common practice involves repeatedly taking random samples of a fixed size and shape from the mixture with replacement, and recording the pro-portion of black particles within each sample; given that a sufficient number of samples are taken, the distribution of these sample proportions (denoted using the random variable X_{SP}) will characterise the state of the mixture. Alternatively, one can divide the entire domain of the mixture into a finite number of fixed cells, with the number of black particles in each cell counted to give cell counts (denoted using the random variable X_{CC}); the state of the mixture can also be described by the distribution of these cell counts. This approach is particularly

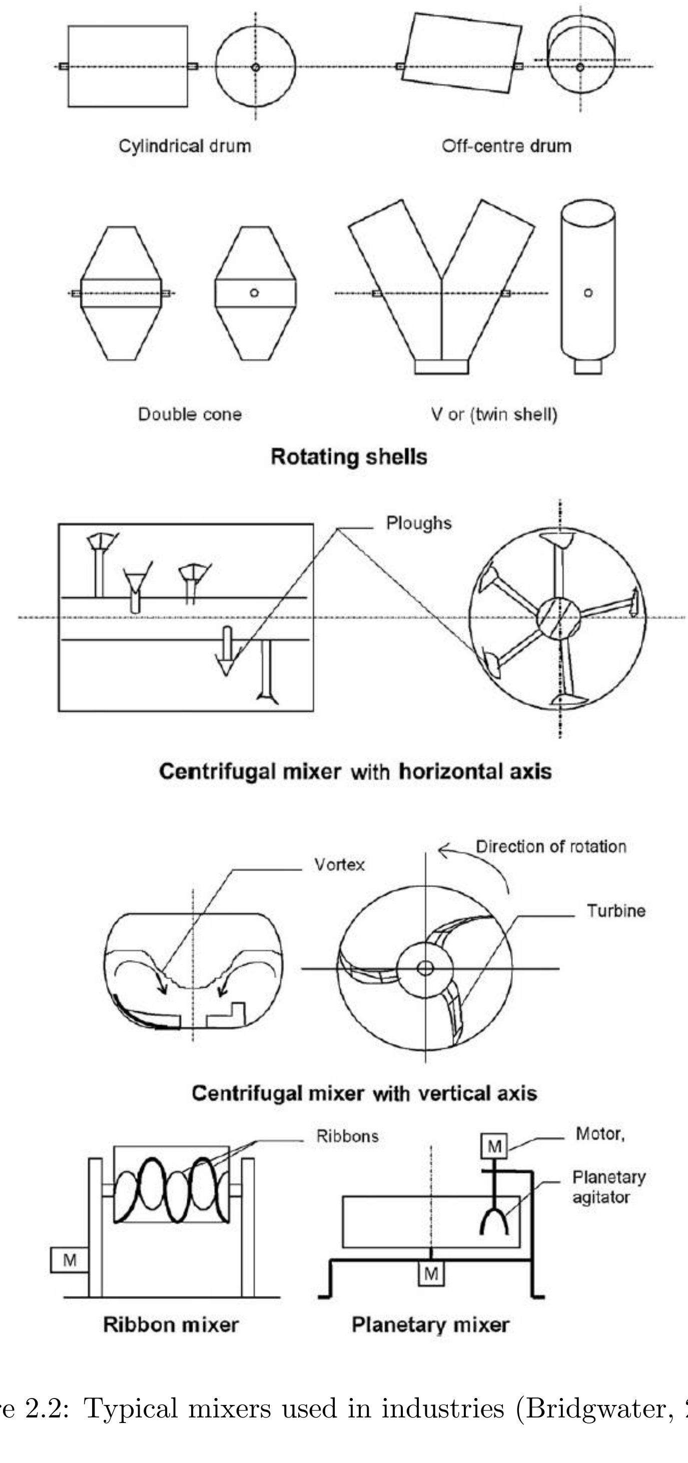

Figure 2.2: Typical mixers used in industries (Bridgwater, 2012).

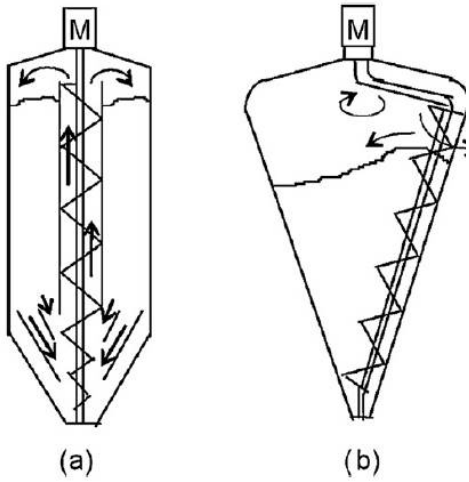

Figure 2.3: (a) Draught tube screw mixer and (b) Nauta mixer with orbiting screw (Bridgwater, 2012).

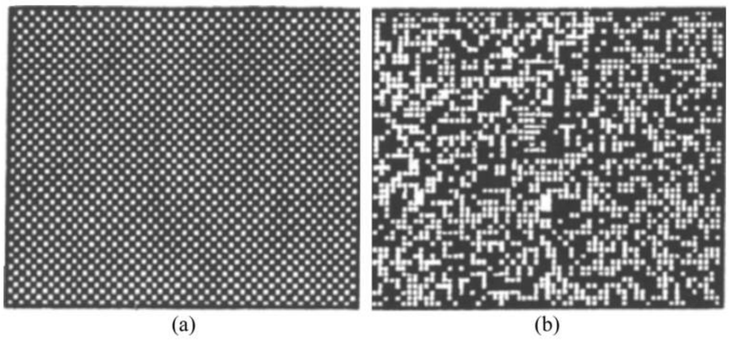

Figure 2.4: Pictorial representations of the likely arrangements of particles in a granular mixture at the end of an ideal mixing operation.

straightforward if the cells all contain an equal number of particles. Other techniques include, for instance, counting the contact points between different types of particles.

The perfectly ordered state

In Fig.2.4 (a), we may define the perfectly ordered state using the probability statement

$$Pr(X_{SP} = P) = 1$$

which says that the sample proportion is always equal to the overall proportion of black particles in the mixture; that is to say, the outcome of random sampling is deterministic. As (M.Poux et al., 1991) have noted, the perfectly ordered state is only attainable in very special cases, and for the mixing of non-interacting particles that are only distinguishable

(a) $P = 0.5$ (b) $P = 0.5$ (c) $P = 0.3$

Figure 2.5: Instances of the randomly mixed state represented on a 2D lattice

by colour, the perfectly ordered state does not represent the final state of the mixture at the steady state.

The randomly mixed state

Non-interacting particles that are identical except colour at the end of an ideal mixing operation will reach the randomly mixed state. On a 2D lattice, this state is represented by Fig.2.5. These randomly mixed states can be generated by completely randomising the arrangement of black and white particles on the lattice, where the number of each type is set by a prescribed value of the overall proportion of black particles in the mixture.
Unlike the perfectly ordered state, random samples taken from a granular mixture in the randomly mixed state will likely contain a different number of black particles each. Given a sample size of n, the distribution of sample proportions is approximated by

$$Pr(X_{SP} = x) = C_n^{nx} P^{nx} (1-P)^{n(1-x)} for x = 0, \frac{1}{n}, \frac{2}{n}, ..., 1$$

where C_a^b denotes a binomial coefficient. The mean and variance of this distribution can be shown to be P and P(1-P)/n, respectively. Note that the variance of the distribution of sample proportions for the randomly mixed state asymptotically approaches zero in the limit of $n \to \infty$: this implies that the two states become increasingly indistinguishable as the number of particles per sample increases. However, for a granular material, unlike a fluid, there are only a finite number of particles in any sample taken; thus, the perfectly ordered state and the randomly mixed state are indeed two dissimilar states.
Finally, the probability mass function of X_{CC} for the randomly mixed state can be written as

$$Pr(X_{CC} = x) = C_{\frac{N}{b}}^{x} P^x (1-P)^{N/b-x} for x = 0, 1, 2, ..., \frac{N}{b}$$

whose mean and variance are NP/b and NP(1-P)/b, respectively.

Variance of sample proportions; the Lacey index

A large portion of the mixing indices available, especially those found in the early literature, are based on or related to the variance of sample proportions, commonly denoted as s^2. The expected values of the variance of sample proportions for the characteristic states can be derived from appropriate probability distributions. For the completely unmixed state, the expected value of the variance of sample proportions for the completely unmixed state is

$$s_0^2 = E(X_{SP}^2) - [E(X_{SP})]^2 = P(1-P)$$

The variance of randomly mixed state is

$$s_r^2 = \frac{P(1-P)}{n} \tag{2.1}$$

and the perfectly ordered state is given by

$$s_p^2 = 0 \tag{2.2}$$

The well-known Lacey index is defined as

$$M = \frac{s_0^2 - s^2}{s_0^2 - s_r^2} \tag{2.3}$$

Since s_0^2 and s_r^2 are fixed with given P and n, it is useful to think of the Lacey index as a normalised version of the variance of sample proportion. Because the normalisation is based on the completely unmixed and the randomly mixed states, the expected values of the Lacey index for these two states are $M_0 = 0$ and $M_r = 1$, respectively. As the mixture evolves from the completely unmixed state to the randomly mixed state during a typical mixing process, the variance correspondingly decreases from s_0^2 and converges to s_r^2, while the Lacey index increases from zero to unity.

2.2.4 Particle segregation

Particle segregation, a most commonly observed phenomenon in various particle processes in industry, is worth being investigated by researchers. However, particle segregation violates the basic requirement of granular mixing. Particles are supposed to be blended sufficiently in most processes in industry like pharmaceutical industry, food industry, cosmetic industry. Thus, particle segregation should be deeply depressed and avoided during the product generation process.

To begin investigating, several quantities are introduced to described the intensity of segregation. Lacey index:

$$M = \frac{\sigma_0^2 - \sigma^2}{\sigma_0^2 - \sigma_R^2} \tag{2.4}$$

where, σ_0^2 and σ_R^2 are sample variances of fully-segregated and fully-random states respectively, and σ^2 is the sample variance of a mixture at a transition state between the two states reference states.

This index can be regarded as an order parameter in most phase transition process. $M = 1$ stands for most uniform mixture (homogenous and fully-random mixture), while $M = 0$ represents a fully-segregated (order) mixing state. Later, the index was developed by Missiaen:

$$I = \frac{\sigma^2 - \sigma_R^2}{\sigma_0^2 - \sigma_R^2} \tag{2.5}$$

and Yamane:

$$I = \frac{\sigma}{\sigma_0} \tag{2.6}$$

which is more suitable for DEM simulations.

The investigation of particle segregation originates from (Rosato et al., 1987), in which a Monte-Carlo method is proposed to investigate the "Brazil nuts" segregation phenomenon. Recent investigation regards it as a phase transition from a disorder initial configuration to an order final state. Pedro M.Reis and Tom Mullin (Reis and Mullin,

2002) set up an experimental study of patterned segregation in a horizontally shaken shallow layer of a binary mixture of dry particles. An order parameter was introduced and the segregation can be regraded as a critical phenomenon with the critical exponent decided.

Factors influencing segregation

Segregation can be influenced by physical properties of particles, such as size, density, or shape. Changing the mixing operation can also change the segregation results. vibration, gravity, shear, or rotation lead to different final configurations. Mixers such as hoppers, drums, ribbon mixers and chutes are also considered as other significant factors to influence the mixing process. Mixing in various mixers is still under study in many research works.

2.3 Numerical Simulation Models

2.3.1 Molecular Dynamics

A landscape of Molecular Dynamics (MD)

The main ingredients of an MD simulation are basically threefold:

- A model is needed for the interaction between the system constituents (e.g. atoms or molecules).
- Time integration is required to advance the particle trajectories (positions and velocities) from time t to t+Δt. Alternatively, one may want to solve a stability problem which in an atomistic system requires an algorithm to relax the atomic coordinates to positions of vanishing forces.
- An ensemble has to be chosen, for which boundary conditions and thermodynamic quantities like temperature, pressure or the number of particles is controlled.

Force calculation

Forces are derived from the potential energy U that depends on the positions of all atoms. The description for the calculation of the energy can be based on different physical approximations. The force acting on an atom i is given by taking the derivative of the potential energy with respect to the position vector $\mathbf{x}_i$ of atom i

$$\mathbf{f}_i = -\frac{dU(x)}{d\mathbf{x}_i} \tag{2.7}$$

where $\mathbf{x}$ denotes the coordinates of all atoms. Once the force vector $\mathbf{f}_i$ acting on all atoms is known, the Newtonian equation of motion

$$\mathbf{f}_i = m_i \frac{d^2 x_i}{dt^2} \tag{2.8}$$

can be integrated in time t to yield the motion of the atoms in space. The mass of the atom is given by m_i.

Integrating the Equations of Motion

Equation [2.8] constitutes a set of second-order ordinary differential equations (ODEs), which can be strongly nonlinear. By converting them to first-order ODEs in the 6N-dimensional space, general numerical algorithms for solving ODEs such as the Runge-Kutta method could be applied. However, these general methods are rarely used in practice, because the existence of a Hamiltonian allows for much simpler and even more accurate integration algorithms. To represent other thermodynamic ensembles than the micro-canonical ensemble for which Equation [2.8] can be integrated directly, requires that Equation [2.8] is modified to create a dynamics in phase space that has the desired distribution density of e.g. a canonical or a grand-canonical ensemble. The time-average of a single-point operator on such a trajectory then approaches the thermodynamic average. An integrator serves the purpose of propagating particle positions and velocities over small time increments Δt. The time step Δt has to be chosen such that the thermal oscillations of the atoms around their equilibrium positions are resolved in time. A typical frequency of this oscillation is the Debye frequency $v_D = c_t/a$, where c_t is the speed of transverse sound waves and a is the lattice parameter. A typical value for metals is $v_D = 10^{13}$ Hz. This implies that the typical time step for MD simulations has to be on the order of femtoseconds (10^{-15} s), which generally limits the method to simulations of fast processes such as brittle fracture or high-strain-rate plastic deformation.

Verlet algorithm

Assuming that the $x^{3N}(t)$ trajectories are smooth, one may perform a third-order Tylor expansion of the positions $x_i(t_0)$ forward $x_i(t_0 + \Delta t)$ and backward $x_i(t_0 - \Delta t)$ in time; their sum yields

$$\mathbf{x}_i(t_0 + \Delta t) + \mathbf{x}_i(t_0 - \Delta t) = 2\mathbf{x}_i(t_0) + \ddot{\mathbf{x}}_i(t_0)(\Delta t)^2 + o((\Delta t)^4) \tag{2.9}$$

Since $\ddot{\mathbf{x}}_i(t_0 + \Delta t) = \mathbf{f}_i(t_0)/m_i$ can be evaluated given the atomic positions at $t = t_0$, $x^{3N}(t + \Delta t)$ in turn may be approximated by,

$$\mathbf{x}_i(t_0 + \Delta t) + \mathbf{x}_i(t_0 - \Delta t) = 2\mathbf{x}_i(t_0) + \frac{1}{m}\mathbf{f}_i(t_0)(\Delta t)^2 + o((\Delta t)^4) \tag{2.10}$$

Neglecting the $o((\Delta t)^4$ term, we obtain a recursion formula to compute $x^{3N}(t + \Delta t)$. Although velocities are not needed in the recursion, they are often calculated since they are required for analysis of ensemble properties. They can be approximated by

$$\mathbf{v}_i(t_0) = \dot{\mathbf{x}}_i = \frac{1}{2\Delta t}[\mathbf{x}_i(t_0 + \Delta t) - \mathbf{x}_i(t_0 - \Delta t)] + o((\Delta t)^2) \tag{2.11}$$

This algorithm is not only one of the simplest, but also a good choice in general. It is fast, but not particularly accurate for long time steps, such that the forces on all particles must be computed rather frequently. It requires about as little memory as is at all possible. This is useful when very large systems are simulated.

Velocity-Verlet algorithm

It starts with $\mathbf{v}^{3N}(t_0)$ and $\mathbf{x}^{3N}(t_0)$. One then evaluates

$$\mathbf{x}_i(t_0 + \Delta t) = \mathbf{x}_i(t_0) + \frac{1}{2m}\mathbf{f}_i(t_0)(\Delta t)^2 + o((\Delta t)^3) \tag{2.12}$$

With $f^{3N}(t_0 + \Delta t)$ evaluated from $\mathbf{x}_i(t_0 + \Delta t)$ one gets

$$\mathbf{v}_i(t_0 + \Delta t) = \mathbf{v}_i(t_0) + \frac{1}{2m}[\mathbf{f}_i(t_0) + \mathbf{f}_i(t_0 + \Delta t)]\Delta t + o((\Delta t)^3) \tag{2.13}$$

and has advanced by one step. This algorithm requires a little more computing but is very popular since it gives $\mathbf{v}^{3N}$ and $\mathbf{x}^{3N}$simultaneously.

Leap-frog algorithm

In the leap-frog algorithm, position and velocities are calculated with the same accuracies but are offset by $\Delta t/2$. It starts with $\mathbf{v}^{3N}(t_0 - \Delta t/2)$ and $\mathbf{x}^{3N}(t_0)$. Time integration is then first done on $\mathbf{v}$.

$$\mathbf{v}_i(t_0 + \frac{1}{2}\Delta t) = \mathbf{v}_i(t_0 - \frac{1}{2}\Delta t) + \frac{1}{m}[\mathbf{f}_i(t_0)]\Delta t + o((\Delta t)^3) \tag{2.14}$$

Followed by integration of $\mathbf{x}$,

$$\mathbf{x}_i(t_0 + \Delta t) = \mathbf{x}_i(t_0) + \mathbf{v}_i(t_0 + \frac{1}{2}\Delta t) + o((\Delta t)^3) \tag{2.15}$$

It can be shown that the leap-frog algorithm produces identical trajectories to the Verlet algorithm besides numerical rounding errors. It therefore has similar properties than the Verlet algorithm but of course provides coordinates and velocities at once.

2.3.2 Continuum Methods

DEM is the common approach for the numerical simulation of multiphase particulate flow. One of the advantages is that every motion of single particles can be tracked. However, it is not applicable to large-scale number (billions of particles) of particle system due to the incapability of computer power. This disadvantage has been being improved by application of GPU, which accelerates the work rate of computer. However, it still has a long way to solve the problem. Another way is through continuum approaches, which are based on a series of continuum partial differential equations describing the states and flow of granule particles. Overall, according to different regions, characteristics of particle flows can be described by different frames of continuum theories. In the dilute region, granule flow displays the characteristics of gas. An approach called Kinetic theory based on Boltzmann equation has been widely used in the dilute region. In the dense region, both CFD and FEM are good candidates which have been focused in many research publications.

2.3.3 Kinetic theory of granular flow (KTGF)

KTGF is based on a series expansion solution to a number of statistical moments of the Boltzmann equation (van Beijeren and Ernst, 1979; Montanero et al., 1999; Darelius et al., 2008b). For dilute systems of elastic particles, there are a number of solutions using an expansion around the equilibrium state, represented by a Gaussian particle state distribution function. The KTGF model satisfying mass, momentum, and the fluctuating kinetic energy can be represented as (Nguyen et al., 2014)

$$\begin{aligned} \frac{\partial}{\partial t}(\alpha_s \rho_p) + \nabla \cdot (\alpha_s \rho_p v_i) &= 0 \\ \frac{\partial}{\partial t}(\alpha_s \rho_p v_i) + \nabla \cdot (\alpha_s \rho_p v_i v_j) &= \frac{\partial \tau_{ij}}{\partial x_j} - \alpha_s \nabla P_s \end{aligned}$$

where α_s is the solid volume fraction, ρ_p is the particle density. v is the velocity vector and τ_{ij} is the combined kinetic and collision stress tensor that can be written in the form of Newton's law of viscosity, Eq.(2.16)

$$\tau_{ij} = (\lambda_s - \frac{2}{3}\mu_s)(\nabla \cdot v_i))I_{ij} + 2\mu_s S_{ij} \tag{2.16}$$

where λ_s represents the bulk viscosity and μ_s the shear viscosity. I_{ij} is the identity matrix and S_{ij} is the strain rate tensor. The third statistical moment is in the velocity fluctuations, C, defined as $v_i = U_i + C_i$, where U_i is the mean motion of the particles. The fluctuations are represented by the fluctuating kinetic energy as seen in Eq.(2.17):

$$\frac{\partial}{\partial t}(\alpha_s \rho_s \frac{< C_i^2 >}{3}) + \nabla \cdot (\alpha_s \rho_p v_j \frac{< C_i^2 >}{3}) = (-P_s I_{ij} + \tau_{ij}) : \nabla v_i + \nabla \cdot q - \gamma \tag{2.17}$$

where $<>$ denotes the ensemble average and $T_g = \frac{1}{3} < C_i^2 >$ can be referred to as the granular temperature. The first term on the right hand side is the energy production due to deformation, while γ is the dissipation of energy due to inelastic collisions and P_s is the solid phase pressure given in Eq.(2.22) and Eq.(2.23), respectively. The combined flux of the fluctuating kinetic energy due to collisions and translation is denoted by q and is described by the Fourier's law of heat transfer, Eq.(2.18).

$$q = k \nabla T_g \tag{2.18}$$

In Eq.(2.18), k is the conductivity of the granular temperature. The transport coefficients are then determined by the Chapman-Enskog method. The method determines the coefficients by expressing them as a series expansion, using a small parameter and the grdients of the solved fields (mass, momentum and fluctuating kinetic energy) around a known solution. The solutin used is that of a dilute gas phase in equilibrium. This solution is only valid for low solid volume fractions and instantaneous elastic, or nearly elastic, binary collisions. The expressions used for the transport coeffecients are given by Eqs.(2.19) - (2.20) and include the above-mentioned assumptions.

$$\mu_s = \frac{4}{5}\alpha_s^2\rho_p d_p g_0(1+e_p)\sqrt{\frac{T_g}{\pi}} + \frac{10\rho_s d_p\sqrt{T_g\pi}}{96(1+e_p)g_0}[1+\frac{4}{5}g_0\alpha_s(1+e_p)]^2 \tag{2.19}$$

$$k_s = \frac{150\sqrt{T_g\pi}\rho_p d_p}{384(1+e_p)g_0}[1+\frac{6}{5}\alpha_s g_0(1+e_p)]^2 + \alpha^2\rho_p d_p g_0(1+e_p)\sqrt{\frac{T_g}{\pi}} \tag{2.20}$$

Eq.(2.19) and Eq.(2.20) are from Gidaspow and Ding, where e_p is the binary restitution coefficient and $g_0 = [1-(\alpha_s/\alpha_{s,max})^{1/3}]^{-1}$ is the radial distribution function.

$$\lambda_s = \frac{4}{3}\alpha_s^2\rho_p d_p g_0(1+e_p)\sqrt{\frac{T_g}{\pi}} \tag{2.21}$$

$$\gamma = \frac{12(1-e_p^2)g_0}{d_p\sqrt{\pi}}\alpha_s^2\rho_p T_g^{3/2} \tag{2.22}$$

$$P_s = \alpha_s\rho_p T_g + 2\rho_p\alpha_s^2 g_0(1+e_p)T_g \tag{2.23}$$

The boundary condition used for the granular phase is that derived by Johnson and Jackson. It sets a heat flux at the well as a function of the solid volume fraction, granular temperature and the particle mean velocity, Eq.(2.24).

$$q = (\frac{\pi}{6}\sqrt{3}\phi\frac{\alpha_s}{\alpha_{s,max}}\rho_p g_0\sqrt{T_g}U_i\cdot U_i) - \frac{\pi}{4}\sqrt{3}\frac{\alpha_s}{\alpha_{s,max}}\rho_p g_0 T_g^{3/2}(1+e_w^2) \tag{2.24}$$

2.3.4 Frictional model

Under quasi-static conditions, the frictional sliding causes the particle-particle interaction and the momentum transfer. The frictional viscosity is calculated from a Coulomb-like friction law (Khalilitehrani et al., 2013; Vun et al., 2010).

$$\mu_{friction} = \frac{P_{friction} sin\varphi}{2\sqrt{I_{2D}}}$$

The expression contains the frictional pressure, $P_{friction}$ the second invariant of the stress tensor, I_{2D}, and the material property angle of internal friction, φ. The frictional pressure can be described by:

$$P_{friction} = Fr\frac{(\alpha_s - \alpha_{s,min})^n}{(\alpha_{s,max} - \alpha_s)^p}$$

where Fr, n and p are empirical constants, $\alpha_{s,min}$ is an empirical value indicating when the transition to a quasi-static system starts and $\alpha_{s,max}$ is the maximum packing limit. These properties are then assumed additive with the KTGF results in the transition region according to Eq.(2.25) and Eq.(2.26).

$$\mu_s = \Sigma\mu_{KTGF} + \mu_{friction} \tag{2.25}$$

$$P_s = \Sigma P_{KTGF} + P_{friction} \tag{2.26}$$

2.3.5 Elastoplastic model

DEM simulations of Rycroft et al. (Rycroft et al., 2009; Kamrin, 2010) showed in multiple 3D well-developed flow environments, a dense granular element of width $\sim 5d$ (for $d =$ particle diameter) captures many of the plastic flow properties expected of a representative element. Among neighboring volume elements of this width, the average stress and deformation rate appear to vary smoothly. Within a flowing element, the eigenvectors of the instantaneous space-average Cauchy stress align to a high degree with those of the deformation rate tensor, evidencing the onset of a deterministic relationship between the two fields. Moreover, a predictable dependence of the packing fraction on the pressure and shearing rate emerges at this length-scale.

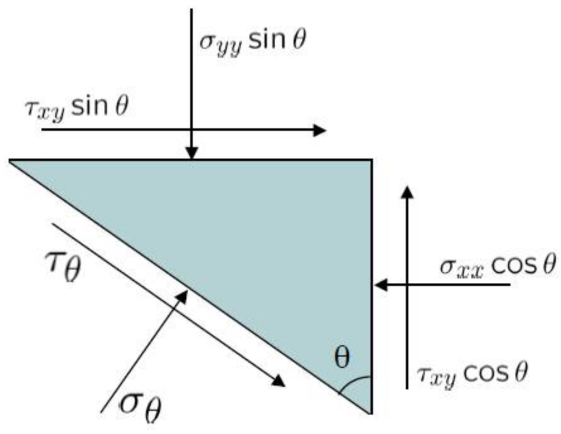

Figure 2.6: Force diagram for a wedge.

Elastic constitutive model

The elastic behavior of both Mohr-Coulomb Elesto-Plastic (MCEP) and Drucker-Prager Elesto-Plastic (DPEP) can be described as the following relationship (Nedderman, 2005):

$$\sigma_{i,j} = D_{ijkl}\epsilon_{kl}$$

where σ_{ij} is the total stress, and ϵ_{kl} the elastic strain. D_{ijkl}, the fourth-order tensor of elasticity, is completely determined by Young's modulus E and Poisson's ratio ν following the isotropic elastic law.

Mohr-Coulomb plastic constitutive relation

Generally, we can demonstrate Mohr-Coulomb plasticity mathematically below (Rao, 2006). If we treat a granular material as an "Ideal Coulomb Material" (ICM), any s-mall amount of material selected (here we choose wedge) can be analysed under the frame of force balance (Fig.2.6). We derive:

$$\sigma_\theta = \frac{1}{2}(\sigma_{xx} + \sigma_{yy}) + \frac{1}{2}(\sigma_{xx} - \sigma_{yy})\cos 2\theta - \tau_{xy}\sin 2\theta \qquad (2.27)$$

$$\tau_\theta = \frac{1}{2}(\sigma_{xx} - \sigma_{yy})\cos 2\theta + \tau_{xy}\cos 2\theta \qquad (2.28)$$

If we define parameters as follows:

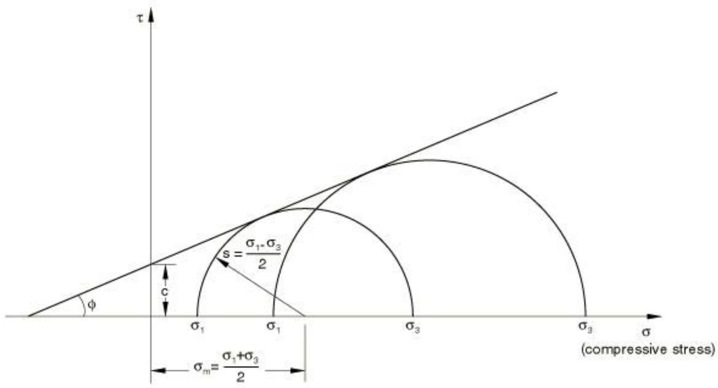

Figure 2.7: Mohr-Coulomb failure criterion.

$$p = \frac{1}{2}(\sigma_{xx} + \sigma_{yy}) \tag{2.29}$$

$$\tan 2\psi = \frac{-2\tau_{xy}}{\sigma_{xx} - \sigma_{yy}} \tag{2.30}$$

$$R = \sqrt{(\frac{\sigma_{xx} - \sigma_{yy}}{2})^2 + \tau_{xy}^2} \tag{2.31}$$

A more simplified and obvious relationship between normal stress and shear stress appears:

$$\sigma_\theta = p + R\cos(2\theta - 2\psi) \tag{2.32}$$

$$\tau_\theta = R\sin(2\theta - 2\psi) \tag{2.33}$$

The derivation above demonstrate that at any plane with certain angle θ, the stress state $(\sigma_\theta, \tau_\theta)$ lies on a circle centered at $(p,\ 0)$ with radius R. The circle is also referred to as "Mohr's Circle" (Fig.2.7).

Mohr-Coulomb plastic yield condition

When it comes to yielding part, the Mohr-Coulomb model assumes the following relation between normal stress and shear stress (2.34):

$$\tau = c - \sigma \tan\phi \tag{2.34}$$

If we consider parametric equations 2.32 and 2.33, 2.34 can be rewritten as:

$$s + \sigma_m \sin\phi - c\cos\phi = 0 \tag{2.35}$$

where

$$s = \frac{1}{2}(\sigma_1 - \sigma_3) \tag{2.36}$$

is half of the difference between the maximum principal stress, σ_1, and the minimum principal stress, σ_3 (and is, therefore, the maximum shear stress),

$$\sigma_m = \frac{1}{2}(\sigma_1 + \sigma_3) \tag{2.37}$$

is the average of the maximum and minimum principal stresses, and ϕ is the friction angle.

For general states of stress the model is more conveniently written in terms of three stress invariants as

$$F = R_{mc}q - p\tan\phi - c \quad = \quad 0$$

where

$$R_{mc} \quad = \quad \frac{1}{\sqrt{3}\cos\phi}\sin(\Theta + \frac{\pi}{3}) + \frac{1}{3}\cos(\Theta + \frac{\pi}{3})\tan\phi$$

ϕ is the slope of the Mohr-Coulomb yield surface in the $p - R_{mc}q$ (Fig.2.8) stress plane, which is commonly referred to as the friction angle of the material and depends on predefined field variables. $p = -\frac{1}{3}\text{trace}(\sigma_{ij})$ is the first invariant of stress representing the equivalent pressure; $q = \sqrt{\frac{3}{2}S_{ij}S_{ij}}$ is the Mises equivalent stress and S_{ij} is the deviatoric stress; ϕ and c are the angles of internal friction and and the cohesion of granular material, respectively. Θ is the deviatoric polar angle defined as $\cos(3\Theta) = (r/q)^3$ where $r = (\frac{9}{2}S_{ji}S_{jk}S_{ki})^{\frac{1}{3}}$ is an invariant measure of deviatoric stress. The friction angle, ϕ, controls the shape of the yield surface in the deviatoric place (Fig.2.8). The friction angle range is $0° \leq \phi < 90°$. In the case of $\phi = 0°$ the Mohr-Coulomb model reduces to the pressure-independent Tresca model with a perfectly hexagonal deviatoric section. In the case of $\phi = 90°$ the Mohr-Coulomb model reduces to the "tension cutoff" Rankine model with a triangular deviatoric section and $R_{mc} = \infty$.

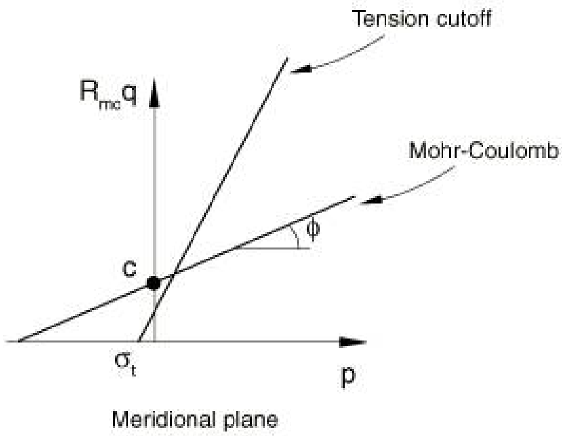

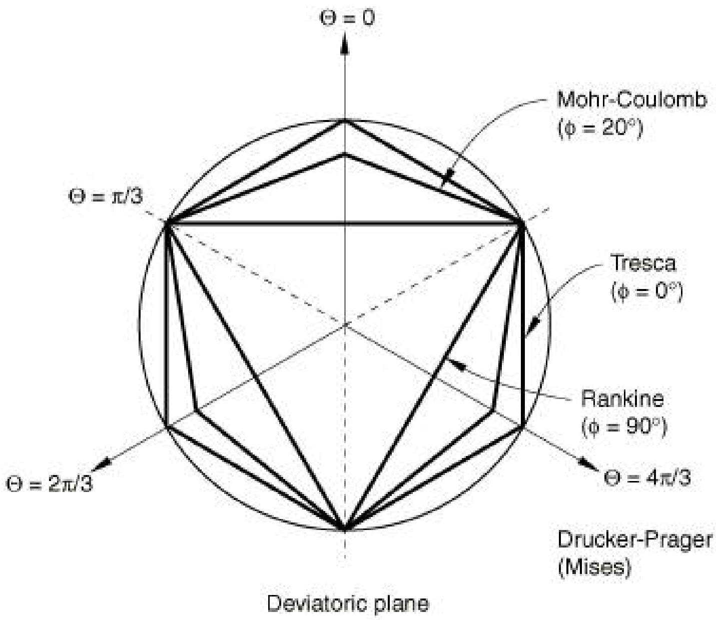

Figure 2.8: Mohr-Coulomb and tension cutoff surfaces in meridional and deviatoric planes

Mohr-Coulomb flow rules

Granular flow can be well described as flow rules. The flow potential G is chosen to be a hyperbolic function in the meridional stress plane and a smooth elliptic function in the deviatoric stress plane, defined by:

$$G = \sqrt{(\epsilon c\mid_0 \tan\psi)^2 + (R_{mw} q)^2} - p\tan\psi \tag{2.38}$$

and

$$R_{mw} = \frac{4(1-e^2)\cos^2\Theta + (2e-1)^2}{2(1-e^2)\cos\Theta + (2e-1)\sqrt{4(1-e^2)\cos^2\Theta + 5e^2 - 4e}} \times \frac{3-\sin\phi}{6\cos\phi} \tag{2.39}$$

where ψ is the dilatancy angle of material, $c|_0$ is the initial cohesion yield stress, ϵ is a parameter that characterizes the eccentricity of the flow potential. e referred to as the deviatoric eccentricity, describing the "out-of-roundedness" of the deviatoric section in terms of the ratio between the shear stress along the extension meridian and the shear stress along the compression meridian, is a function of the internal friction angle ϕ, given as $e = (3-\sin\phi)/(3+\sin\phi)$.
An additive strain rate decomposition is assumed:

$$d\boldsymbol{\varepsilon} = d\boldsymbol{\varepsilon}^{el} + d\boldsymbol{\varepsilon}^{pl},$$

where $d\boldsymbol{\varepsilon}$ is the total strain rate, $d\boldsymbol{\varepsilon}^{el}$ is the elastic strain rate, and $d\boldsymbol{\varepsilon}^{pl}$ is the inelastic (plastic) strain rate.
The constitutive flow rule can be written as:

$$d\boldsymbol{\varepsilon} = \frac{d\bar{\varepsilon}^{pl}}{g}\frac{\partial G}{\partial \boldsymbol{\sigma}},$$

where g can be written as

$$g = \frac{1}{c}\boldsymbol{\sigma} : \frac{\partial G}{\partial \boldsymbol{\sigma}}$$

Extended Drucker-Prager model

The extended Drucker-Prager models:

- are used to model frictional materials, which are typically granular-like soils and rock, and exhibit pressure-dependent yield (the material becomes stronger as the pressure increases);
- are used to model materials in which the compressive yield strength is greater than the tensile yield strength, such as those commonly found in composite and polymeric materials;
- allow a material to harden and/or soften isotropically;
- generally allow for volume change with inelastic behavior: the flow rule, defining the inelastic straining, allows simultaneous inelastic dilation (volume increase) and inelastic shearing;
- can be defined to be sensitive to the rate of straining, as is often the case in polymeric materials;

linear Drucker-Prager model

The deviatoric stress measure of DPEP can be defined as

$$t - p\tan\phi - c = 0 \tag{2.40}$$

where

$$t = \frac{q}{2}[1 + \frac{1}{K} - (1 - \frac{1}{K}(\frac{r}{q})^3) \tag{2.41}$$

where $K(\theta, f_\alpha)$ is a material parameter. To ensure convexity of the yield surface, $0.778 \leq K \leq 1.0$. This measure of deviatoric stress is used because it allows the matching of different stress values in tension and compression in the deviatoric plane, thereby providing flexibility in fitting experimental results when the material exhibits different yield values in triaxial tension and compression tests. With this expression for the deviatoric stress measure, the yield surface is defined as

$$F = t - p\tan\beta - d = 0 \tag{2.42}$$

where

- $d = (1 - \frac{1}{3}\tan\beta)\sigma_c$ if hardening is defined by the uniaxial compression yield stress, σ_c;

- $d = (\frac{1}{K} + \frac{1}{3}\tan\beta)\sigma_t$ if hardening is defined by the uniaxial tension yield stress, σ_t;

- $d =$ d if hardening is defined by the shear (cohesion) yield stress, d;

and $\beta(\theta, f_\alpha)$ is the friction angle of the material in the meridional stress plane. Potential flow in the linear model is assumed, so that

$$d\boldsymbol{\epsilon}^{pl} = \frac{d\bar{\epsilon}^{pl}}{c}\frac{\partial G}{\partial \boldsymbol{\sigma}} \tag{2.43}$$

where

- $c = (1 - \frac{1}{3}\tan\psi)$ if hardening is defined in uniaxial compression;

- $c = (\frac{1}{K} + \frac{1}{3}\tan\psi)$ if hardening is defined in uniaxial compression;

- $c = \frac{1}{2}(1 + \frac{1}{K})$ if hardening is defined in uniaxial compression

and

- $d\bar{\epsilon}^{pl} = |d\bar{\epsilon}^{pl}|$ in the uniaxial compression case;

- $d\bar{\epsilon}^{pl} = d\bar{\epsilon}^{pl}$ in the uniaxial tension case;

- $d\bar{\epsilon}^{pl} = \frac{d\gamma^{pl}}{\sqrt{3}}$ in the pure shear case, where γ^{pl} is the engineering shear plastic strain.

G is the flow potential, chosen in this model as

$$G = t - p\tan\psi \tag{2.44}$$

Non-dilatant double-shearing model

If the flow is considered to be in a vertical channel or slot in the (x,z) plane, with the z-axis vertically upwards. Assuming plane strain conditions, the non-zero components of the stress tensor satisfy the equilibrium equations:

$$\begin{aligned} \frac{\partial \sigma_{xx}}{\partial x} + \frac{\partial \sigma_{xz}}{\partial z} &= 0, \\ \frac{\partial \sigma_{xz}}{\partial x} + \frac{\partial \sigma_{zz}}{\partial z} &= \rho g \end{aligned}$$

where ρ denotes the bulk solid density, assumed constant, and g is the acceleration due to gravity. In terms of stress invariants p and q and the stress angle Ψ which are defined by

$$\begin{aligned} p &= -\frac{1}{2}(\sigma_{xx} + \sigma_{zz}), \\ q &= \frac{1}{2}\sqrt{(\sigma_{xx} - \sigma_{zz})^2 + 4\sigma_{xz}^2}, \\ \tan 2\Psi &= \frac{2\sigma_{xz}}{\sigma_{xx} - \sigma_{zz}} \end{aligned}$$

we have the following standard expressions

$$\begin{aligned} \sigma_{xx} &= -p + q\cos 2\Psi \\ \sigma_{zz} &= -p - q\cos 2\Psi \\ \sigma_{xz} &= q\sin 2\Psi \end{aligned}$$

For a cohesionless granular material, the stress relations are completed with the assumption of the Coulomb-Mohr yield condition

$$q = p\sin\phi \tag{2.45}$$

where ϕ denotes the angle of internal friction which is assumed to be constant. The above equations are generally accepted as a reasonable basis for the determination of the stress components. For steady flow the non-zero velocity components u(x, z) and w(x, z) in the x and z directions respectively satisfying the equations

$$\frac{\partial u}{\partial x} + \frac{\partial \omega}{\partial z} = 0 \tag{2.46}$$

$$\left(\frac{\partial u}{\partial z} + \frac{\partial \omega}{\partial x}\right)\cos 2\Psi - \left(\frac{\partial u}{\partial x} - \frac{\partial \omega}{\partial z}\right)\sin 2\Psi + \sin\phi\left(\frac{\partial u}{\partial z} - \frac{\partial \omega}{\partial x} + 2\omega\right) = 0 \tag{2.47}$$

where for steady flow the quantity ω is defined by

$$\omega = u\frac{\partial \Psi}{\partial x} + w\frac{\partial \Psi}{\partial z} \tag{2.48}$$

2.3.6 Finite Element Method

Overview of Eulerian analysis

Pure Eulerian analysis is a finite element technique in which materials are allowed to flow across element boundaries in a rigid mesh. In the more traditional finite element formulation (also known as the Lagrangian technique), materials are closely associated with an element, and the materials move only with the deformation of the mesh. Because the element quality issues associated with a deformable mesh are not present in Eulerian analyses, the Eulerian technique can be very effective at treating problems involving very large deformations, material damage, or fluid materials.

Eulerian mesh deformation

The Eulerian time incrementation algorithm is based on an operator split of the governing equations, resulting in a traditional Lagrangian phase followed by an Eulerian, or transport, phase. This formulation is known as Lagrange-plus-remap process.During the Lagrangian phase of the time increment nodes are assumed to be temporarily fixed within the material, and elements deform with the material. During the Eulerian phase of the time increment deformation is suspended, elements with significant deformation are automatically remeshed, and the corresponding material flow between neighboring elements is computed.

At the end of the Lagrangian phase of each time increment, a tolerance is used to determine which elements are significantly deformed. This test improves performance by allowing those elements with little or no deformation to remain inactive during the Eulerian phase. The inactive elements typically have no impact on the visualization of an Eulerian analysis; however, plotting an Eulerian mesh using a very large deformation scale factor may reveal slight deformations for elements within the deformation tolerance.

Eulerian material advection

As material flows through an Eulerian mesh, state variables are transferred between elements by advection. The variables are assumed to be linear or constant in each old element, then these values are integrated over the new elements after remeshing. The new value of the variable is found by dividing the value of each integral by the material volume or mass in the new element.

Second-order advection assumes a linear distribution of the variable in each old element. To construct the linear distribution, a quadratic interpolation is constructed from the constant values at the integration points of the middle element and its adjacent elements. A trial linear distribution is found by differentiating the quadratic function to find the slope at the integration point of the middle element. The trial linear distribution in the middle element is limited by reducing its slope until its minimum and maximum values are within the range of the original constant values in the adjacent elements. This process is referred to as flux limiting and is essential to ensure that the advection is monotonic.

The Eulerian analysis technique can be coupled with traditional Lagrangian techniques to extend the simulation functionality in Abaqus:

- Arbitrary Lagrangian-Eulerian (ALE) adaptive meshing is a technique that combines features of Lagrangian and Eulerian analysis within the same part mesh. ALE adaptive meshing is typically used to control element distortion in Lagrangian parts undergoing large deformations, such as in a forming analysis.

- Coupled Eulerian-Lagrangian (CEL) analysis allows Eulerian and Lagrangian bodies within the same model to interact. Coupled Eulerian-Lagrangian analysis is typically used to model the interactions between a solid body and a yielding or fluid material, such as a Lagrangian drill traveling through Eulerian soil or an Eulerian gas inflating a Lagrangian airbag.

Some features, advantages, and disadvantages of the Lagrangian and Eulerian can be summarized in the table below.

2.4 Common Mixers

Mixer used in industry are diverse; the type of mixer to be used and its operational conditions are dependent upon the intended application. For example, in the pharmaceutical industry, bladed mixers are used for mixing and granulation of powders.

Lagrangian mesh	Eulerian mesh
Lagrangian coordinates of n-odes move with the material. Material coordinates of material points are time invariant.	Eulerian coordinates of nodes are fixed and coincide with s-patial points. Spatial coordinates of material points vary with time.
No material passes between elements.	Material flows through the mesh.
Element quadrature points remain coincident with material points.	The material point at a given element quadrature point changes with time. This makes dealing with history-dependent materials difficult.
Boundary nodes remain on the boundary. Therefore, boundary conditions and interface conditions are easily applied.	Boundary nodes and the material boundary may not coincide. Therefore, boundary conditions and interface conditions are hard to apply.
Severe mesh distortion can occur because the mesh deforms with the material.	There is no mesh distortion because the mesh is fixed in space. However, the domain that needs to be modeled is larger because we do not want the body to leave the domain.

Table 2.1: A comparison of Lagrangian mesh and Eulerian mesh

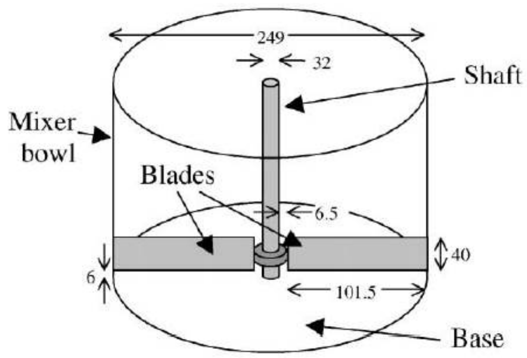

Figure 2.9: Diagrammatic representation of the mixer. Dimensions are cited in mm

2.4.1 High Shear Mixer

DEM studies

The experiment of high shear mixer was carried out in (Steward et al., 2001), in which a vertical cylinder stirred by two long flat blades opposed at 180° (Fig.2.9). The mixer and blade configurations were chosen so that the flow produced was as simple as possible. Because the mixer is vertical the blades are constantly immersed at the same depth, producing a steady-state flow, unlike a horizontal mixer where flow is periodic. This configuration is used directly for a wide range of industrial processes, but most commonly for high intensity mixers and high shear granulators. Flat blades are the simplest type of mixing element. The three-dimensional motion of glass beads in a simple bladed mixer has been studied at five different shaft speeds and five different fill levels using PEPT. Particle motion for the different conditions has been shown by sections through the velocity fields and by frequency distributions of the velocity components.

A detailed comparison between DEM study and PEPT was studied with the same geometry in (Stewart et al., 2001). Flow patterns, velocity distributions were compared between the results of experiment and five cases of different DEM parameters (shown in Fig.2.10, 2.11). More extensive investigations with DEM was carried out by (Chandratilleke et al., 2009, 2010, 2012) in which effects of operation and material properties was taken into consideration. Study of mixing process was also involved. In (Chandratilleke et al., 2010), the influence of blade speed on mixing was studied in terms of a wide range of parameters related to flow, structure, and forces, such as flow fields in horizontal and cylindrical sections, coordination number, porosity, mixing index, force network in horizontal and vertical sections, inter-particle forces, and blade torque. The mixing pattern

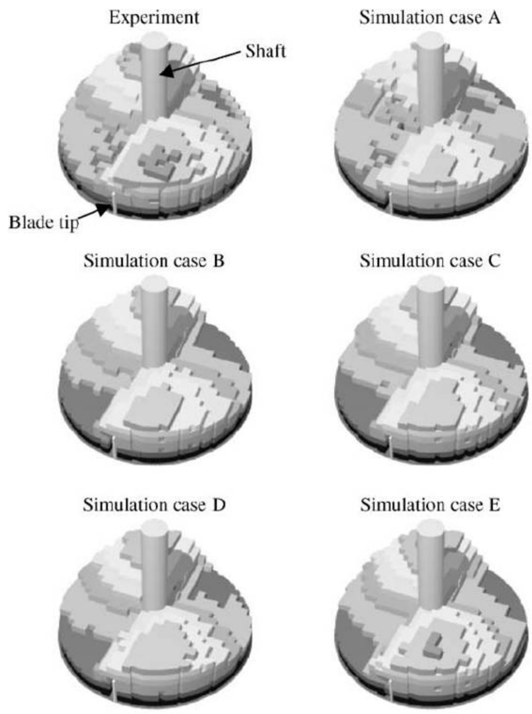

Figure 2.10: Surfaces from PEPT experiment and the five DEM simulations.

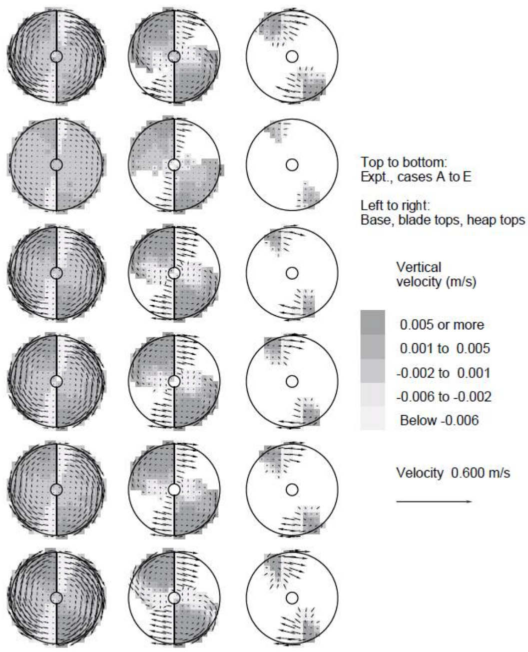

Figure 2.11: Velocities fields from experiment and DEM simulations

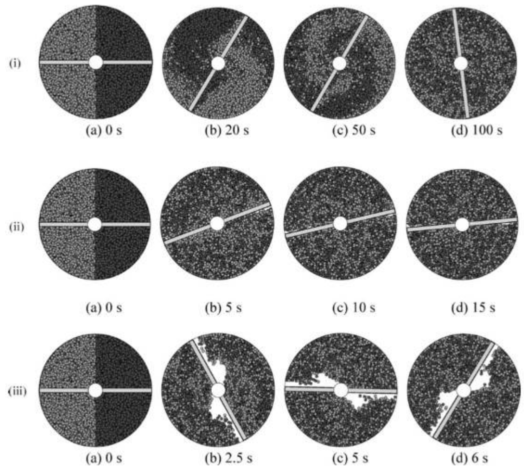

Figure 2.12: Mixing of dark and light gray particles initially arranged in the left and right halves of the mixer sliced at 37.5 mm height.

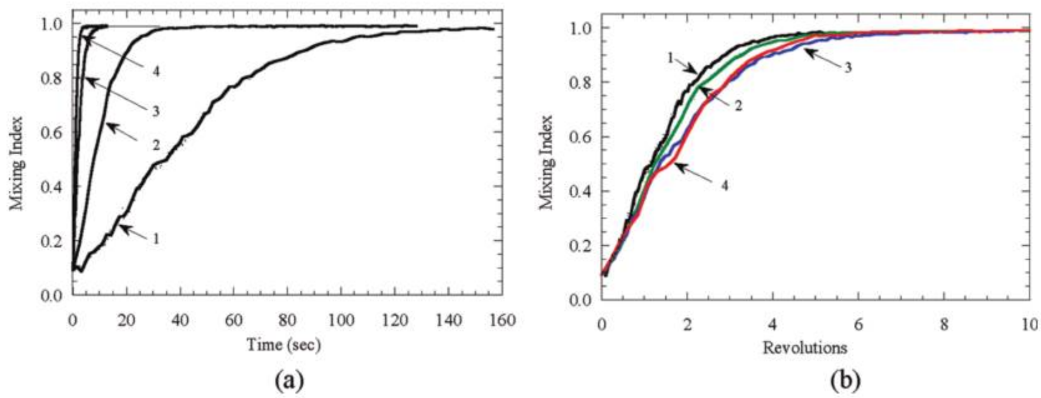

Figure 2.13: Mixing index as a function of time (a) and revolutions (b)

and index was shown in Fig.2.12 and 2.13. The effects of blade rake angle and gap in a cylindrical mixer were also investigated in (Chandratilleke et al., 2009). The geometry can be illustrated in Fig.2.14, in which the angle between blades and bottom as well as gap were defined. In Fig.2.15, the DEM model was verified by comparison with PEPT via the probability of density distribution in detail. The results show that the probability density curve of the simulations agrees reasonably well with those of the PEPT study.

CFD studies

In terms of continuum method used in investigation of high shear mixer, most studies have focused on computational fluid dynamics (CFD). Based on KTGF, an Eulerian-Eulerian approach where particles are treated as a continuous medium was used for study in a high shear mixer (Darelius et al., 2008b). It was found that the bed height could not be

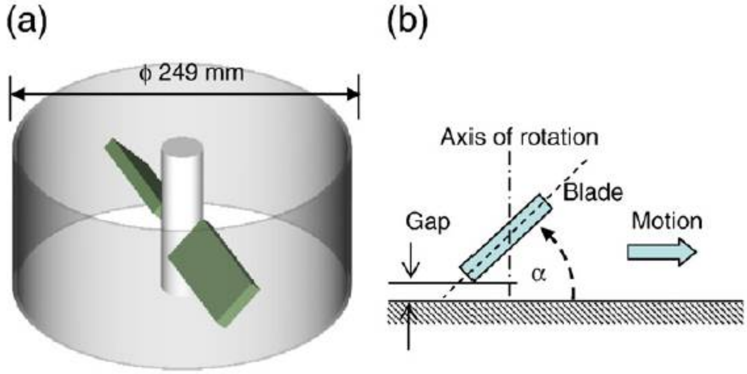

Figure 2.14: (a) Geometry of the mixer used in the simulation, (b) Definitions of gap and rake angle a for a single blade.

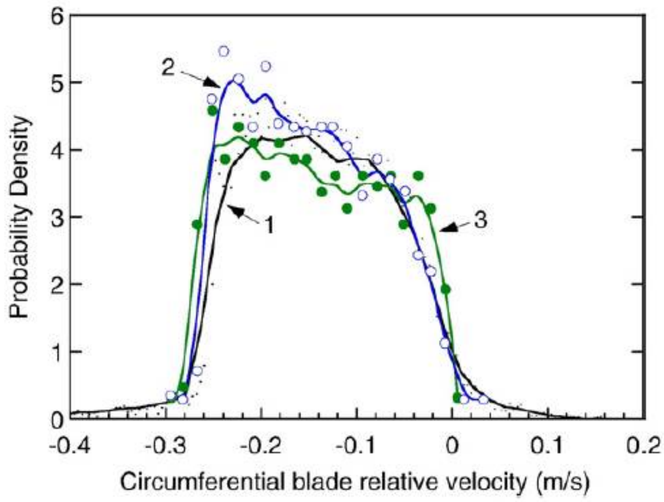

Figure 2.15: Comparison of simulations with PEPT results in terms of probability density distribution of blade relative velocities in circumferential direction for the entire bed

captured in the simulation using free slip as wall boundary condition for the solid phase, but as the partial slip was implemented to increase energy dissipation at the wall, the bed height was well predicted. Moreover, the wall velocity magnitude could be reasonably well predicted using both free and partial slip boundary conditions, but the velocity direction was poorly predicted as too much particle tangential momentum was transformed into axial momentum at the vessel wall. The discrepancy between simulated and measured velocities in the region close to the impeller can probably be better described if the frictional stress models are developed, e.g. by tackling the cohesiveness in dense particle flow. In the dense region, a constitutive law based on visco-plastic approach was proposed by Jop et al (Jop et al., 2006). The model gives quantitative predictions for the flow shape and velocity profiles. For stiff particles the shear stress is shown to be proportional to the normal stress, with a coefficient of proportionality, a single dimensionless number called inertial number I:

$$\tau = \mu(I)P \tag{2.49}$$

$$I = \dot{\gamma}d/(P/\rho_s)^{0.5} \tag{2.50}$$

$$\mu(I) = \mu_s + (\mu_2 - \mu_s)/(I_0/I + 1) \tag{2.51}$$

where $\mu(I)$ is the friction coefficient, d is the particle diameter and ρ_s is the particle density. However, the simple scalar law (2.49) cannot be applied in more complex flows where shear in different directions is present and a full three-dimensional rheology is needed. In their dense model, the granular material is described as an incompressible fluid with the internal stress tensor:

$$\sigma_{ij} = -P\delta_{ij} + \tau_{ij} \tag{2.52}$$

$$\tau_{ij} = \eta(|\dot{\gamma}|, P)\dot{\gamma}_{ij} \tag{2.53}$$

$$\eta(|\dot{\gamma}|, P) = \mu(I)P/|\dot{\gamma}| \tag{2.54}$$

$$I = |\dot{\gamma}|d/(P/\varrho_s)^{0.5} \tag{2.55}$$

The simulation proceeds by solving the incompressible Navier-Stockes equations with the internal stress given by 2.52. The results in Fig.2.16 show that the proposed rheology

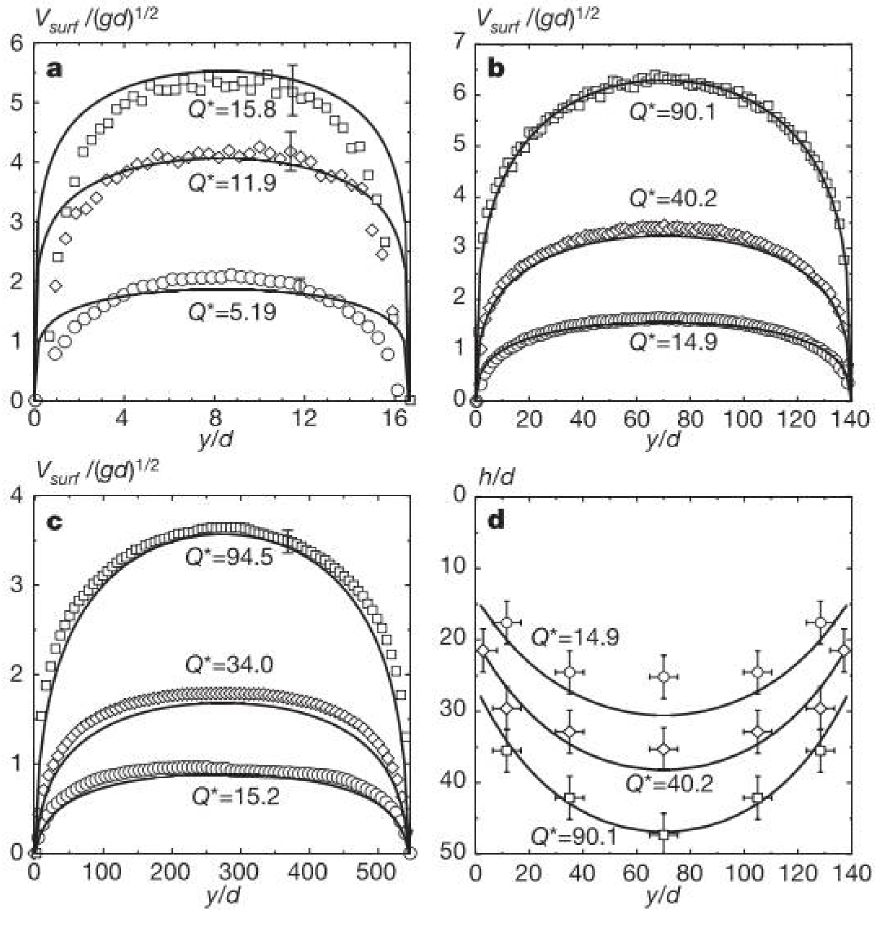

Figure 2.16: Comparison of 3D simulations (lines) and experimental results (symbols) for different flow rates in an inclined chute (Jop et al., 2006).

gives quantitative-agreed predictions for this complex 3D flow.

In (Khalilitehrani et al., 2013), a approach applied to dense particulate systems and based on the constitutive law proposed by Jop et al (Jop et al., 2006) was employed to study the dense regions of a High Shear Granulator. The model gave a good general description of the flow field and bed shape. However the model is insufficient in some aspects mostly related to the regions with low volume fraction. The agreement of comparison between experimental and simulated velocity fields is fairly good, but the model overestimates the velocity of the particle field as compared to experimental data (shown in Fig.2.17). This may be due to the fact that the fluctuating part of the velocity of the particles is not modelled when the particulate phase is assumed to be a non-Newtonian fluid.

A further study (Khalilitehrani et al., 2014) modelled a high shear granulation system, including both dense and dilute regions. The dense region was modelled using an approach in which the system was treated as a visco-plastic fluid and the rheology of such a fluid

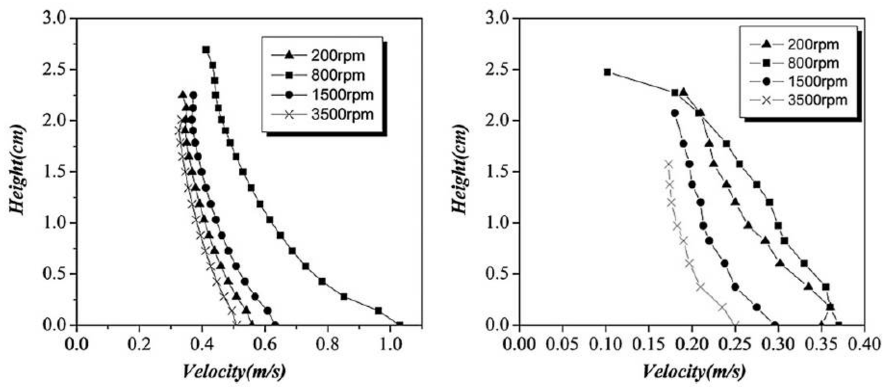

Figure 2.17: Tangential velocity profiles along the sidewalls left: Model right: Experiments (Khalilitehrani et al., 2013).

was evaluated. The dilute regions were modelled by the standard Kinetic Theory of Granular Flow (KTGF). The switching between the models was accounted for by using the dimensionless inertial number, defined as the ratio of shear forces and pressure forces. Compared with the earlier models, the current model showed a good prediction of the velocity field as shown in Fig.2.18. In a transient mixing study (Nguyen et al., 2014), an Eulerian-Eulerian multiphase framework was employed to model and simulate particulate flow and mixing behaviours in the blending of dry powders for inhalation. The model can capture the main features in granular flow motion, e.g. bed height and the dominating flow direction. The flowing patterns were easily obtained (Fig.2.19), however, no matter using the theoretical frame of KTGF or extended KTGF, the simulation results are still not able to agree well with the experimental results, as shown in Fig.2.20.

2.4.2 Rotating Drum

Among most mixers, rotating drum is a simplification of industrial 2D or 3D mixing devices. The simple rotating drum enables to easily understand mixing dynamics. The system consists of a cylinder in axial rotation and is filled with a mixture of particles, often binary mixtures. The use of rotating drums or kilns as granular mixers, dryers and gas-solid reactors is widespread in the chemical industries and new applications are still emerging. The interest for rotating drums lies in its simplicity and inherent flexibility. It can also be designed to accommodate a broad range of material characteristics. The main flow regimes for solid mixtures in rotating drums are classified from the Froude number (Fr). It is accepted that the cross-sectional behaviour of the bed progresses through six

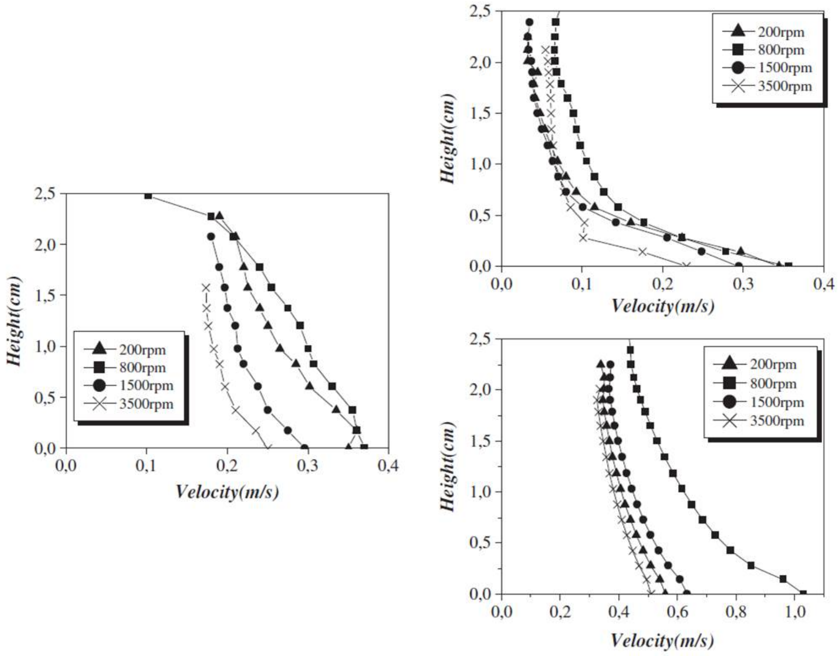

Figure 2.18: Velocity profiles; left: experimental data; right, up: Rheology + KTGF (current model); right, down: Rheology model (Khalilitehrani et al., 2014).

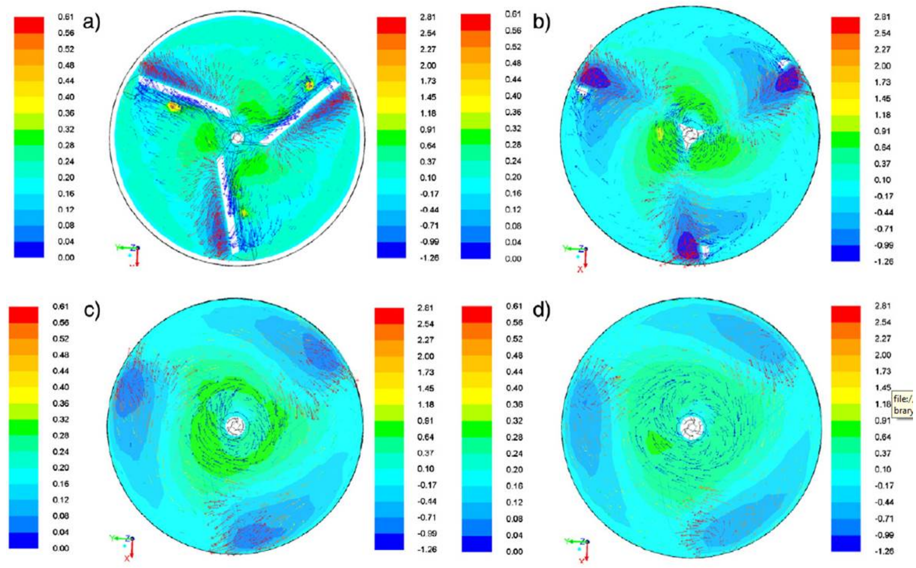

Figure 2.19: Horizontal snapshots of axial velocities at heights of (a) 1cm, (b) 2cm, (c) 3cm, and (d) 4cm. (Nguyen et al., 2014)

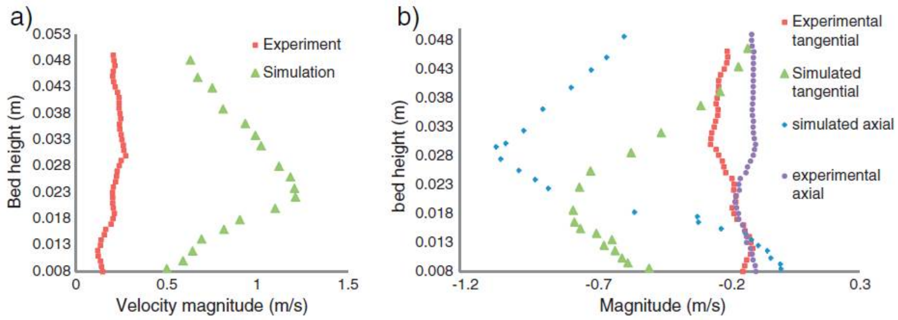

Figure 2.20: Velocity profiles at the vessel wall (a) velocity magnitude, (b) tangential and axial velocities. (Nguyen et al., 2014)

characteristic patterns as rotational speed increases. From the definition of the Froude number, it is possible to determine the effect of centrifugal forces over gravitational forces via:

$$Fr = \frac{R\omega^2}{g} \tag{2.56}$$

where R is the cylinder radius and g is the gravitational acceleration. Bell noted that scaling of particulate processes should be done with extreme caution since granular materials, unlike gases and liquids, behave differently at different scales. A Froude number (Fr) of unity indicates that the gravitational forces are balanced by centrifugal ones resulting in a motion within the cylinder where the material adheres to the walls: a regime known as centrifuging. The work of Henein et al. showed that the rolling bed regime occurs at low Froude numbers. They also showed that for a range of materials, the bed motion was in the rolling regime at Fr above 10^{-3} at even their lowest experimental drum loading of 4%. Mellmann reviewed the different operating regimes based on the Froude number. He showed that rolling beds typically occur at Fr between 10^{-4} and 10^{-2} with a cylinder loading greater than 10% and the centrifugation regime occurs at Froude numbers greater than 1.

Comparison between DEM and PEPT

Conventionally, the results derived from DEM was supposed to be compared with that from PEPT. The paper (Yang et al., 2003) presented a numerical study of particle flow in a horizontal rotating drum by DEM with special reference to the effect of rotation speed. The results were analysed in terms of microdynamic variables related to flow structure such as porosity and coordination number, and force structure such as particle interaction

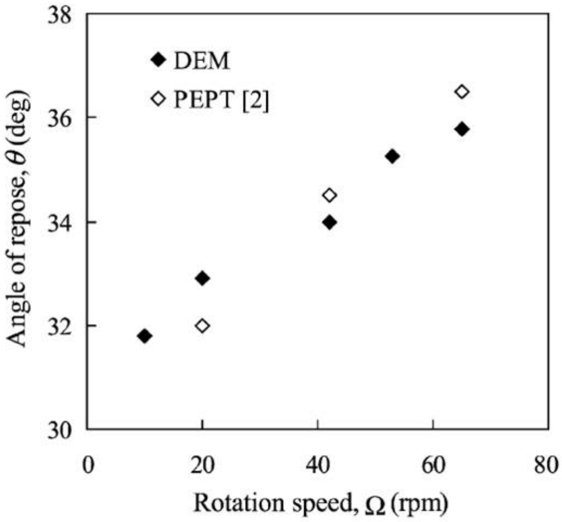

Figure 2.21: Dynamic angle of repose as a function of rotation speed.

forces, relative collision velocity and collision frequency. The results of DEM was compared with that of PEPT, for example, Fig.2.21 shows the dependence of the dynamic angle of repose θ on the rotation speed Ω, where θ is defined as the angle of the surface of rotating particles relative to a horizontal plane and obtained via a least square fitting of centres of particles at the surface. The agreement between DEM simulation and PEPT measurement is fairly good, both indicating the dynamic angle of repose increases linearly with the speed of rotation.

Six flow regimes in a rotating drum

With the discrete element method Runyu Yang et at (Yang et al., 2008) investigated the granular flow dynamics in different regimes. By varying the rotation speed and particle-wall sliding friction over a wide range, six flow regimes were produced. The results showed that the angle of repose of the moving particle bed had a weak dependence on the rotation speed in the slumping and rolling regimes, and increased significantly as the flow transited to the cascading and cataracting regimes. The mean flow velocity increased with the rotation speed, but the normalised velocity against the drum speed in the continuous regimes collapsed into a single curve, which can be well described by a log-normal distribution. The corresponding six regimes are shown in Fig.2.22. The particle flow went through different flow regimes as the rotation speed varied from 0.1 to 300 rpm (Fr=$5.6 \times 10^{-7} \sim 5$). At 1 rpm, the flow was in the slumping regime with particles at the bottom of the bed in small, intermittent avalanches. As the speed increases to 5 rpm, the time interval becames

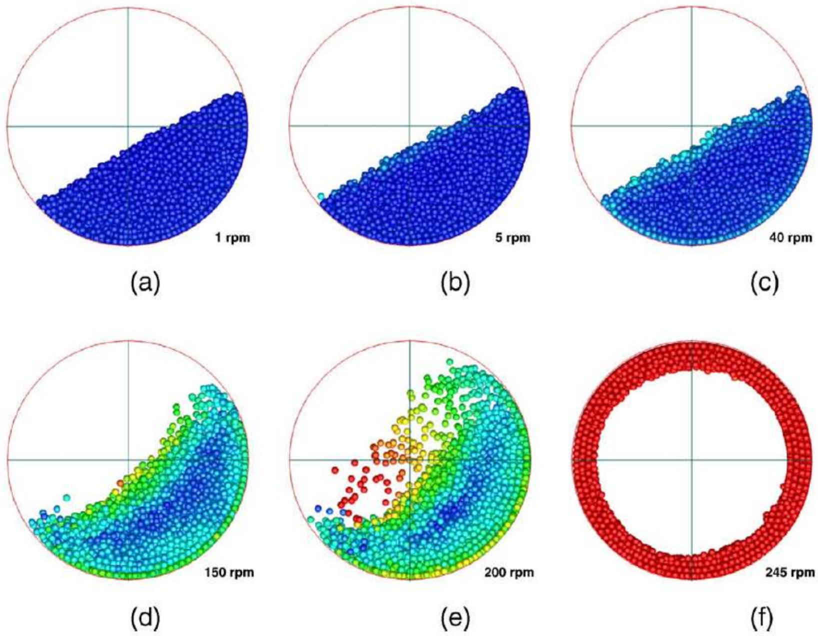

Figure 2.22: Particle flow patterns at different rotation speeds showing different flow regimes: (a) slumping; (b) slumping-rolling transition; (c) rolling; (d) cascading; (e) cataracting; and (f) centrifuging. Colour represents particle velocity.

shorter and the flow was in the transition period due to the competition between the gravity and the centrifugal force. So the particle bed was not stable and moved back and forth around the equilibrium position. At 40 rpm, the flow was clearly in the rolling regime characterised by a flat surface, a thin layer of fast moving particles and the majority of particles moving slowly at the bottom. Further increasing the rotation speed to 80 and 150 rpm led the flow into the cascading regime which showed an S-curved surface with a clear shoulder and tail. At 200 rpm, the particles had enough energy to be thrown off the bed surface into the space beyond the middle point, which defines the cataracting regime. At 245 rpm, the particles were thrown so far into the space that they traveled around the inner edge of the cylinder. This centrifuging motion was characterised by the particles adhering to the drum wall as a uniform solid layer with little relative motion between particles. Note at this speed, the Froude number Fr is 3.35 far beyond the unity.

Geometry method applied to drum

Slow granular mixing processes can be analysed by a geometric technique commonly seen in industry (Metcalfe et al., 1995a). An upright two-dimensional disk partially filled with

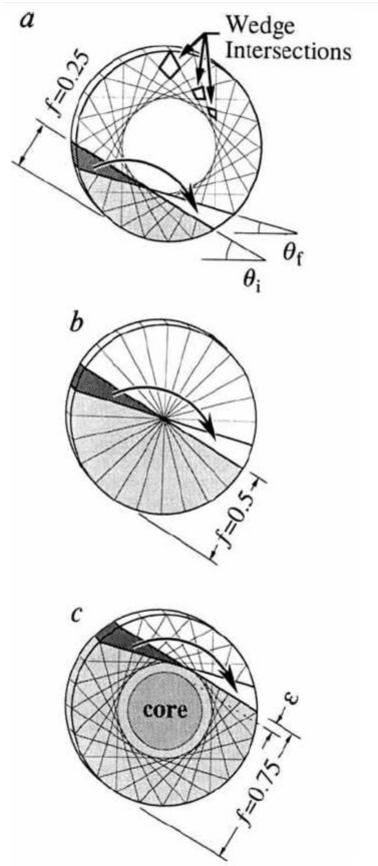

Figure 2.23: (a) Schematic of avalanche mixing for a quarter-filled disk; (b) a half-filled disk and a three-quarter-filled disk. (c) In all cases, the disk rotates slowly clockwise, and distinct avalanches occur which take material from an uphill wedge (dark grey) to a downhill wedge (white), as indicated by solid arrows. Mixing within the wedges is taken to obey a deterministic map; mixing between wedges occurs in quadrilateral wedge intersections indicated.

coloured passive particles and rotating about its axis is considered as an example of a modelled system. For slow rotations, the surface layer mixes through the action of successive avalanches (shown in Fig.2.23). Slow mixing implies that each avalanche stops completely before a new one begins. The avalanche duration scales as $\sqrt{D/g}$, where D is the container diameter and g is the acceleration due to gravity, so we require $\Omega\sqrt{D/g} \ll 1$, where Ω is the rotation rate. Material below the surface layer rotates as a solid body with the disk. A side-by-side comparison between experiments and numerical simulations, using a random map to model mixing within the wedges, are shown in Fig.2.24.

However, there are limitations of this geometrical method (McCathy, 1996). Core periphery is different under the mixing of two powders with size, shape, and density differences. The core precession, the line rotates past its original position in the direction of the container rotation (shown in Fig.2.25), can not be captured by the geometrical method. A

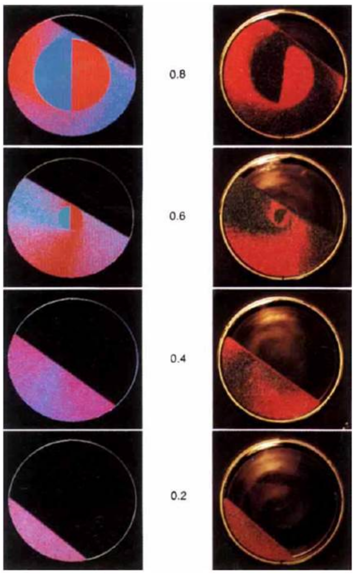

Figure 2.24: Mixing patterns form simulation (left) and experiment (right) after two disk revolutions at the indicated fill levels f.

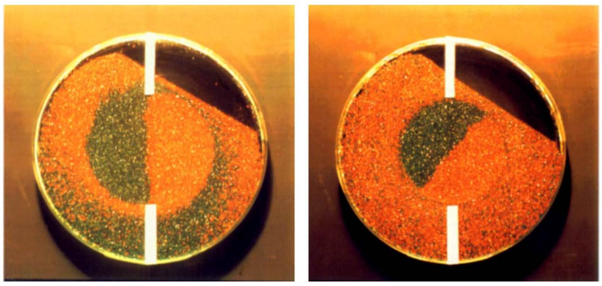

Figure 2.25: A comparison between two experimental photos of a 2-D mixer with a circular cross-section filled with large cubic particles. The first photo (a) is after 3 revolutions and the second (b) is after 40 revolutions. Note that the interface within the core has precessed by 42 degrees.

hybrid simulation technique merging geometrical and dynamical approaches improved the original geometrical method. The comparisons between hybrid simulations and experiments are shown in Fig.2.26.

Kinematics in the rolling regime

A representative lagrangian approach is kinematics in the low speed rotation regime, when the free surface of the granular solids is nearly flat, and when particles are identical so that segregation is unimportant. The flow is divided into two regions: a rapid flow region of the cascading layer at the free surface, and a fixed bed of particles rotating at the angular speed of the cylinder. The continuum model, in which averages are taken across the layer, is used to analyze the flow in the layer. As shown in Fig.2.27, particles in a partially filled

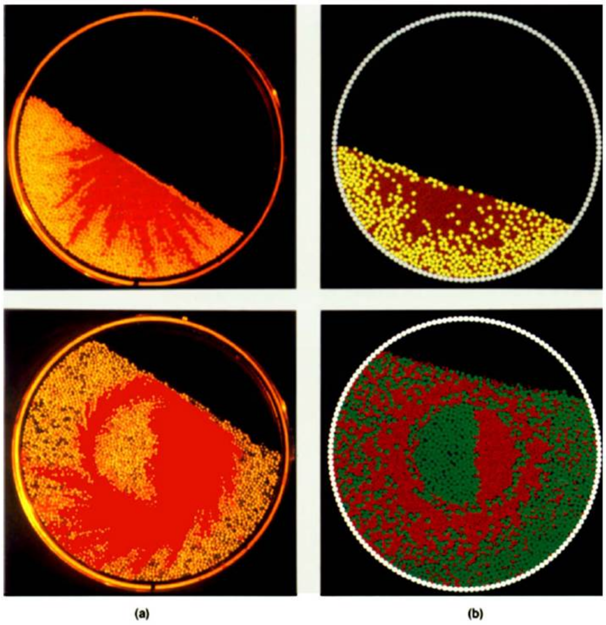

Figure 2.26: Shown is a comparison of experiments (a) and simulations (b) of segregating materials at f = 0.4 and f = 0.75. The simulations easily capture the large-scale, geometrical features, such as the core, as well as the smaller-scale, dynamical characteristics like radial segregation. The simulation at the top involves 3,000 particles; the simulation ar the bottom, 6,000 particles.

horizontal drum rotate about its axis. Conditions are as follows: the system operates in the rolling regime where the free surface is nearly flat, and there is a steady flow of particles in a thin layer at the free surface of the bed. The flow in the drum can be divided into two regions: the rapid flow region of the cascading layer and the bed rotating at the angular velocity of the drum. In general, there is a region of slow flow between these tow regions, where the nearly close-packed particle assembly experiences plastic deformation. Rotation of the drum results in a flow of particles from the fixed bed into the cascading layer in the upper half of the layer and a flow from the layer into the fixed bed in the lower half. The steady state mass balance equation for the flow in the layer is given by

$$\frac{d}{dz}(\rho u \delta) = \rho_b v_{int} \cdot n \tag{2.57}$$

where δ(x) is the layer thickness, and u(x) is the velocity averaged across the layer,

$$u =< v_x >= \frac{1}{\delta} \int_{-\delta}^{0} v_x dy. \tag{2.58}$$

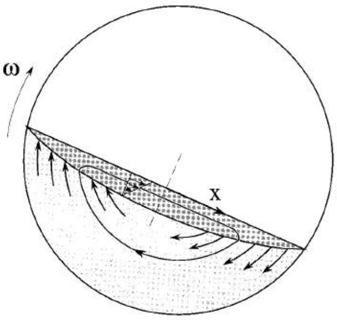

Figure 2.27: Schematic view of the flow in the rotating drum mixer

Configurations	Kinetic viscosity model	Frictional viscosity model	α_{SC}
S1	Syamlal-O'brien	-----	-----
S2	Gidaspow	-----	-----
S3	Syamlal-O'brien	Schaeffer	0.50
S4	Syamlal-O'brien	Schaeffer	0.61
S5	Gidaspow	Schaeffer	0.50
S6	Gidaspow	Schaeffer	0.61

Figure 2.28: Model configurations used in the CFD simulations

As a result, essential aspects of mixing of granular materials in the continuous flow regime in a rotating cylinder corresponding to a flat interface with a velocity dependent dynamic angle of repose can be modeled in terms of a cross-averaged, nearly one-dimensional continuum model. The model yields the average velocity in the cascading layer of particles and the shape of the layer. Model results are presented for three different cases: plug flow, Bagnold's profile and simple shear flow. The model has one adjustable parameter which determines the magnitude of the collision stresses. All other parameters are independently estimated from the static and dynamic angles of repose, the rotational speed and the filling level of the cylinder.

CFD studies

Based on KTGF, D.A.Santos et al (Santos et al., 2013) studied the hydrodynamic behavior in a rotating drum under different operating conditions with the Eulerian-Eulerian multiphasic model. The theory of granular flow was used in the simulations. The results concerned with different solid flow regimes and velocity distributions were compared with experimental data. In order to obtain the volume fraction of the granular solid phase and particle velocity profiles in a rotating drum, six different models configurations were used in this work, as shown in Fig.2.28. Various filling levels were studied with the ex-

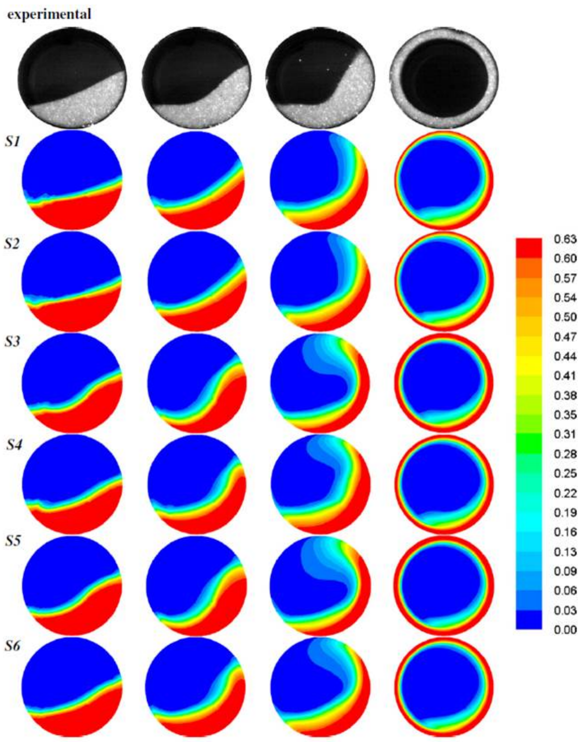

Figure 2.29: volume fraction of the granular solid phsse of 1.09mm and fill level of 31.40% for drum rotating at 1.45, 4.08, 8.91 and 16.4 rad/s from the left to the right, respectively: experimental and simulated using model configurations S1, S2, S3, S4, S5 and S6.

perimental data. Fig.2.29 was one of them. However, only four regimes concerned with rolling, cascading, cataracting and centrifuging were identified by simulations as the rotational speed increases. S1 and S2 configurations qualitatively agreed better with the experimental observations than the other configurations.

Stochastic approach

A stochastic approach of Markov chains was proposed by Javan D.Tjakra (Tjakra et al., 2012, 2013). This approach captures the collective dynamics which can be obtained from the Markov chains operator. The obtained operators are used to estimate the spatial particle distribution and the degree of particulate mixing as examples of collective dynamic features of polydisperse particulate systems. The results derived from Markov chains were also compared with DEM (shown in Fig.2.30).

Chaotic advection mixing in a drum

Experiments and computations show that granular flows in circular containers is steady which leads to poor mixing if advection is taken into account alone (no particle diffusion

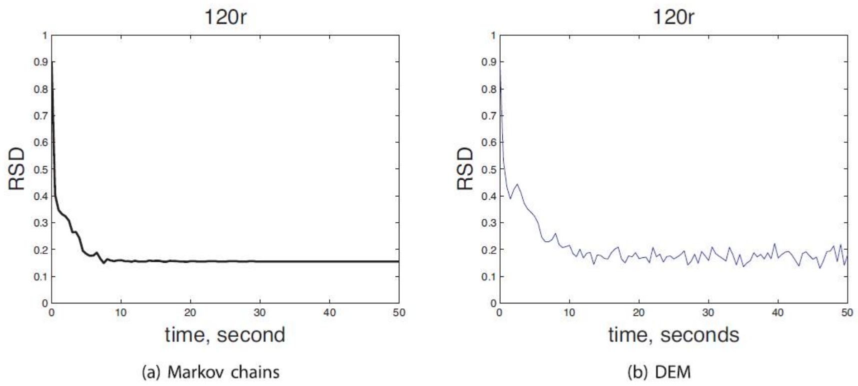

Figure 2.30: The RSD mixing index of binary disperse of particulate system at $\Omega = 120$ rpm

generated by interparticle collisions). In contrast, the flow in elliptical and square mixers is time periodic and results in chaotic advection and rapid mixing. Computational evidence for chaos in noncircular mixers is studied in terms of Poincarê sections (obtained from computing the particle trajectories by integration of the velocity field with respect to time [no diffusion considered], and noting the position after each half revolution of the mixer) and blob deformation (Khakhar et al., 1999). Poincarê sections show regions of regular and chaotic motion, and blobs deform into homoclinic tendrils with an exponential growth of the perimeter length with time. In contrast, in circular mixers, the motion is regularly everywhere and the perimeter length increases linearly with time. Poincarê sections and blob deformations are shown in Fig.2.31. The other signatures of chaos are a positive Liapunov exponent - exponential stretching - and the presence of horseshoe maps; the rate of stretching is considered in Fig.2.32. The change in the computed perimeter length of the blob increases linearly with time in the circular mixer, whereas an exponential increase of length with time is obtained for the blobs in the chaotic regions of the square and elliptical mixers.

2.5 Research Plan

Finite element study of flow kinematics and mixing behaviors in various particle mixers

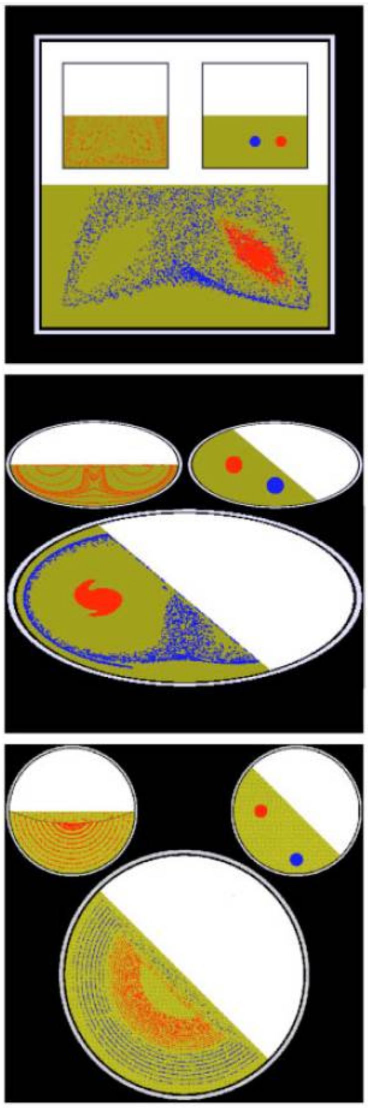

Figure 2.31: Comparison of the mixing of tracer particles in a circular, elliptical, and square mixer simulated using the model with no particle diffusion. The inset figure on the upper left-hand side shows the Poincarê section, and the initial condition is shown in the upper right-hand inset.

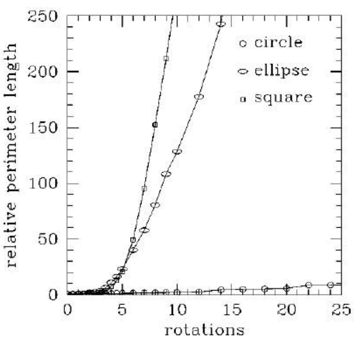

Figure 2.32: Variation of the relative perimeter length of a blob with time in the mixers. Note that while the perimeter length in the circular mixer grows linearly, the length in the non-circular mixers grows exponentially.

2.5.1 Research aims

Model development and validation

To develop and testify the new model (FEM within the frame of Eulerian method) under various circumstances by comparison with DEM results and experiments measurement.

Model studies

To study various mixing cases by taking into account the geometries (containers), operations in laboratories, material properties.

Potential industrial applications

To extend our new model from lab scale to a larger scale to fulfil the needs of industrial applications.

2.5.2 General methodology

FEM based on the Mohr-Coulomb model of elasto-plastic theory as the continuum simulation method will be used throughout the whole research.

2.5.3 Stages in the Research

Method validation in a high shear mixer

In order to validate the FEM model, we will establish the model in a high shear mixer with parameters similar to (Chandratilleke et al., 2010) and compare our results derived from FEM against that from DEM and experiments. To testify our method, we will consider the following aspects:

- Granular flow patterns.
- Bed profile types.
- Various types of flow velocity distributions.
- Stress distribution along the wall and blade.
- Torque variation as a function of time.

Practical application of FEM simulation to Mipro mixer

We will consider various effects of operational and material property to granular flow and mixing in the context of a realistic Mipro mixer. Operational effects taken into account include:

- Blade speed varied in a large range.
  we will study instantaneous vector field of relative velocities with different blade speeds at different sections.
- Blade rake angle and blade gap at the bottom.
  we will study probability density distribution of blade relative velocities at different angles, flow patterns in vertical cylindrical sections at different radii, angles and blade gap.
- Optimization of mixing time.
  we try to figure out an optimizing method of minimizing time to get to the well mixed state.

Material properties taken into account incorporate:

- Various material properties with respect to a continuum method such as cohesiveness, internal friction angle, dilation angle, etc.

Granular kinematics studied by FEM in a circular rotary drum

In a circular rotary drum at the rolling regime, we will investigate kinematics with FEM from the following aspects:

- The distribution of velocity magnitude.
- Transverse velocity distribution.
  we will compare our results of transverse velocity distribution to simple shear flow and Bagnold solution profile, which has been testified with experiments.
- Flow layer thickness and layer length in the active zone at various conditions.
- Proposing a scale-up law of flow layer thickness as a function of internal and external parameters.

Granular kinematics studied by FEM in a non-circular rotary drum

The whole study will be performed in the rolling regime of a non-circular (square, ellipse) rotary drum. We will study in the frame of FEM:

- The distribution of velocity magnitude.
- Transverse velocity distribution.
- Chaotic advection without considering the effects of diffusion.
  We try to simulate the streamline of Poincaré sections as well as deformation pattern of the marked blob by tracing particles in our method.

Mixing process in a circular rotary drum

We try to measure RSD (relative standard deviation) and mixing index during the mixing process. Results will be compared with DEM, CFD and Markov chains method results provided by (Tjakra et al., 2012, 2013). Several factors affecting mixing will be studied as follows:

- Rotational speed. Various Froude numbers characterising angle velocity will be tried during simulation.
- Material property from a continuum point of view such as cohesion yield stress, internal friction angle.
- Non-circular drum.

2.5.4 Time lines

- Model development and validation in a high shear mixer
  2014.03 — 2015.06
- Material properties and operational studies in a high shear mixer
  2015.06 — 2015.12
- Mixing in a drum
  2016.01 — 2017.02

Chapter 3

FEM study of particle flow and convective mixing in a cylindrical bladed mixer

3.1 Introduction

Blending different kinds of granules from initial separate phases into the homogeneous state is a common process in many industries such as pharmaceutical, food, and cosmetic industries. This process has many fascinating physical implications that demand continuous research (Aranson and Tsimring, 2006). The common device to complete particle blending mainly comprise the rotating drums (Yang et al., 2003, 2008), V-blenders, ribbon mixers (Musha et al., 2013) and CBM (Bridgwater, 2012). The CBM, consisting of an exterior shell and a central shaft inside with two opposed flat blades, can generate a high shear force to enhance the convective movement of particles and thus attracts extensive experimental and numerical-investigations in the literature (Stewart et al., 2001; Zhou et al., 2004; Chandratilleke et al., 2009, 2010, 2012). Parkerb et al. (2001) studied the motion of glass beads in a CBM using a positron emission particle tracking (PEPT) technique focusing on the influences of different shaft speeds and filling levels (Steward et al., 2001). Their experiment revealed several important features of particle flow such as the heap formation and recirculation zone around the blades, and evaluated the distributions of particle velocity residence time in the CBM system. A similar mixer was later simulated by Stewart et al. (Steward et al., 2001) via discrete element method (DEM). With

properly selected parameters of sliding friction and rolling friction, DEM can provide good predictions of the overall bed profile and particle velocities in various cases. Zhou et al. (Zhou et al., 2004) investigated the flow structure in terms of porosity and coordination number by DEM considering the binary mixing under different conditions of initial particle filling levels. Chandratilleke et.al. (Chandratilleke et al., 2009, 2010) further studied the effects of blade speed and blade rake angle on particle mixing index. They found that by increasing the blade speed, the mixing rate calculated in terms of step time can be significantly enhanced whereas the rate in terms of revolution number is adversely reduced. Their study also unveiled the critical importance of the particle recirculating flow for the mixing efficiency. Mixing of fine particles was explored by Chandratilleke et.al (Chandratilleke et al., 2014) aiming to develop a more universal understanding towards the effects of inter-particle van de Waals force, blade speed and rake angle on mixing rate so as to find the optimal design and operational conditions of CBMs.
However, how to efficiently simulate the collective behaviour of particles in practical mixing equipment is still challenging. It is known that, the DEM modelling, limited by the current computer capacity, is technically difficult to deal with the large scale industrial mixers where as many as billions of particles may be involved (Nguyen et al., 2014). Continuum models can largely mitigate such computational tension as they neglect the detailed particle microdynamics and treat the particle assembly as a continuum media. The motions of the continuum are governed by the common physical equations of mass, momentum and energy conservation together with a particular constitutive law for describing the characteristics of granular material. Many such constitutive laws have been proposed for the dense granular flow previously (Jop et al., 2006) and some of them were also applied to the CBM (Khalilitehrani et al., 2013, 2014, 2015). More Recently, an Eulerian FEM approach based on Mohr-Coulomb elasto-plasticity (MCEP) theory has been employed to simulate several common industrial processes (Zheng and Yu, 2014, 2015a,b), and satisfactorily reproduced the stress and flow characteristics in different systems. In theory, continuum modelling of mixing process should embody the correct mixing mechanisms. Bridgewater (Bridgwater, 2012), elucidated three primary mixing mechanisms of particle mixing in usual mixer systems. The most common way of mixing is convection which transfers groups of particles from one location to another as attached?clumps following the flow field. An alternative mechanism, i.e. shear mixing, is characterized by the

considerable slip zones at locations of high velocity gradient, which effects a continuous extension of the interfacial areas between the two groups of particles. The third mechanism, diffusion, roots in the frequent particle collisions that cause particles penetrating into other domains stochastically. To account for such a mixing description, an extra scalar transport equation is usually needed to couple with governing equations of particle flow in a continuum approach (Nguyen et al., 2014). Nonetheless, as the most important mixing mechanism (Bridgwater, 2012), the convective flow, is of fundamental significance to the mixing process and lays the basis for understanding particle shear and diffusion, and hence is therefore focused in this paper.

This work utilises the recent Eulerian FEM model (Zheng and Yu, 2014, 2015a,b) to investigate the flow and the mixing processes of cohesionless particles in a CBM. The conventional MCEP model is selected for description of granular flow for its simplicity and less empirical parameters. The simulated results including bed pattern, velocity distribution, and mixing index are presented in section 3.3 and compared with DEM and experimental outcome when possible. The complicated effects of model parameters such as the internal friction angle on flow and mixing behaviours are also discussed based on the FEM results.

3.2 Theory and numerical simulation method

3.2.1 Governing equations

The granular materials within CBM are treated as a continuum medium in view of the fact that the size of a CBM is far larger than the average size of particles. Similar to other forms of matter, the flow of a granular material also needs to satisfy the fundamental principles of conservation of mass, momentum, and energy, as written below:

Mass conservation,

$$\frac{\partial \rho}{\partial t} + \nabla \cdot (\rho v) = 0 \tag{3.1}$$

Momentum conservation,

$$\frac{\partial (\rho \boldsymbol{v})}{\partial t} + \nabla \cdot (\rho v \otimes \boldsymbol{v}) = \bigtriangledown \cdot \boldsymbol{\sigma} + \rho \boldsymbol{b} \tag{3.2}$$

and energy conservation,

$$\frac{\partial \epsilon}{\partial t} + \nabla \cdot (\epsilon \boldsymbol{v}) = \boldsymbol{\sigma} : \dot{\boldsymbol{\varepsilon}} \tag{3.3}$$

where ρ refers to the bulk density of granular material, $\boldsymbol{\sigma}$ is Cauchy stress tensor, $\boldsymbol{b}$ is the body force, $\boldsymbol{v}$ is the velocity vector and ϵ is the internal energy per unit volume. $\dot{\boldsymbol{\varepsilon}} = (1/2)\nabla\boldsymbol{v} + (\nabla v)^T$ represents the strain rate.

3.2.2 Mohr-Coulomb elastoplastic theory

Granular flow in the dense region can be viewed as a continuum flow characterised by elesto-plastic behaviours, which has been demonstrated under various constitutive laws and geometry circumstances such as pressure dip in a hopper flow (Zheng and Yu, 2014), granular eddies in a chute flow, and JiangLiu granular elasticity law (Jiang and Liu, 2003). Mohr-Coulomb plasticity was the simplest continuum model widely applied in granular materials for industrial purposes, however, its shortcomings were illustrated by a series of publications (Kamrin, 2010). One prominent disadvantage is that the model attributes most of characteristics of granular matter yield condition into a single internal friction angle. By demonstrating various properties of granular flows, a series of models with constitutive laws were established (Henann and Kamrin, 2013). However, it is less convincing and necessary to add extra degrees of freedom and parameters into the model, because most physical hypotheses introduced stay at the level of phenomenology which is lack of physical insight and first principle calculations. The consequence is the hinderance of seeking the real reason for certain granular phenomenon and making the whole continuum granular theory bloated. Recent investigations indicate that Mohr-Coulomb plasticity is still valid under certain circumstances and appropriate numerical simulations (Zheng and Yu, 2014, 2015a,b), which makes the additional phenological theories unnecessarily useful. With fewer parameters involved, we hope to use the minimum and powerful model (classic Mohr-Coulomb elasto-plastic model) to capture most of major features with respect to complex granular phenomena in containers of various geometries.

A linear relation between stress and elastic strain is adopted as:

$$\sigma_{ij} = D^{el}_{ijkl}\epsilon^{el}_{kl} \tag{3.4}$$

where σ_{ij} is the total stress; ϵ^{el}_{kl} is the elastic strain; and D^{el}_{ijkl} is the fourth-order tensor of elasticity.

The yield condition is given by:

$$R_{mc}q - p\tan\varphi - c = 0 \tag{3.5}$$

where

$$R_{mc} = \frac{1}{\sqrt{3}\cos\varphi}\sin(\Theta + \frac{\pi}{3}) + \frac{1}{3}\cos(\Theta + \frac{\pi}{3})\tan\varphi$$

φ is the slope of the Mohr-Coulomb yield surface in the $p - R_{mc}q$ stress plane, which is commonly referred to as the friction angle of the material and can depend on temperature and predefined field variables. $p = -\frac{1}{3}\mathrm{trace}(\sigma_{ij})$ is the first invariant of stress representing the equivalent pressure; $q = \sqrt{\frac{3}{2}S_{ij}S_{ij}}$ is the Mises equivalent stress and S_{ij} is the deviatoric stress; φ and c are the angles of internal friction and and the cohesion of granular material, respectively. Θ is the deviatoric polar angle defined as $\cos(3\Theta) = (r/q)^3$ where $r = (\frac{9}{2}S_{ji}S_{jk}S_{ki})^{\frac{1}{3}}$ is an invariant measure of deviatoric stress. The friction angle, φ, controls the shape of the yield surface in the deviatoric place. The friction angle range is $0° \leq \phi < 90°$. In the case of $\phi = 0°$ the Mohr-Coulomb model reduces to the pressure-independent Tresca model with a perfectly hexagonal deviatoric section. In the case of $\phi = 90°$ the Mohr-Coulomb model reduces to the "tension cutoff" Rankine model with a triangular deviatoric section and $R_{mc} = \infty$.

Granular flow can be well described as flow rules. The flow potential G is chosen to be a hyperbolic function in the meridional stress plane and a smooth elliptic function in the deviatoric stress plane, defined by:

$$G = \sqrt{(\epsilon c\mid_0 \tan\psi)^2 + (R_{mw}q)^2} - p\tan\psi \tag{3.6}$$

and

$$R_{mw} = \frac{4(1-e^2)\cos^2\Theta + (2e-1)^2}{2(1-e^2)\cos\Theta + (2e-1)\sqrt{4(1-e^2)\cos^2\Theta + 5e^2 - 4e}} \times \frac{3-\sin\varphi}{6\cos\varphi} \tag{3.7}$$

where ψ is the dilatancy angle of material, $c|_0$ is the initial cohesion yield stress, ϵ is a parameter that characterizes the eccentricity of the flow potential; and e referred to as the deviatoric eccentricity describing the "out-of-roundedness" of the deviatoric section in terms of the ratio between the shear stress along the extension meridian and the shear stress along the compression meridian, is a function of the internal friction angle φ, given as $e = (3 - \sin\varphi)/(3 + \sin\varphi)$.

An additive strain rate decomposition is assumed:

$$d\boldsymbol{\varepsilon} = d\boldsymbol{\varepsilon}^{el} + d\boldsymbol{\varepsilon}^{pl},$$

where $d\boldsymbol{\varepsilon}$ is the total strain rate, $d\boldsymbol{\varepsilon}^{el}$ is the elastic strain rate, and $d\boldsymbol{\varepsilon}^{pl}$ is the inelastic (plastic) strain rate.

The constitutive flow rule can be written as:

$$d\boldsymbol{\varepsilon} = \frac{d\boldsymbol{\varepsilon}}{g}\frac{\partial G}{\partial \boldsymbol{\sigma}},$$

where g can be written as

$$g = \frac{1}{c}\boldsymbol{\sigma} : \frac{\partial G}{\partial \boldsymbol{\sigma}}$$

3.2.3 Coupled Eulerian-Lagrangian method of FEM

In the Eulerian FEM, the nodes of material are fixed so that the meshes are not distorted and material flows through the meshes freely. The algorithm to realize the performance is known as Lagrange-plus-remap. More details can be found in (Zheng and Yu, 2014). The coupled Eulerian- Lagrangian method allows interactions and interprets a good contact condition between rigid body of lagrangian part and materials set up as Eulerian part. In our simulation, the whole rigid body including the rotating blades and the exterior wall is completely immersed in the Eulerian meshes as Fig.3.1 shows.

3.2.4 Simulation conditions

The considered setup of CBM is shown in Fig.3.1 , similar to that adopted in previous experiment (Stewart et al., 2001; Zhou et al., 2004) and DEM simulation (Zhou et al., 2004). It comprises a cylindrical container of inner diameter 249mm, a fixed axial shaft of diameter 32mm, and two identical flat blades of 40 mm high and 10 mm thick. The container and the blades are modelled as Lagrangian parts (element type R3D4) in the FEM simulation. The cohesionless particles regardless of size and shape are treated as a

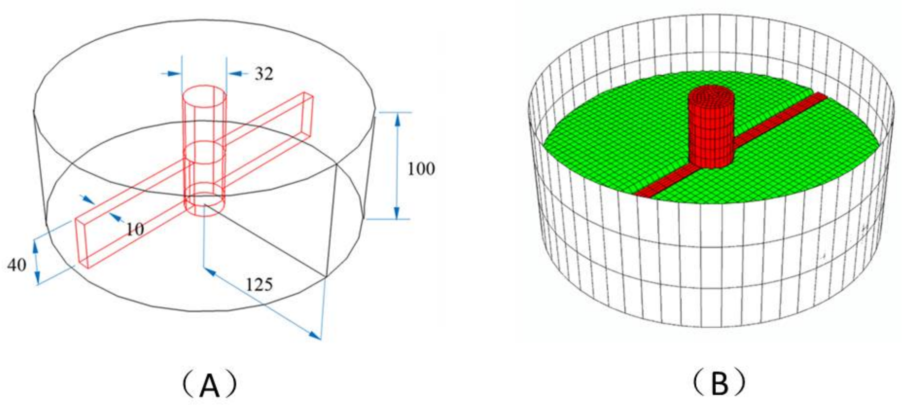

Figure 3.1: (A) The geometry of CBM under consideration; (B) computational mesh for FEM modelling (Eulerian mesh is set to be transparent so that the inside blade and drum can be sighted).

Parameters	Symbols	Basic values	Range of variation
Particle density	ρ	$1500kg/m^3$	-
Poisson's ratio	ν	0.3	-
Young's modulus	E	1×10^6	-
Internal friction angle	ϕ	$15°$	$10°$-$35°$
Friction coefficient of material-wall interaction	μ	0.3	0.1-0.5
Dilation angle	Ψ	0.1	-
cohesion yield stress	c	0	-

Table 3.1: Physical parameters used in the simulation

continuum Eulerian fluid (element type EC3D8R). As shown in Fig 3.1, these Lagrangian parts should be totally immersed in the Eulerian meshes in order to contact with the granular materials. For clarity, Fig 3.1 shows the cross-section of a coarse Eulerian mesh only; the mesh size adopted in computation is approximately 0.5 cm. The Eulerian meshes are assigned with materials at the initial step. An Eulerian Volume Fraction (EVF) is defined to calculate the volume fraction of material occupying the elements. The parameters to characterize material property are listed in Table 3.1. The initial height of granular bed is equivalent to the top of blades. The simulation starts with blades rotating about the shaft at an angular velocity of 1 rad/s. The Eulerian elements are fixed in space and time while the materials are pushed through them by the rotating blades. More details about the algorithm can be found elsewhere (Zheng and Yu, 2014). The whole simulation lasts for at least 10 seconds until the fluctuation of system kinetic energy becomes negligible, in other words, when granular flow arrives at a steady state. Information of various physical quantities is then collected at this state.

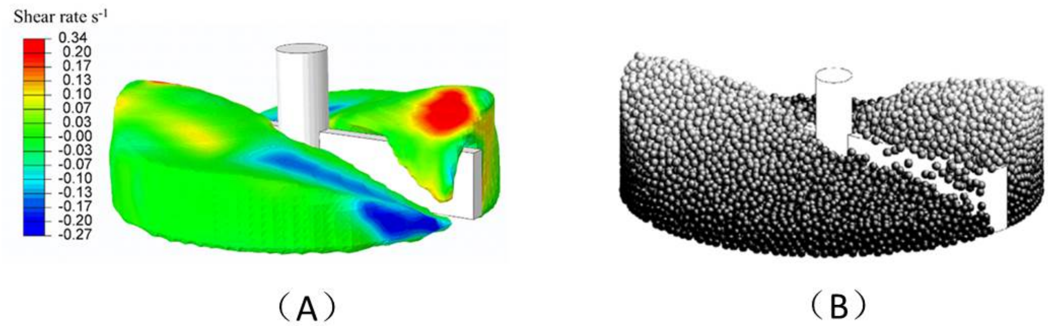

Figure 3.2: A comparison of the bed profiles between (A) FEM and (B) DEM (Zhou et al., 2004)

3.3 Results and discussion

3.3.1 Bed heaps

Fig.3.2 illustrates a typical profile of bed material in the simulated CBM. When stirred by the blades, the bed is forced to rotate about the central axis and forms two heaps in the front of blades. Such heaping phenomena have been commonly observed in previous PEPT experiment (Stewart et al., 2001) and DEM simulations (Chandratilleke et al., 2009, 2010). Note that as a consequence of the heaps, there are two obvious recirculating flow (RF) regimes in the vicinity of blades which considerably affect the mixing rate (to be discussed later).

The altitude of bed heaps is mainly determined by the internal friction angle φ. As displayed in Fig.3.3, bed profiles are obtained with different internal friction angles. The particle-wall friction coefficient μ equals to 0.3 for all the cases. The colour indicates the bed altitude in units of m, with a fixed friction coefficient μ, the heap height grows remarkably from around 0.08 m to 0.113 m as φ increases from 15° to 35°. Previous discrete studies (Stewart et al., 2001; Zhou et al., 2004) found that the heap height can also be promoted by enhancing the sliding friction coefficient μ_s between component particles. This finding is in principle consistent with the present FEM observations, because the inter-particle friction μ_s is to a large extent related to the internal friction angle φ although they are concepts of different scales. The flow bed profile can be different by changing the internal friction angle.

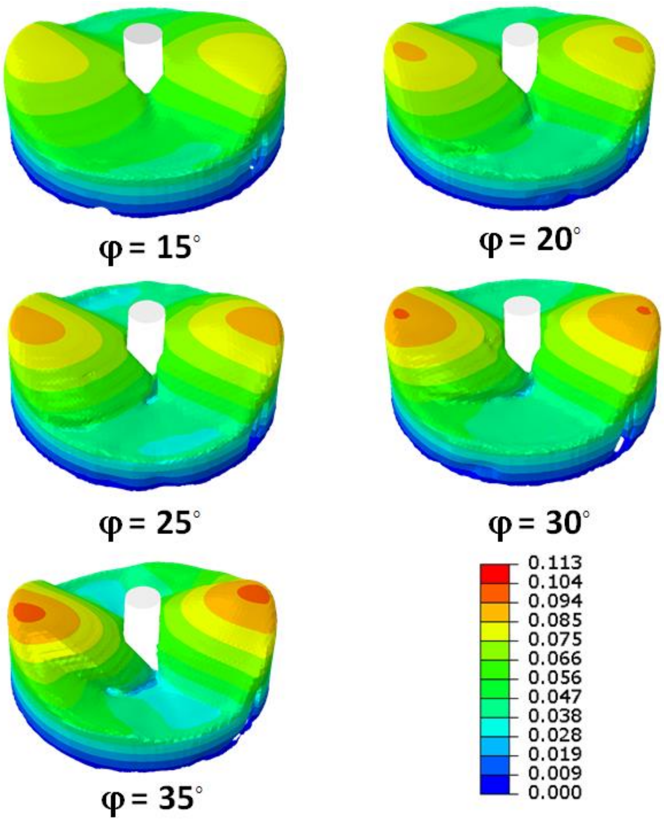

Figure 3.3: Bed profiles obtained with different internal friction angles. The particle-wall friction coefficient μ equals to 0.3 for all the cases. The colour indicates the bed height in units of m.

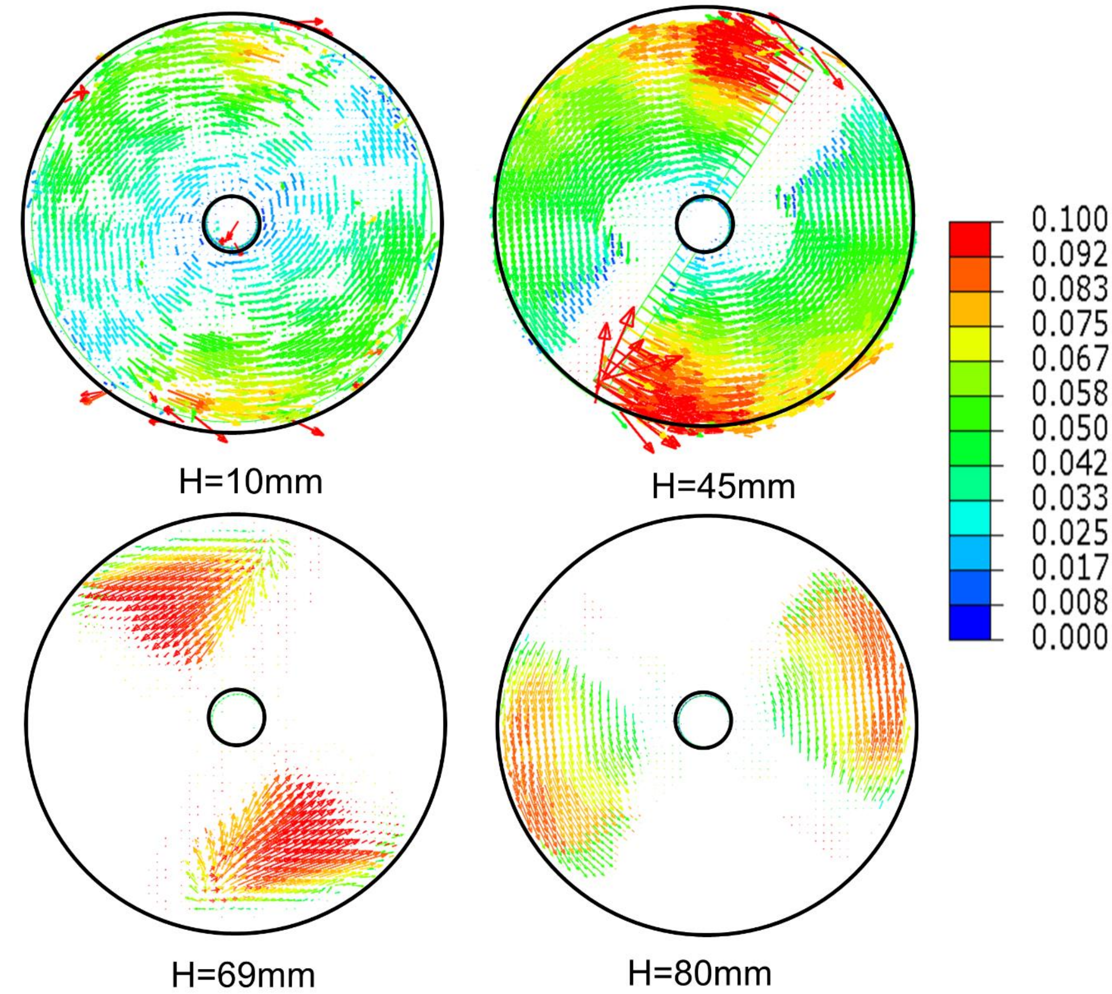

Figure 3.4: Velocity vectors in horizontal sections of different heights for $\mu = 0.3$. The colour indicates the velocity magnitude in units of m/s.

3.3.2 Velocity profile and distribution

Fig.3.4 depicts the translational velocities of particles in horizontal sections of different heights. As seen, in the lower areas such as H = 10 mm, the majority of particles flow in the same angular direction (counter-clockwise). The velocity reaches maximum at the front surface of blades where particles are subject to the strongest normal propelling force, and then gradually decreases with the distance from blades. The velocity distribution above the top of blades (up to 45 mm) is somewhat complicated, as the particles in this region can surmount the blades and flow in both directions, generating a recirculating flow velocity in the rear of the blades. At the top of the heap, however, particles flow in a variety of directions depending on the shape of heap, including an obvious radial flow at the perimeter (H = 45 mm and H = 69 mm). The vertical distribution of velocity in

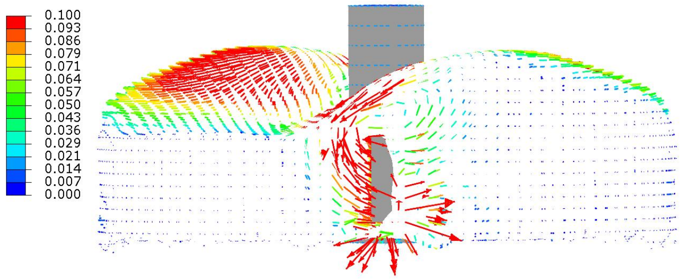

Figure 3.5: Recirculation pattern of the velocity field in FEM simulation. The colours denote the magnitude of velocity in units of m/s.

the immediate area of blade is illustrated in Fig.3.5. As seen, the majority of particles in this area are propelled to move forward while a small proportion of particles near the surface move back in a counter-clockwise vortex manner, forming a similar recirculating flow (RF) pattern to the previous DEM observations (Zhou et al., 2004). Those particles flowing downward can either end in laying on the bed surface or re-joining the forward flow along with the particles behind.

Velocity statistics is a common way to quantitatively evaluate the flow field in many granular flow systems. Analogous to the treatment in previous work (Zhou et al., 2004), the following velocity frequency density is defined in our analysis:

$$f(V_i) = \frac{number \quad of \quad nodes \quad \in [V_i, V_j + \triangle V]}{total \quad number \quad of \quad nodes} \times \frac{1}{\triangle V} \tag{3.8}$$

, where V represents certain velocity measure under investigation, such as resultant velocity $V_m = \sqrt{V_x^2 + V_y^2 + V_z^2}$, radial velocity $V_r = V_x \cos\alpha + V_y \sin\alpha$ or tangential velocity $V_t = V_y \cos\alpha - V_x \sin\alpha$, where $\alpha = \arctan(y/x)$, x and y are the coordinates of particles on X-Y plane. $\triangle\ V = 0.004\ m/s$ is the velocity interval designated in statistics. Note that all the FEM data are retrieved from the nodes of Eulerian elements and the statistics is performed on the number of element nodes that are occupied by the granular material (neglecting the void elements).

Fig.3.6 shows the probability distributions of velocities V_m in the rotated particle bed. Different values of internal friction angle φ and wall friction μ are used because the two variables significantly influence the collective behaviours of particles at macroscopic scale. It is observed that for small internal friction angle $\varphi = 25°$, the speed curve peaks at a very low value $V_m < 0.01$ because most particles keep inertial in this case. As φ increases and

μ keeps constant, the apex of velocity distribution becomes less sharp and shifts gradually from the lower-valued speed side to higher-valued side, indicating an increasing number of particles entering into the flowing regime. By contrast, if φ stays unchanged and wall friction μ increases, the proportion of high-speed particles within the system will decline oppositely as seen from Fig.3.6 (B). Such distributions bear a high resemblance to the trend in DEM results (Zhou et al., 2004) when the sliding friction coefficient μ_s between particles is reduced. Moreover, the FEM and DEM data can agree quantitatively when the values of parameter φ and μ are properly adjusted as shown in Fig.3.7. Note that in cases of extremely great internal friction angle such as $\varphi = 89°$ (Fig.3.6 (A)) or tiny wall friction, e.g. $\mu_s = 0.1$ (Fig.3.6) and $\mu = 0.0001$ (Fig.3.6), there is an evident linear correlation between speed frequency f(V) and speed V. This pattern in fact corresponds to a special flow state where all particles move at the same angular velocity about the CBM axis like an integral solid adhering to the blades. According to the MCEP theory, granular material will behave like solid where the critical incipient failure state $\tan\varphi < \tau/\sigma$ (τ and σ are the respectively shear stress and normal stress exerted on the element) is not satisfied. Hence the larger φ, the more materials staying at solid/elastic state. For sufficiently large φ, the entire bed will move as a rigid solid without any heaps or recirculation. Likewise, if the frictional resistance from CBM walls is too small, the bed material will also rotate freely as a rigid body. Under both circumstances, the translational velocities are simply along the tangential direction and proportional to the radial coordinates in magnitude. Assuming that the effective angular velocity of bulk bed is ω_b and the translational velocity at certain radial position r is v_r, the velocity frequency density in this particular condition can be found from

$$f(V_i) = \frac{number \quad of \quad particles \quad \in [V_i, V_j + \triangle V]}{total \quad number \quad of \quad particles} \times \frac{1}{\triangle V} \tag{3.9}$$

, given by

$$f(v_p)\mathrm{d}v_p \quad = \quad \frac{\mathrm{d}N_p}{N_{total}}$$

, where N_p indicates the number of particles within the range $v_r dv_r$ and N_{total} is the total number of particles in DEM simulation. In FEM, N_p and N_{total} represent the number of element nodes as mentioned above.

This situation can be considered as two dimension owing to the uniformity of velocity along the bed depth. Hence, $dN_p = 2pr\pi dr$ and $N_{total} = \pi R^2 \rho$ where R is the radius of mixer and ρ is the bulk density, and the following linear relationship between the frequency density and the velocity can be derived:

$$f(v_r) = \frac{2}{\omega_b^2 R^2} v_r$$

This equation explains the linear distributions of resultant velocity shown in Figs.3.6 and 3.7, that is, those cases all correspond to a uniform angular flow state. By Eq.3.10, we can also infer the effective angular speed of whole bed about shaft. Taking the case $\varphi = 89°$ and $\mu = 0.3$ in Fig.3.6 (A) as an example, the slope of $f(v_r)$ versus v_r is approximately 150. Recalling the geometric parameters R = 0.125 m, the bulk angular velocity is found to be $\omega_b = 0.92$ rad/s. In another case of $\varphi = 50°$ and $\mu = 0.0001$ (Fig.3.6), the bulk angular velocity is estimated as $\omega_b = 1.03$ rad/s via the same method. By and large, both values are equal to the applied blade rotating speed 1 rad/s.

Fig.3.8 illustrates the statistical distributions of the radial velocity component V_r and tangential component V_t. The radial velocity within CBM is generally small and distribute only in a narrow regime. But with the increase in φ, particles are increasingly involved in the radial flow of RF region, which in turn creates a slightly wider distribution of radial velocity, just as observed in previous DEM study (Zhou et al., 2004). For internal friction angle $\varphi \geq 30°$, the collective particles tends to rotate as a rigid solid as discussed above and the tangential velocity V_t becomes the major composition of resultant velocity V_m. As such, the average value of tangential velocity V_t shows a considerable increase with φ while the majority of radial velocities V_r fall gradually to almost zero.

3.3.3 Mixing kinetics

Mixing pattern evolution

Mixing occurs when more than two kinds of particles occupy one detection cell. To model this behaviour, a state variable c_r is defined to represent the concentration of particles in each FEM mesh, with $c_r = 1$ for meshes full of red particles, $c_r = 0$ for those of blue particles and $c_r = 0.5$ representing a complete mixing state. It should be emphasized that the colours here only serves as identifiers of different parts of the bed rather than different

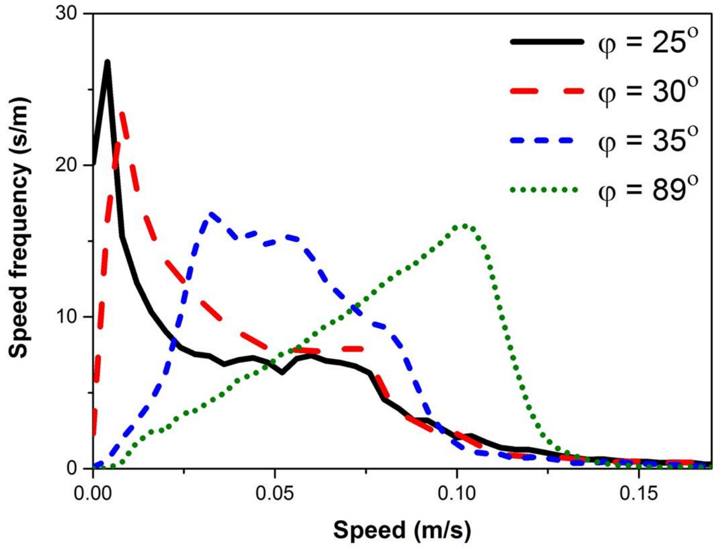

(A)

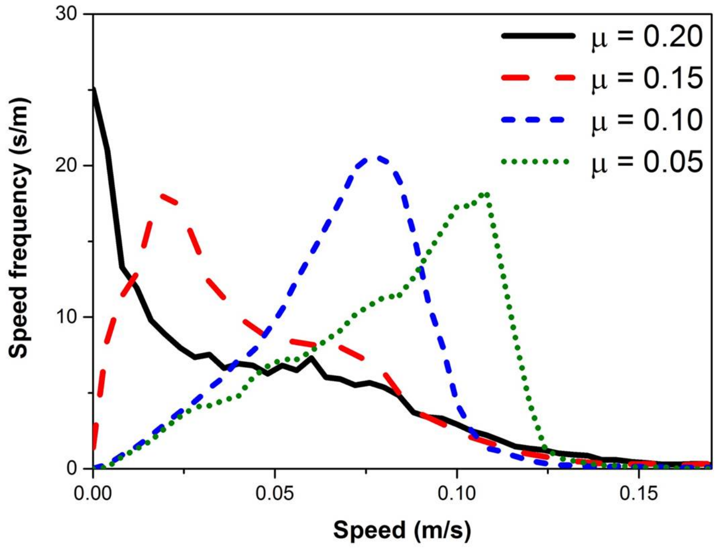

(B)

Figure 3.6: Statistical distributions of the particle velocity V_m for different material parameters when (A) $\mu = 0.3$; (B)$\varphi = 15°$.

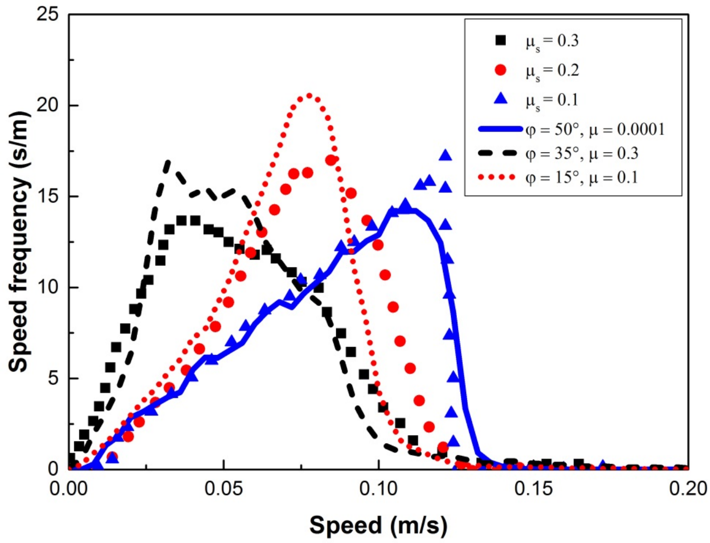

Figure 3.7: Comparison of the velocity statistical distributions obtained by FEM and DEM. Note that μ_s is the inter-particle sliding friction coefficient used in DEM (Zhou et al., 2004) while μ indicates the macroscopic friction between bulk material and CBM components in FEM modelling.

materials-both red and blue parts in effect have the same physical properties given in Table 3.1. In FEM simulation, the initially apart red and blue material points may come close as a result of the evolving flow field and mix with each other. An additional principle is applied implicitly, i.e. that assumingly the materials are immediately uniformly mixed in each individual mesh irrespective of the mesh size. This in essence endows the flow process with an artificially diffusional characteristic, without which the boundary between materials would never disappear, however lengthy and curly it becomes, just like the mixing picture of fluids (Ottino, 1990). Such a treatment is in general reasonable although as shown momentarily it may introduce an undesirable mesh-dependency of mixing rate. Fig.3.9 shows the simulated mixing patterns at different stages. The materials of different colours are separated by the blades at t = 0 s. Shortly after the blades start rotate, a clear S-shaped boundary shows up between the two bulks and then two small RF regions in green colour ($c_r = 0.5$) emerges at 4.5 s indicating a the commencement of solid mixing. With the continuing rotation of blades, the green regions grows slowly and eventually expand to the whole bed at t = 18s, indicating that the system has reached an overall homogeneous mixing state.

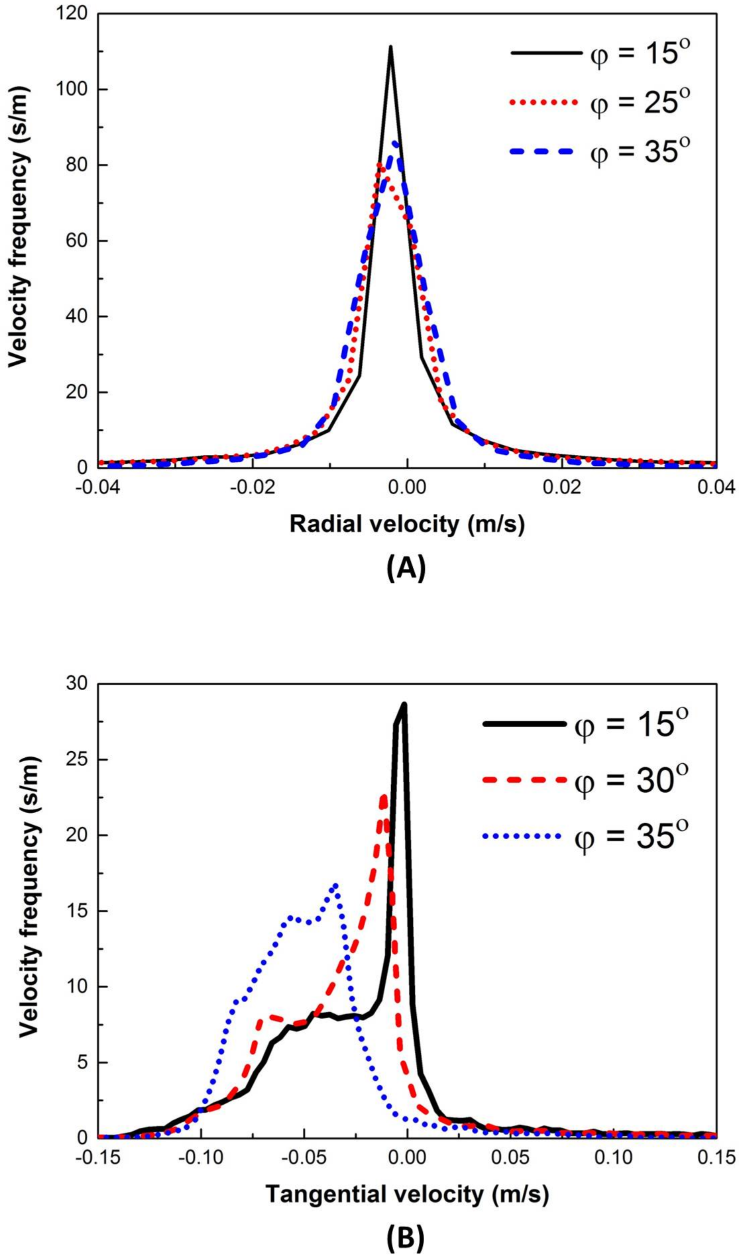

Figure 3.8: Radial and tangential velocity distributions at different φ when $\mu = 0.3$.

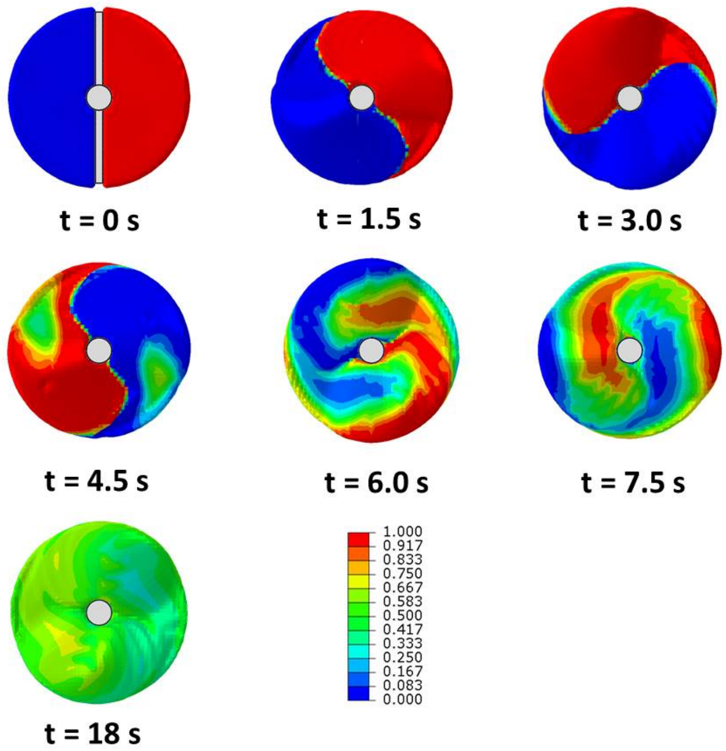

Figure 3.9: Top view of Mixing patterns at different time steps for $\varphi = 15°$, $\mu = 0.3$. The colour denotes the concentration of red particles c_r.

Mixing mechanisms

This subsection presents a detailed investigation into the mixing mechanism based on the FEM results. Since the particle diffusion is not rigorously considered in FEM modelling; only the convective and shear mixing related to macroscopic solid movement are focused here. Fig.3.10 shows a lateral view of the mixing process at times 3.75 s and 4.5 s respectively. At 3.75 s, the red materials start to overlap the blue ones due to the existence of velocity gradient, creating a narrow slipping and mixing zone (in green colour), which is commonly observed and recognized as the characteristics of shear mixing in centrifugal mixers (Bridgwater, 2012). This shear-induced mixing may expand slowly with time but is overall localised to the interfacial regime where two kinds of substance contact. Very poor mixing can be attained outside the regime at this stage. A better mixing zone appears at 4.5 s in the rear of blade as depicted in Fig.3.10 (B), which corresponds to the RF regime discussed in Sec.6.2. This is because particles in this regime undergo rapid and complex motions as shown in Fig.3.5, and thus have greater chances of meeting others in one mesh and blending. The critical importance of RF zone for mixing was also found in a previous

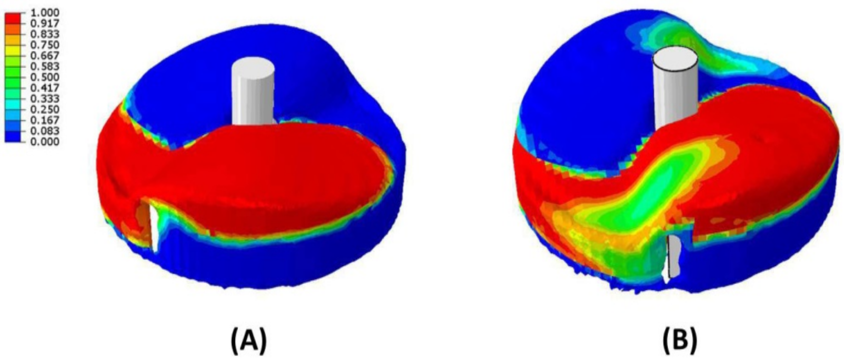

Figure 3.10: A lateral view of mixing at (A) 3.75 s; (B) 4.5 s. The parameters used are identical to those in Fig.3.9.

study on the influences of mixer geometries (blade rake angle and gap) (Chandratilleke et al., 2009).

In fluid mixing, the interfacial area between different fluids is a commonly studied fundamental quantity which reflects how the fluid stretch and fold during the mixing process (Zhendong et al., 2012). This concept is also adopted here to ascertain the respective contributions of shear and RF zones to the mixing efficiency. The interfacial area per unit volume of the layers is given by (Ottino, 1990) $a_V(x,t) = lim_{V \to 0} \frac{S}{V}$, where S is the interfacial area between fluid layers within the volume V enclosing point x at time t. For the total system, $a_V = \int a_V(x,t)dx$ and is independent of space. By definition, a larger a_V represents a better mixing. Technically in our modelling, we take the interfacial area as the number of nodes that have c_r values within the range $0.49 < c_r < 0.51$, N_{inter}. Fig.3.11 shows the mixing pattern in case of $f = 15°$ and $\mu = 0.1$, where the recirculation flow is suppressed by the use of small wall friction and therefore shear plays the dominant role in the mixing process. The S-shaped interface stretches and becomes larger with time but it changes at a quite lower rate for a long period. Even until 28.8s, the system is still far from being well mixed. As shown in Fig.3.12 (A), N_{inter} increases linearly with time in this case. In contrast, in case that the recirculation becomes dominant (e.g. $\varphi = 15°$ and $\mu = 0.3$), N_{inter} increases more rapidly as an exponential function of time (Fig.3.12 (B)). The emergency of exponential behaviour in Fig.3.12 (B) ($t \approx 5s$) coincides in time with the appearance of RF zone shown in Fig.3.10 (B) ($t \approx 4.5s$).

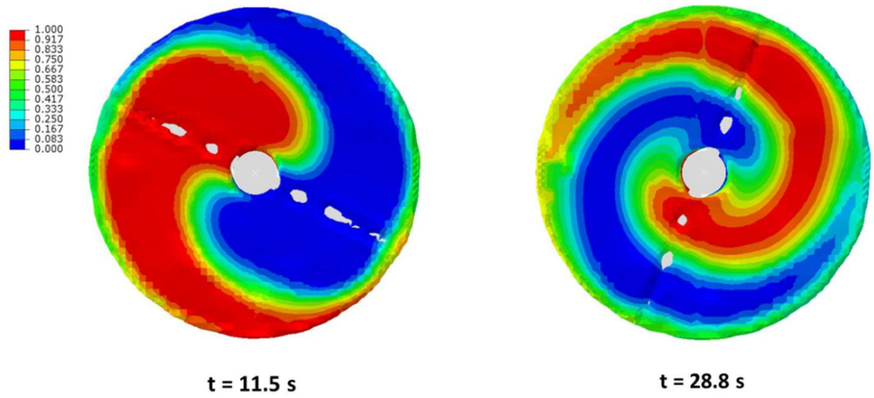

Figure 3.11: Bottom view of mixing patterns when $\varphi = 15°$ and $\mu = 0.1$.

Mixing index

Mixing index characterizes quantitatively the extent of particle mixing, with values between 0 (totally segregated state) and 1 (fully mixed state). Lacey (Zhou et al., 2004) proposed a popular index based on the local sampling variance, which is however mainly suitable for discrete studies. In this continuum study, the intensity of mixing proposed for characterizing the liquid mixing efficiency (Zhendong et al., 2012) is selected as the mixing index, written as

$$M \quad = \quad 1 - \sqrt{\frac{\sigma^2}{\sigma_{max}^2}}, \tag{3.10}$$

,where σ is defined as:

$$\sigma \quad = \quad \sqrt{\frac{1}{N}\sum_{i=1}^{n}(c_i - c_m)^2}, \tag{3.11}$$

N is the total number of sampling points. c_i is the concentration of particle at the sampling point i. $c_m = 0.5$ is the optimal mixing fraction, which also stands for the average concentration of the whole material assembly. σ is the standard deviation of concentration at certain time, and σ_{max} is the maximum standard deviation during the whole mixing process. M equals 0 at the initial stage when particles are completely separated ($\sigma = \sigma_{max}$) and equals 1 at the final homogeneous mixed state ($\sigma = 0$). In our work, the sampling points are taken as the computational grids of FEM meshes, so the value of M may be affected by the mesh density as discussed in the following section.

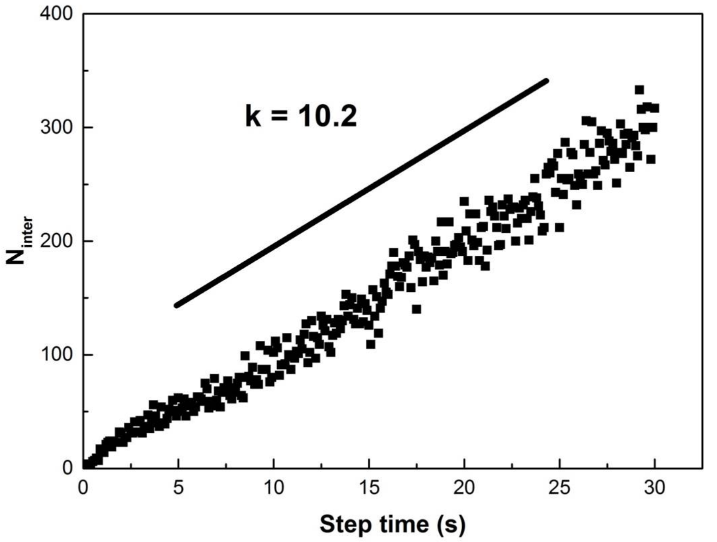

(A)

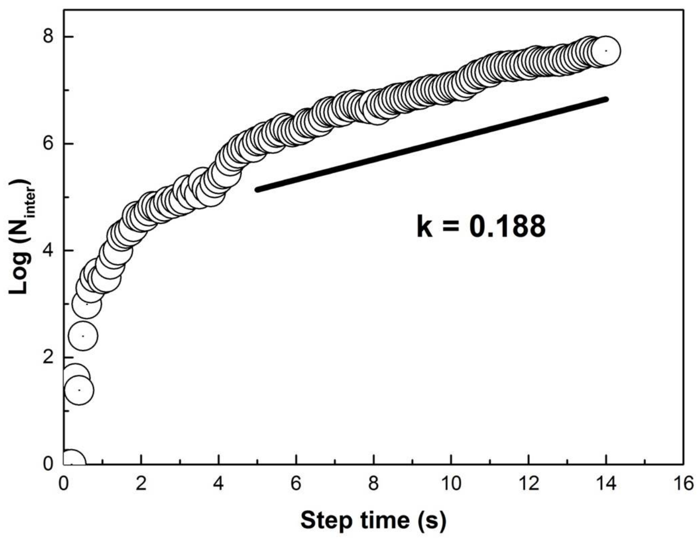

(B)

Figure 3.12: (A) Variation of interfacial area between the two species in case of $\varphi = 15°$ and $\mu = 0.1$; (B) The logarithm of interfacial area when $\varphi = 15°$ and $\mu = 0.3$.

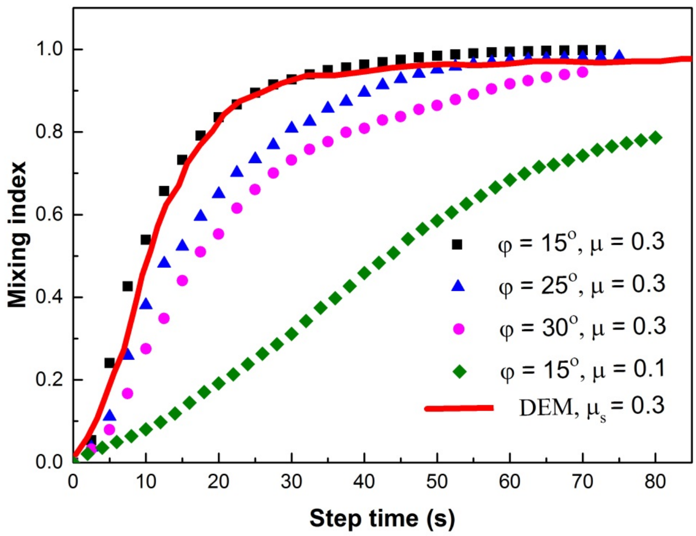

Figure 3.13: Mixing index as a function of time. DEM result is from ref. (Zhou et al., 2004)

Fig.3.13 plots the increasing mixing index as a function of time. It is seen that the obtained mixing index with $\varphi = 15°$ and $\mu = 0.3$ agrees well with that by DEM when $\mu_s = 0.3$, although the definitions of mixing index M are slightly different. The mixing index in other cases also exhibits a similar trend to the DEM data, rising dramatically at the first few seconds and then slowly approaches the plateau value 1.0. The increase rate of M appears to be substantially affected by the internal friction angle φ and wall friction μ. In preceding Fig.3.6, we demonstrate that the increase of φ can speed up the particle motions in CBM; however, such effect mainly enhances the uniform rotation of entire bed about the shaft but on the other hand weakens the convective flow inside bed and the mixing rate. The mixing rate is the poorest in case $\varphi = 15°$ and $\mu = 0.1$, which, as illuminated in Sec.3.3.3, is mainly driven by the shear mixing at the interface of bulk solids. This confirms again that the interface shear is less effective than convection in mixing particles.

Influence of mesh size

The choice of mesh size can influence the characterization of mixing in many ways. Even in physical experiment or discrete modelling (Liu et al., 2013a), how to select an appropriate mesh for computing mixing index is still an open question, much depending on the scale of studied system and particle size. This is apparently an important issue because technically there will be zero mixing if the mesh size is too small to accommodate more than two particles, or invariably complete mixing if the cell is so large that all particles are included. In previous CFD simulation, the mesh density was also found to significantly influence the fluid mixing process in a micro-mixer (Zhendong et al., 2012). This section aims to illustrate the mesh size effect in our FEM simulation. Fig.3.14 shows the mixing rates yielded by FEM with different mesh densities. Apparently, the fine mesh produces a slow mixing rate in FEM modelling, much similar to the observations in previous CFD simulation of fluid mixing (Zhendong et al., 2012). The problem is mainly because the continuum approaches always consider the materials in a mesh as uniformly mixed, irrespective of their detailed spatial distribution below the mesh scale. Hence a particle assembly may be regarded as a good mixture in a coarse mesh but may not in a fine mesh. Fig.3.14 gives an example to elucidate this issue. Suppose c_r reaches 0.5 in coarse element (inset A) while there are actually many different states of particle arrangements if the coarse mesh is further decomposed into more fine elements, such as the one represented by insets B and C. In case B, the particles can be still deemed as homogeneously mixed since the standard deviation σ is unchanged. By contrast, the particles in case C are completely separated and σ becomes larger than case A, although the nominal values of concentration c_r within this domain are the same. Therefore, coarse mesh tends to overlook the particle separations more easily and leads to a faster mixing rate, which introduces some uncertainties into continuum predictions of mixing. One possible resolution to this problem is by introducing a diffusion equation to physically control the propagation/rate of mixing within individual mesh, replacing the instant mixing mechanism implicitly embodied in current simulations. In practice, the mesh size should be carefully selected in light of the system scale, particle size and the diffusional rate as well as the sustainable computational costs because simulation with fine mesh can be fairly time-consuming.

3.4 Conclusions

A numerical study of the flow and mixing process within a cylindrical blade mixer is performed by means of Eulerian FEM approach. Focused on cohesionless particles, this work investigates various features of the blade mixer including the profile of particle bed, the

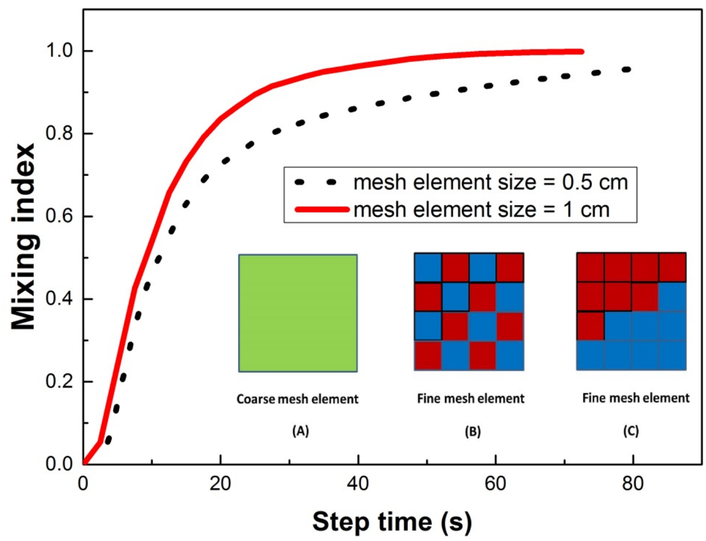

Figure 3.14: Mesh element size effect. The case is selected as $\varphi = 15°$ and $\mu = 0.1$.

recirculation flow pattern, the mixing index and their dependencies on material properties such as internal friction angle φ and particle-wall friction coefficient μ. The following conclusions can be drawn from this study:

- The formation of heaps in front of blades associated with the counter-wise recirculation flow is the main reason of mixing in a cylindrical blade mixer. It produces an exponential increase in the total interfacial area between two mixed solids and thus a quick mixing rate. Without such heaps, the interfacial area rises only linearly with mixing time. This is because the heaps create a localised vortex flow field enhancing the chance of contact of different materials. It would be beneficial to encourage such vortex flow in practical applications by adjusting the blade height and angle.

- Material characteristics such as internal friction angle and wall friction significantly influence the performance of mixer. Different material parameters generate completely different flow behaviours and mixing efficiency. Those materials with large internal friction angle mobilise in the system more like a solid and hence are more difficult to mix. Wall friction, on the other hand, can prevent such rigid solid motion and promote particle mixing.

- By properly selecting material parameters, FEM modelling can well reproduce the velocity fields and mixing index measured in previous DEM work. It can also agree with the theoretical results yielded under a special condition. This method may help to overcome the scale-up issues in bulk solid handling industries owing to its high simulation speed. However, some challenges exist in this method: a) a physically sound law describing the diffusional mixing of particles is still absent, and b) the obtained mixing rate depends heavily on the size of computational mesh. These aspects are important to the quantitative accuracy of FEM approach and require more studies in future.

3.5 Nomenclature

ϱ	bulk density of granular material $[kg/m^3]$
E	Young's modulus [Pa]
ν	Poisson's ratio [-]
φ	internal friction angle [degree]
c	shear cohesion [Pa]
μ	Coulomb friction between granular material and drum wall [-]
μ_s	sliding friction coefficient in DEM simulation [-]
H	height of granular flow bed [m]
V	velocity of granular material [m/s]
V_m	resultant velocity of granular material [m/s]
V_r	radial velocity of granular material [m/s]
V_t	tangential velocity of granular material [m/s]
$\triangle V$	statistical velocity interval of granular material [m/s]
f (V)	statistical speed frequency [s/m]
ω_b	angular velocity of bulk bed [1/s]
v_r	translational velocity at certain radial position r [m/s]
N_p	number of particles within the range $v_r dv_r$ [-]
N_{total}	total number of particles in DEM simulation [-]
R	radius of mixer [m]
N_{inter}	interfacial area in form of number of nodes [-]
M	Mixing index [-]
σ	standard deviation of concentration [-]

Chapter 4

Development and validation of a FEM-based convection-diffusion model for granular mixing

4.1 Introduction

Mixing of granular materials is commonly seen and widely applied in many manufactory processes such as the production of tablets and capsules in pharmaceutical areas, the production of composite materials with high hardness in powder metallurgy, plastic and cosmetics. During the mixing process, the flowing particulate material can go through a very complex process due to the collective motion of a great number of particles. It is essential to simulate and understand those complicated behaviours for a better designing of practical mixers. Among the various mixers, rotating drums partially filled with particles are the commonly used mixer in industry for mixing, granulation, grinding and calcination. Complicated granular flows regimes such as avalanching, rolling, cascading, cataracting, and centrifuging are observed experimentally and numerically in the rotating drums (Yang et al., 2003, 2008). So drums are ideal mixers to carry out simulations and test new hypotheses in theory and new methods in model development.

However, in terms of the traditional discrete element method (DEM) in simulation, the scale problem can always be encountered when a group of granular particles are treated individually. Consequently the numerical simulation with DEM can only be tested and proceed in mixers within a small scale, such as the bladed mixer with the diameter of approximate 10 cm in which a limited number of particles are simulated.

Continuum approaches are an another way to solve the scale up problem. Various continuum approaches are proposed in the history of granular flow investigation. The simplest model is the geometrical model studying avalanche flow in a 2D drum (Metcalfe et al., 1995b). The material in the drum is divided into many wedges which are transferred by a convection algorithm. The geometrical method is able to reproduce main features of mixing in a slowly rotating drum when avalanche happens. It provides a picture of understanding the mixing mechanism in a visual way. As the drum rotates more quickly for example in a rolling regime, a set of algebraic equations based on geometrical characters are established to describe the behaviors in the rolling region and stagnant part separately (Khakhar, McCarthy, Shinbrot and Ottino, 1997). In most complicated cases, An Eulerian-Eulerian multiphase mode based on kinetic theory is the most commonly used technique describing granular flows in complex mixers (Nguyen et al., 2014). The numerical calculations in those models are mainly based on the finite volume method widely applied in CFD. In the drum study (Santos et al., 2013), rolling, cascading, cataracting and centrifuging regimes can be identified by choosing appropriate types of kinetic theory, which demonstrates that the kinetic model can also be applied in the dense granular flow treatment. When granular flow becomes denser, many theories fail to achieve the description of complex behaviour of granular flow such as solid-liquid duality characterising the behaviour of sandpile. The Eulerian FEM based on Mohr-Coulomb elastoplastic (MCEP) model is a promising approach which has been tested and demonstrated well in simulating a wide range of complex granular phenomena (Zheng and Yu, 2014, 2015a,b). In (Zheng and Yu, 2015b), Slipping and slumping regimes are well reproduced by the FEM simulation. FEM accurately predicts some key aspects of the bed kinematics such as the linear increase of surface angle with Froude number and the linear distribution of velocity in the active layer. Applying this method to mixing problems is a tentative try in recent research where convection is the only mixing mechanism considered (Bai et al., 2017). Convection relying on particle flow is the most common way to transfer particles to different locations during which mixing happens. For most mixing processes, convection plays the dominant role and determines the mixing status. Another mechanism, diffusion, resulting from frequent particle collisions at the interface where two kinds of materials contact, causes the materials penetration, which enhances the mixing process at certain circumstances. The diffusion process is also important in some cases and should not be ignored in the mixing process. Therefore a general 3D FEM model coupled with diffusion is needed in the mixing simulation process. Diffusion can be implemented into the mathematical models via different ways such as by adding an extra term from diffusion equations into the fluid dynamics (Zhendong et al., 2012) or coupling the random walk mechanics from a microscopic perspective (Khakhar et al., 1999).

In this work, we develop the model by adding the diffusion term in the form of second-order differential equations into our FEM dynamics (Bai et al., 2017). The algorithm which couples diffusion with FEM convection will be represented in Sec.5.4. Since tumblers and stirrers are the most commonly used mixers for comparing data out of theories and experiments, a quasi-2D drum is selected to validate our model for its simplicity in geometry and easy comparison with data in previous work, which is demonstrated in Sec.4.2.6. A series of patterns as well as physical quantities such as mixing index from FEM will be studied in Sec.6.3.

4.2 FEM simulation conditions and the algorithm of convection coupled with diffusion

The Eulerian FEM simulation is used through out the work in this chapter (Zheng and Yu, 2014, 2015a,b).

4.2.1 governing equations

The granular material inside the CBM is treated as a continuum medium since the dimension of CBM is far larger than the diameter of particles. Similar to other forms of matter, granular dynamics also needs to satisfy the fundamental principles of mass, momentum and energy conservation, given by mass conservation

$$\frac{\partial \rho}{\partial t} + \nabla \cdot (\rho \boldsymbol{\nu}) = 0$$

Momentum conservation

$$\frac{(\rho \boldsymbol{\nu})}{\partial t} + \nabla \cdot (\rho \boldsymbol{\nu} \bigotimes \boldsymbol{\nu}) = \nabla \cdot \sigma + \rho \boldsymbol{b}$$

Energy conservation

$$\frac{(\rho\epsilon)}{\partial t} + \nabla \cdot (\epsilon \boldsymbol{\nu}) = \boldsymbol{\sigma} : \dot{\boldsymbol{\epsilon}}$$

where ρ refers to the bulk density of granular material, $\boldsymbol{\sigma}$ is Cauchy stress tensor, $\boldsymbol{b}$ is body force, $\boldsymbol{v}$ is velocity vector and ϵ is the internal energy per unit volume. $\dot{\boldsymbol{\epsilon}} = (1/2)(\nabla v + (\nabla v)^T)$represents the strain rate.

4.2.2 Mohr-Coulomb model

In the Mohr-Coulomb elastoplastic model, a linear relation between stress and elastic strain is adopted as:

$$\sigma_{ij} = D^{el}_{ijkl}\epsilon^{el}_{kl} \tag{4.1}$$

where σ_{ij} is the total stress; ϵ^{el}_{kl} is the elastic strain; and D^{el}_{ijkl} is the fourth-order tensor of elasticity.

The yield condition is given by:

$$R_{mc}q - p\tan\varphi - c_y = 0 \tag{4.2}$$

where

$$R_{mc} = \frac{1}{\sqrt{3}\cos\varphi}\sin(\Theta + \frac{\pi}{3}) + \frac{1}{3}\cos(\Theta + \frac{\pi}{3})\tan\varphi$$

φ is the slope of the Mohr-Coulomb yield surface in the $p - R_{mc}q$ stress plane, which is commonly referred to as the friction angle of the material and can depend on temperature and predefined field variables. $p = -\frac{1}{3}\text{trace}(\sigma_{ij})$ is the first invariant of stress representing the equivalent pressure; $q = \sqrt{\frac{3}{2}S_{ij}S_{ij}}$ is the Mises equivalent stress and S_{ij} is the deviatoric stress; φ and c_y are the angles of internal friction and the cohesion of granular material, respectively. Θ is the deviatoric polar angle defined as $\cos(3\Theta) = (r/q)^3$ where $r = (\frac{9}{2}S_{ji}S_{jk}S_{ki})^{\frac{1}{3}}$ is an invariant measure of deviatoric stress. The friction angle, φ, controls the shape of the yield surface in the deviatoric place. The friction angle range is $0° < \varphi < 90°$. In the case of $\varphi = 0°$ the Mohr-Coulomb model reduces to the pressure-independent Tresca model with a perfectly hexagonal deviatoric section. In the case of

$\varphi = 90°$ the Mohr-Coulomb model reduces to the "tension cutoff" Rankine model with a triangular deviatoric section and $R_{mc} = \infty$.

Granular flow can be well described as flow rules. The flow potential G is chosen to be a hyperbolic function in the meridional stress plane and a smooth elliptic function in the deviatoric stress plane, defined by:

$$G = \sqrt{(\epsilon c\mid_0 \tan\psi)^2 + (R_{mw}q)^2} - p\tan\psi \tag{4.3}$$

and

$$R_{mw} = \frac{4(1-e^2)\cos^2\Theta + (2e-1)^2}{2(1-e^2)\cos\Theta + (2e-1)\sqrt{4(1-e^2)\cos^2\Theta + 5e^2 - 4e}} \times \frac{3-\sin\varphi}{6\cos\varphi} \tag{4.4}$$

where ψ is the dilatancy angle of material, $c|_0$ is the initial cohesion yield stress, ϵ is a parameter that characterizes the eccentricity of the flow potential. e referred to as the deviatoric eccentricity, describing the "out-of-roundedness" of the deviatoric section in terms of the ratio between the shear stress along the extension meridian and the shear stress along the compression meridian, is a function of the internal friction angle φ, given as $e = (3 - \sin\varphi)/(3 + \sin\varphi)$.

An additive strain rate decomposition is assumed:

$$d\boldsymbol{\varepsilon} = d\boldsymbol{\varepsilon}^{el} + d\boldsymbol{\varepsilon}^{pl},$$

where $d\boldsymbol{\varepsilon}$ is the total strain rate, $d\boldsymbol{\varepsilon}^{el}$ is the elastic strain rate, and $d\boldsymbol{\varepsilon}^{pl}$ is the inelastic (plastic) strain rate.

The constitutive flow rule can be written as:

$$d\boldsymbol{\varepsilon} = \frac{d\boldsymbol{\varepsilon}}{g}\frac{\partial G}{\partial \boldsymbol{\sigma}},$$

where g can be written as

$$g = \frac{1}{c}\boldsymbol{\sigma} : \frac{\partial G}{\partial \boldsymbol{\sigma}}$$

4.2.3 Transient mixing model

The general scalar transport equation governing the mixing process (Khakhar, 2011) can be expressed in Eq.4.5, where c is the concentration (also known as volume fraction) of granular materials of one spices and v is its velocity. The left side refers to the terms for the traditional convection only and the right hand side indicates the term for diffusion mechanism.

$$\frac{\partial c}{\partial t} + v \cdot \nabla c = \nabla \cdot (\boldsymbol{D} \nabla c) \tag{4.5}$$

The notion $\mathbf{D}$ in front of the gradient operator refers to the diffusivity which can be treated as a tensor (Campell, 1997). In our work for simplicity, it is assumed as a scalar. In the dilute region (Fan et al., 2015), the relationship between diffusivity and particle diameter and granular temperatures can be expressed as:

$$D \sim d_p \sqrt{T} \tag{4.6}$$

where d_p is the particle diameter and T is the granular temperature. In the dense region of granular material (Hajra and Khakhar, 2005), the linear relationship can be represented as:

$$D = \chi \dot{\gamma} d_p^2 \tag{4.7}$$

where $\dot{\gamma}$ and χ are the local shear rate of material and diffusion coefficient respectively.

4.2.4 Boundary conditions

For the governing equations of Eulerian method, according to ABAQUS manual (Abaqus 6.10 Analysis User Manual (Dassault Systmes Simulia Corp, Providence, RI)), there are 3 types of boundary conditions for inflow materials: free inflow, no inflow and void inflow.

Free inflow

If no Eulerian boundary is defined, material can flow into the Eulerian domain freely; and the material content and the state of each inflow material are equal to that which presently exists within the element.

No inflow

Material or void can flow into the Eulerian domain through the specified boundary. The normal component of the velocity is set to zero if the velocity is directed inward at the boundary, while the tangential component of the velocity remains unchanged.

Void inflow

Inflow can occur but the influx volume contains only void.

There are also 4 types of boundary conditions for outflow materials: free outflow, nonreflecting outflow, equilibrium outflow and zero-pressure outflow.

Free outflow

Material can flow out of the Eulerian domain freely; and the material content and the state of each outflow material are equal to that which presently exists within the element.

Nonreflecting outflow

A nonreflecting outflow condition can be used in boundary value problems defined in unbounded domains or problems in which the region of interest is small in size compared to the surrounding medium.

Equilibrium outflow

It is assumed that the stress is zero-order continuous across the element faces on the boundary. Traction is applied to these element faces to balance the nodal forces created by the stress in the boundary elements. This condition is usually applied at the outflow boundary where the pressure distribution is unknown.

Zero-pressure outflow

It is common in flow problems to specify a zero pressure at the outlet of the flow. Since the normal traction on the boundary contains the contribution from both the pressure and the shear stress, the natural boundary condition is not sufficient to provide such a condition if the shear behavior of the flow is also considered. The zero pressure outflow condition applies a traction that counteracts the shear contribution and, thus, generates a uniformly distributed pressure field on the boundary.

In this chapter, the simulation happens in a 2D cylindrical mixer where materials are able to flow freely through the boundaries, so the boundary conditions of no-inflow and free outflow are applied in this work.
For the mixing process, the zero-flux boundary condition is adopted throughout the work as Eq.6.8 describes.

$$\nabla \cdot (\boldsymbol{D}\nabla \boldsymbol{c}) = 0 \tag{4.8}$$

4.2.5 Implementation of coupling diffusion to FEM

A splitting operator method (Karlsen et al., 2001; Lanser and Verwer, 1999; Fan et al., 2014) which decomposes a complex equation into two parts for obtaining numerical solutions is applied in this work. The concentration equation 4.5 can be split into the LHS part which indicates the convection mechanism and the RHS part representing the diffusion term during the mixing process. Finally, the whole concentration equation can be decomposed into a couple of differential equations:

$$\frac{\partial c}{\partial t} = -v \cdot \nabla c \quad \text{(convection quation)} \tag{4.9}$$
$$\frac{\partial c}{\partial t} = \nabla \cdot (\boldsymbol{D}\nabla c) \quad \text{(diffusion quation)} \tag{4.10}$$

The numerical solution of concentration $c_{i,j}^{t_c}$ of the LHS convection part (Eq.4.9) at each time step t and the node $(i,\ j)$ can be made by the FEM dynamics and obtained via ABAQUS. The RHS diffusion part (Eq.4.10) can be solved numerically by the Finite Central Difference Method (FCDM). A two dimensional case of FCDM regarding the second order derivative can be illustrated as the way of calculating algorithm bellow. The diffusion term in form of continuous space and time is smashed down into a set of discrete quantities located at the nodes of the FEM grid :

$$\left(\frac{\partial^2 c}{\partial x^2}\right)_{i,j} = \frac{c_{i+1,j} - 2c_{i,j} + c_{i-1,j}}{(\triangle x)^2} + O((\triangle x)^2) \tag{4.11}$$

, where $i,\ j$ are the node numbers of the mesh created by FEM and $\triangle x$ is the length of interval between two nodes as Fig.4.1 shows. $O((\triangle x)^2$ refers to infinitesimal of high orders. The diffusion part of $c_{i,j}^{t_c}$ can be obtained by Eq.4.10 and Eq.4.11:

$$c_{i,j}^{t_d} = D * dt * \frac{c_{i+1,j}^{t_c} - 2c_{i,j}^{t_c} + c_{i-1,j}^{t_c}}{(\triangle x)^2} \tag{4.12}$$

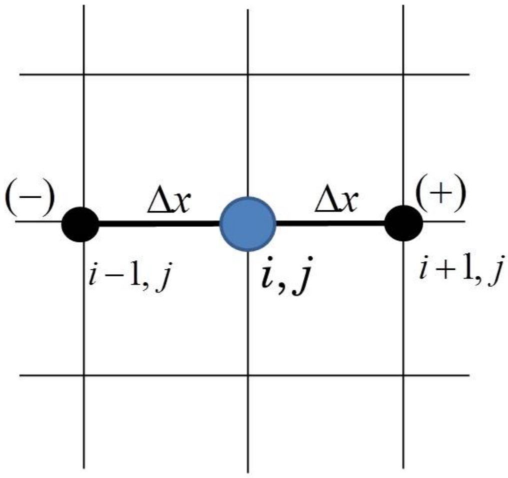

Figure 4.1: The integration grids in FEM mesh configuration.

As the flow chart (Fig.4.2) indicates, the whole FEM diffusion dynamics proceeds explicitly via the ABAQUS solver. To obtain the concentration of each node at time step t+1, the concentration $c_{i,j}^{t_c}$ at each time step t calculated by FEM convection dynamics continue to be updated through the following algorithm:

$$\begin{aligned} c_{i,j}^{t+1} &= c_{i,j}^{t_c} + c_{i,j}^{t_d} & (4.13)\\ &= c_{i,j}^{t_c} + D * dt * \frac{c_{i+1,j}^{t_c} - 2c_{i,j}^{t_c} + c_{i-1,j}^{t_c}}{(\triangle x)^2} & (4.14) \end{aligned}$$

, where $c_{i,j}^{t+1}$ refers to the species concentration at time step $t+1$. The updated $c_{i,j}^{t+1}$ will be involved in a new round of convection calculation through the ABAQUS solver. The coupling procedure is implemented via the user subroutine VUSDFLD.

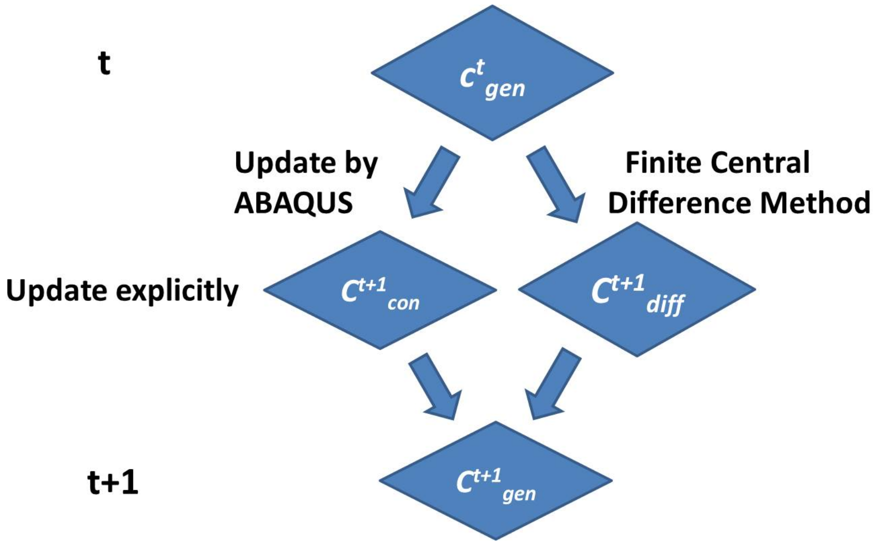

Figure 4.2: The algorithm of updating variables by FEM explicit solver.

4.2.6 Simulation conditions

Three dimensional (3D) thick drums and quasi-2D thin drums are the two typical commonly studied drums in many literatures (Zheng and Yu, 2015b; Santos et al., 2013; Khakhar, McCarthy, Shinbrot and Ottino, 1997). In a 3D drum, particle flow in the middle can be hardly influenced by the friction from walls at both ends of the drum, while the interaction with walls plays an important role in the flow processing in a 2D drum. However, in order to simplify the numerical simulation in this work, a quasi-2D thin drum with no end walls is adopted and modelled as Lagrangian parts (element type R3D4). The granular bulk is immobile along the axial direction, which is similar to the periodic boundary condition (BC) treatment. Granular material is described by the Mohr-coulomb elastic-plastic modelling and treated as a continuous Eulerian part (element type EC3D8R). To achieve the high accuracy, a high mesh density with mesh size of 0.5 cm (the optimized mesh size in (Bai et al., 2017)) is employed throughout the simulation. The geometry and mesh condition similar to the work (Zheng and Yu, 2015b) are shown in Fig.4.3 where these Lagrangian elements should be totally immersed into the Eulerian meshes to contact with granular materials. To visualize the boundary of material in an Eulerian field, an Eulerian Volume Fraction (EVF) is defined to determine the volume of material within Eulerian elements. More information of the Eulerian FEM technique can be found in (Zheng and Yu, 2014, 2015a,b). The parameters of the drum and the granular material are listed in

Table 4.1.

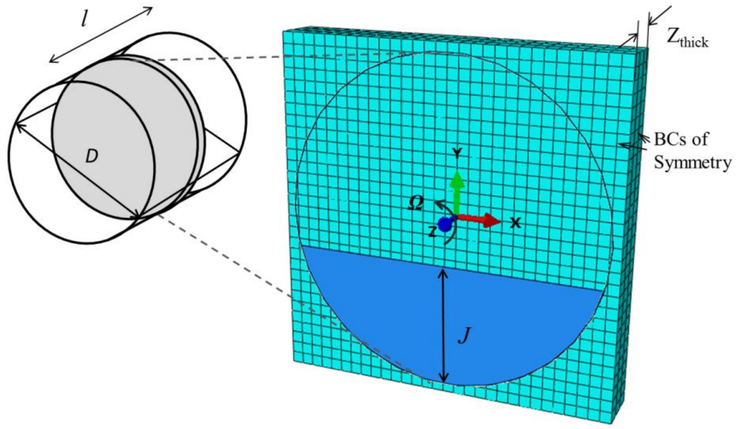

Figure 4.3: Drum geometry and mesh condition (Zheng and Yu, 2015b).

Parameters	Symbols	Values	Range of variation
Drum diameter	d	0.07 m	-
Drum thickness	Z	0.01 m	-
Drum rotation speed	ω	15 rpm	-
Particle diameter	d_p	1.3 mm	-
Particle density	ρ	1500 kg/m^3	-
Poisson's ratio	ν	0.3	-
Young's modulus	E	1×10^6 Pa	-
Internal friction angle	φ	20°	15° - 30°
Friction coefficient of material-wall interaction	μ	0.3	0.1 - 0.3
Cohesion yield stress	c_y	0 Pa	-
Diffusion coefficient	χ	0.1	0.01 - 0.5
Diffusivity	D	10^{-3}	10^{-4} - 10^{-3}

Table 4.1: Parameters used in the simulation

4.3 Results and discussion

4.3.1 FCDM Diffusion test with ABAQUS

The accuracy of diffusion algorithm is tested through 1D Gaussian pulse diffusion case. The 1D diffusion equation can be written as:

$$\frac{\partial c(x)}{\partial t} = D\frac{\partial^2 c(x)}{\partial x^2} \tag{4.15}$$

The diffusion equation above admits a Gaussian function as solution:

$$c(x,t) = \frac{1}{\sqrt{4\pi Dt}} \exp\left(-\frac{x^2}{4Dt}\right) \tag{4.16}$$

At $t = 0s$ this is a Dirac delta function, so for computational purposes one must start to view the solution at some time $t = t_\epsilon > 0$. Replacing t by $t_\epsilon + t$ makes it easy to operate with a (new) t that starts at t=0s with an initial condition with a finite width. The important feature of Eq.4.16 is that the standard deviation σ of a sharp initial Gaussian pulse increases in time according to $\sigma = \sqrt{2Dt}$, making the pulse diffuse and flatten out. We tested the numerical results generated by the Finite Central Difference Method above in comparison with the analytical equation Eq.4.16. The diffusion patterns of 1D and 2D are shown in Figs.4.4 and 4.5. At t=1.0s the value is concentrated in the center and spread symmetrically to both sides. As time increases, the value evolves due to diffusion effects and tends to be distributed uniformly in space. The quantitative results of $D = 10^{-3}m^2s^{-1}$ are shown in Fig.4.6. It can be seen that the two kinds of results also overlap which demonstrates the high accuracy of our method. As time increases, the central pulse becomes flat and will finally equals to zero when time goes to infinite. The time interval is selected as $\triangle t = 10^{-3}s$ much wider than the average time increment ($\triangle t = 10^{-5}s$) in FEM dynamics, which demonstrates our method is hardly dependant on time increment steps. Figs.4.7 and 4.8 show the cases of mesh size effects ($\triangle s = 0.02$ m and $\triangle s = 0.04$ m respectively). However, when the diffusion coefficient decreases to a lower value, the results are sensitive to the grid density. Fig.4.9 and 4.10 show the cases when the mesh size is above certain threshold, deviation to the analytical function can be observed. The courser mesh can only be applied when the diffusivity is large enough

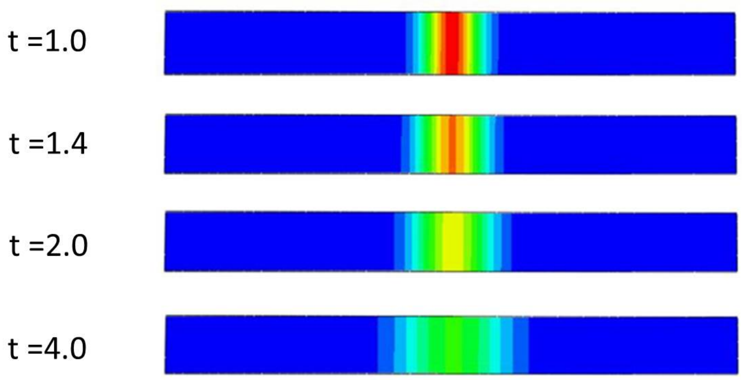

Figure 4.4: 1D diffusion pattern evolution.

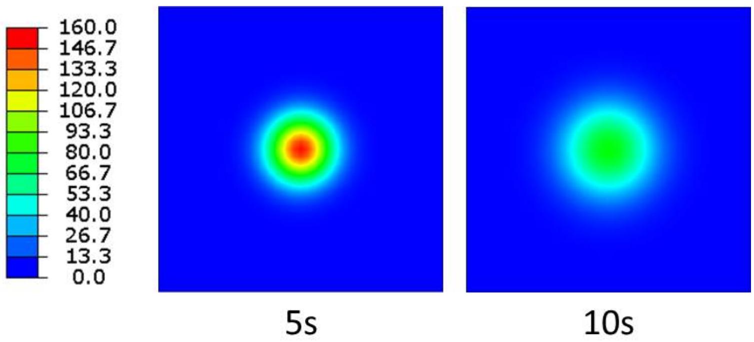

Figure 4.5: 2D diffusion pattern evolution.

for FCDM. The RHS of Eq.4.15 can be discretized by FCDM into Eq.4.17. The value of the discrete term on the RHS is the high order of intestinal related to $\triangle x$ so for most simulation cases, FCDM can rarely be affected by the mesh size.

$$\frac{c(x+\triangle x)+c(x-\triangle x)-2c(x)}{\triangle x^2}=c''(x)+\frac{1}{12}c^{(4)}\triangle x^2+O(\triangle x) \tag{4.17}$$

4.3.2 Model verification in 2D shear flow

Diffusion in sheared granular systems has attracted considerable attention in granular flow. In order to further validate the FEM diffusion model, the FEM simulation of quasi-two dimensional Couette shear flow is carried out. The original DEM simulation schematic is shown in Fig.4.11. White spheres are adhered and fixed at the bottom and top walls. The bottom wall is driven at a constant velocity along the x direction to apply shear to interior particles, while the upper wall is stationary. The boundaries of the x direction (streamwise direction) and z direction (vertical direction) are periodic such that particles

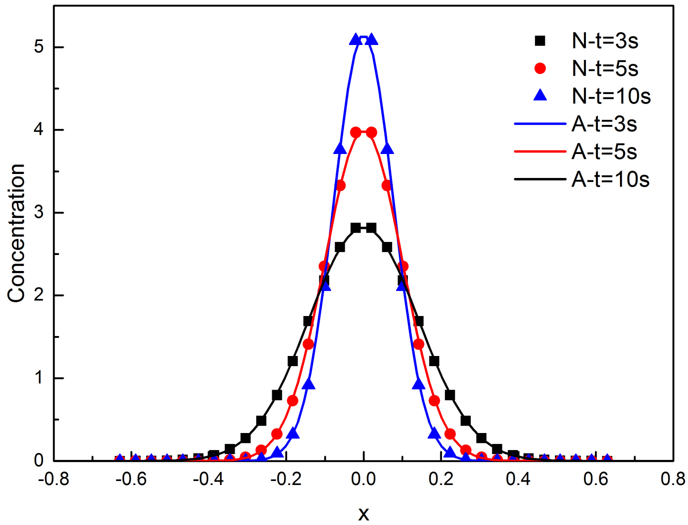

Figure 4.6: Comparison of results between numeration and analysis. N-t: numerical results, A-t: the analytical results, $\triangle t = 10^{-3}$ s, $D = 10^{-3}$ m^{2}s^{-1}.

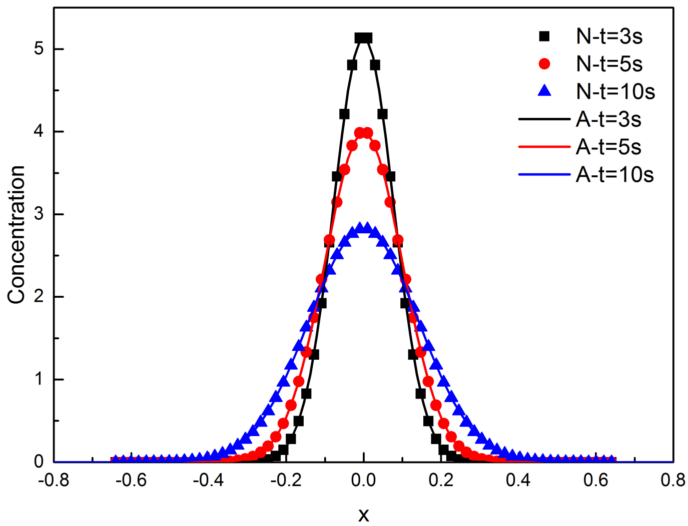

Figure 4.7: Comparison of results between numeration and analysis. N-t: numerical results, A-t: the analytical results, $\triangle s = 0.02$ m, $D = 10^{-3}$ m^{2}s^{-1}.

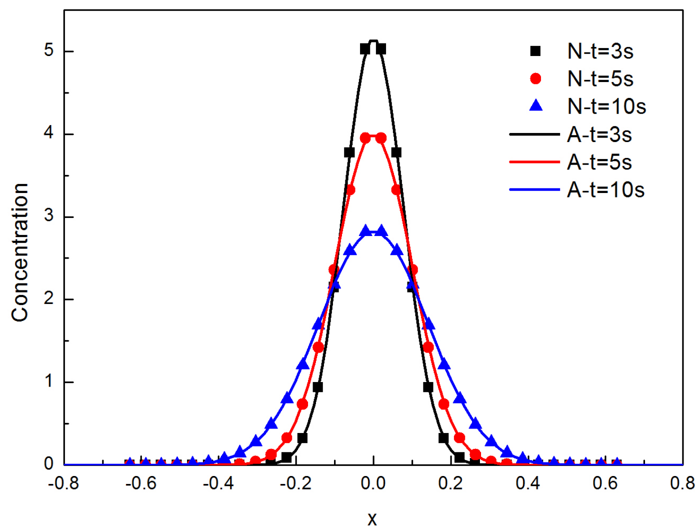

Figure 4.8: Comparison of results between numeration and analysis. N-t: numerical results, A-t: the analytical results, $\triangle s = 0.04$ m, $D = 10^{-3}$ m^{2}s^{-1}.

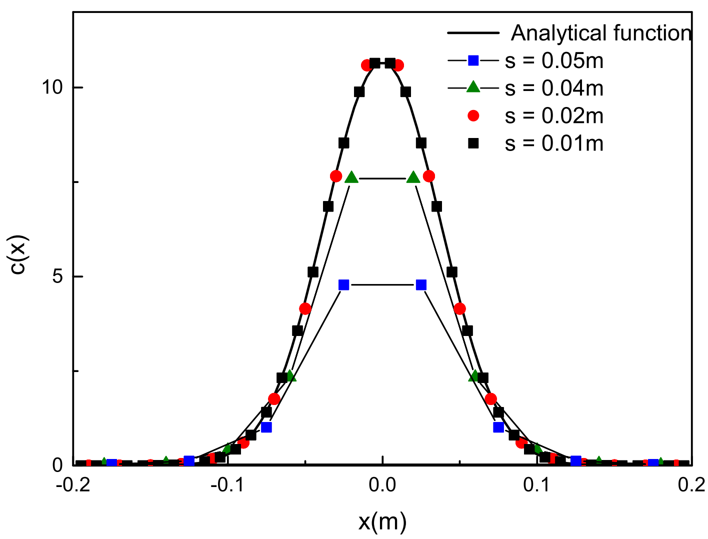

Figure 4.9: Influence of mesh size on simulation results. t = 7 s, $D = 10^{-4}$ m^{2}s^{-1}.

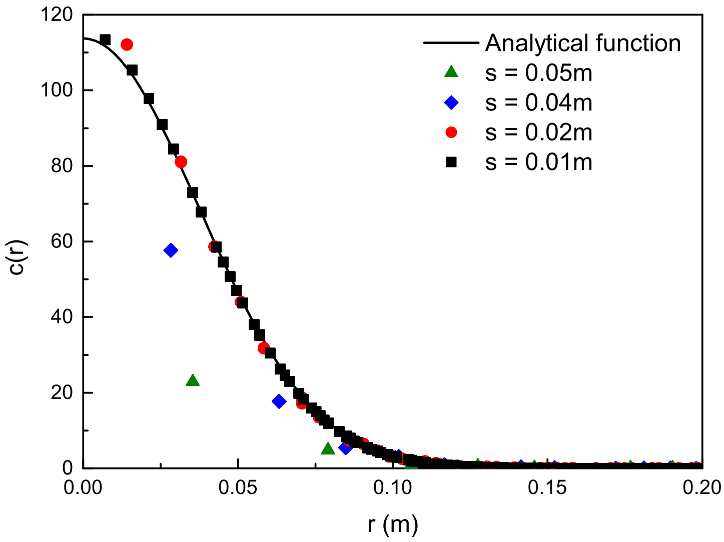

Figure 4.10: Mesh size effect on calculation accuracy. t = 7 s, $D = 10^{-4}$ m^{2}s^{-1}.

exit from one side and reappear on the other with the same altitudes and velocities. In FEM simulation, two very long thin rigid body are used as the fixed top and the bottom. The top is fixed while the bottom moves toward right at a constant speed. A very narrow range of Eulerian material in the middle from the whole entity is selected to eliminate the boundary effects. The interface between two materials of different colors becomes broadened because of diffusion caused by shear force, indicating the material penetration. The overall average velocities of DEM and FEM at different heights along x direction are compared in Fig.4.12. It is observed that at a lower speed ($\mu_0 = 0.66$ m/s) the results of velocity from FEM and DEM match well. However, at a higher speed ($\mu_0 = 1.55$ m/s) a large bifurcation is noted. A possible reason is that the constitutive law in our current model does not take nonlocal effects into consideration. Fig.4.13 shows the evolution and development of the FEM and DEM simulation mixing layer thicknesses. Both FEM and DEM show that the mixing layers expand with time and develop faster in the initial stages before growing smoothly. The mixing layers are almost symmetric. The panel velocity has a significant influence on the development of mixing layer. For those cases where larger bottom speeds are applied, the mixing layers end up in thicker blocks.

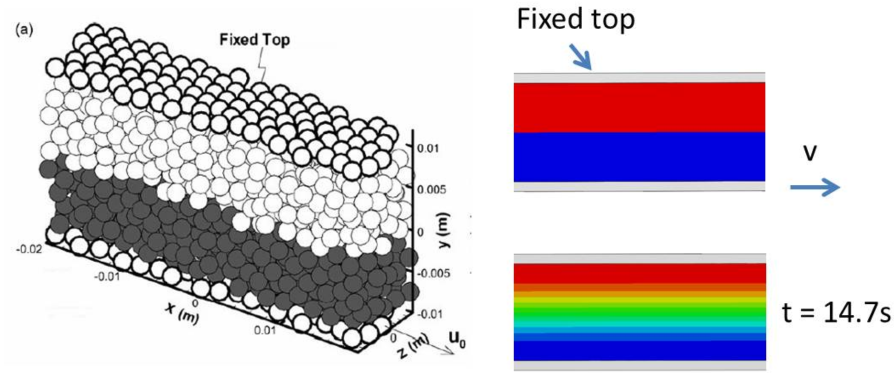

Figure 4.11: Schematic of the sheared granular flow. Left: Three-dimensional diagram (Lu and Hsiau, 2008); Right: FEM results.

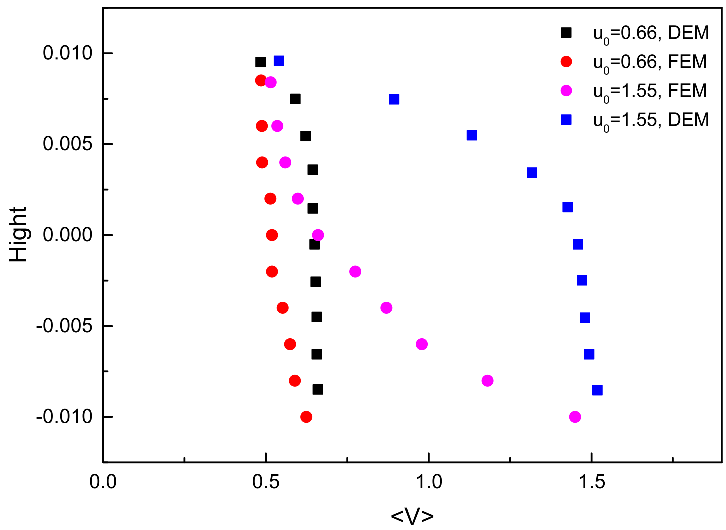

Figure 4.12: Distributions of overall average velocity in x direction. μ_0 indicates the moving speed at the bottom panel.

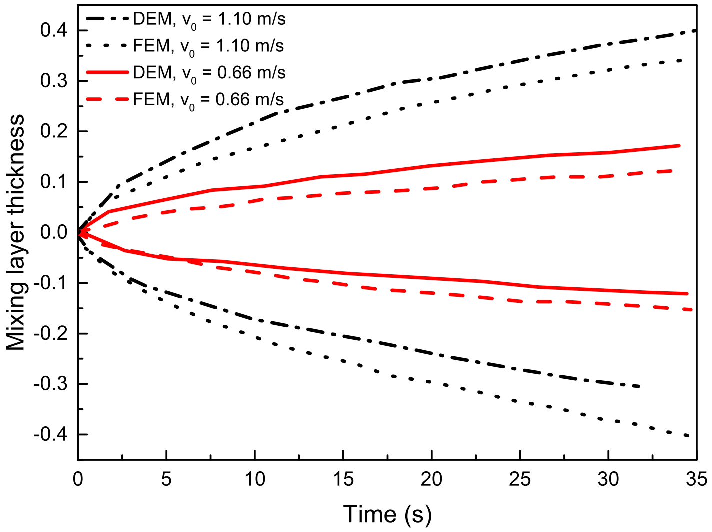

Figure 4.13: Evolution by FEM and DEM mixing layer thicknesses simulated.

4.3.3 Model verification in a 2D rotating drum

Diffusion occurs in the flowing layer (active region in Fig.4.14) if the FEM diffusion model is applied. Fig.4.14 shows the contour of shear rate $\dot{\gamma}$ where Eq.6.7 is applied. In the active region $\dot{\gamma}$ has an observable value while it can be negligible in the passive region. So that diffusivity can be almost zero in the passive region, which means diffusion mainly take effects in the active region especially in those areas where the value of $\dot{\gamma}$ is considerable. Fig.4.15 shows the comparison between the convection only case and the case when diffusion mechanism is added on. The case of convection only shows no mixing happening in all regions. For the diffusion case, the interface between two materials becomes more blurred and widened in the active region as materials penetrate to each other due to the existence of concentration gradient. Please note that the two mixing states in the passive region almost have the same mixing pattern because the diffusivity is almost zero in that regime and diffusion can be hardly observed. The FEM results with different diffusion coefficients are compared with DEM (Liu et al., 2013a). For FEM, all the geometrical and operational parameters are set up as same as DEM. As the value of χ increases, the contour of red material gets more unrecognized. It shows that when certain value (0.1 in our case) is chosen as the value of fitting parameter χ, the mixing pattern at some time step produced by FEM matches that of DEM. A quantitative comparison of mixing

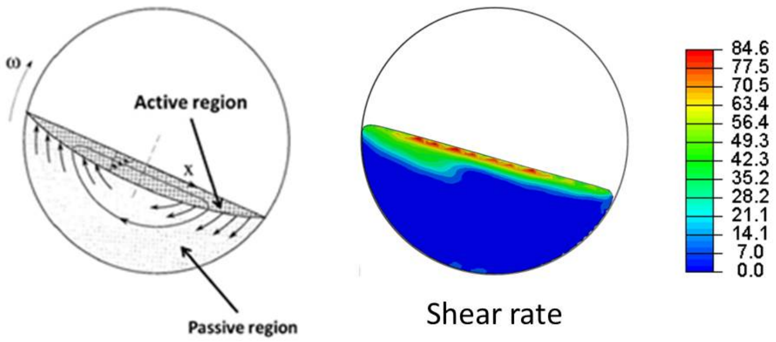

Figure 4.14: Evolution of the FEM and DEM mixing layer thicknesses.

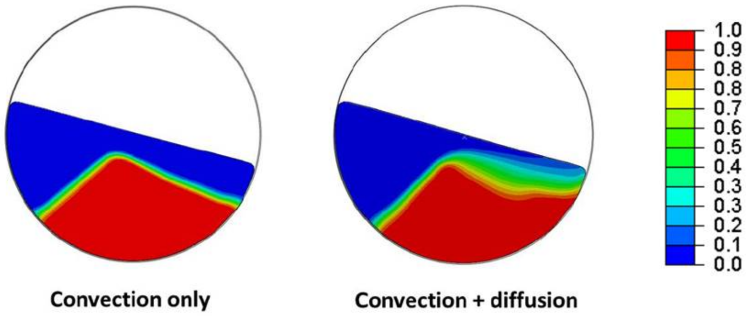

Figure 4.15: The roles of convection and diffusion in mixing. Left: mixing under convective motion. Right: mixing with convection and diffusion.

index (defined in Chapter 3) between FEM and DEM is shown in Fig.4.17. If χ is the fitting parameter, the mixing index of FEM is able to match that of DEM as illustrated in Fig.4.17 which shows the mixing index evolution as a function of revolutions. When χ varies from 0.05 to 0.5, the best fitting curve for the whole mixing process is $\chi = 0.5$. However, please note that at 1 rev the best fitting parameter χ is 0.1. That is why the most resemble pattern is $\chi = 0.1$ in Fig.4.16. The fitting method in the current diffusion model is quite different from that in the convection model discussed in Chapter 3, where the best way of matching the mixing index to DEM is implemented by changing the mesh size.

4.3.4 Mesh size effects

Many physical quantities produced by continuum methods are sensitive to Mesh sizes. In the study of mixing process, the mixing index can be more influenced. Generally, as the mesh size shrinks, the simulation result shows that the whole mixing process has a slower mixing rate and needs a long mixing period to complete. The reason why the mixing process is delayed has been analysed in Chapter 3. However, the mesh size effect should

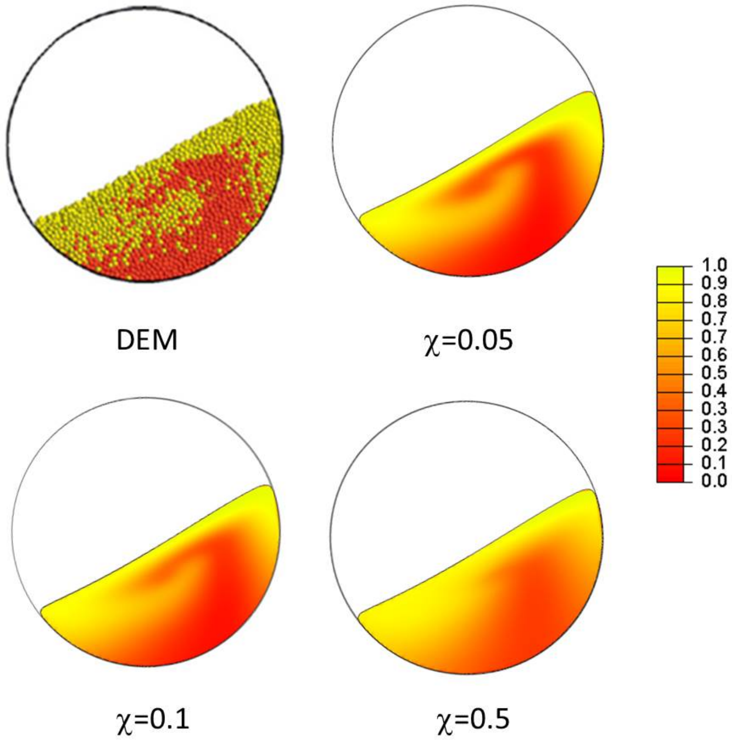

Figure 4.16: Comparison between DEM and FEM patterns with different diffusion coefficients at 1 rev. upper left: DEM results from (Liu et al., 2013a). Right: FEM mixing results with different values of χ.

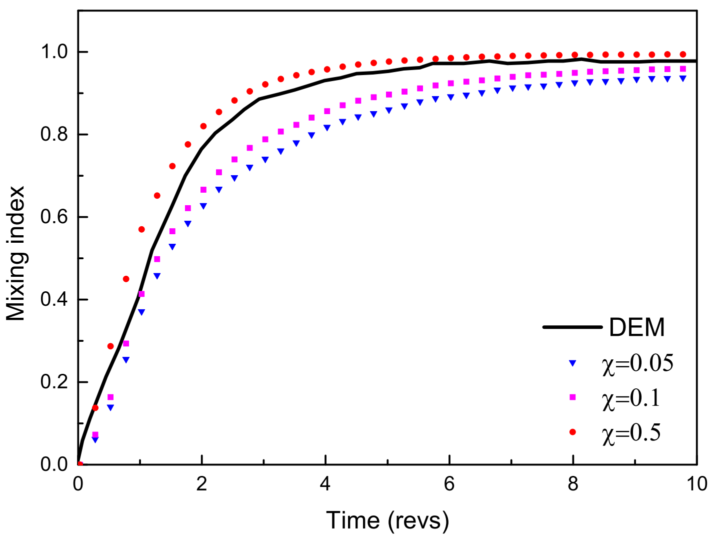

Figure 4.17: Comparison of mixing index between DEM and FEM. The parameters selected are the same used in DEM (Liu et al., 2013a) (f=40% and Ω = 15rpm)

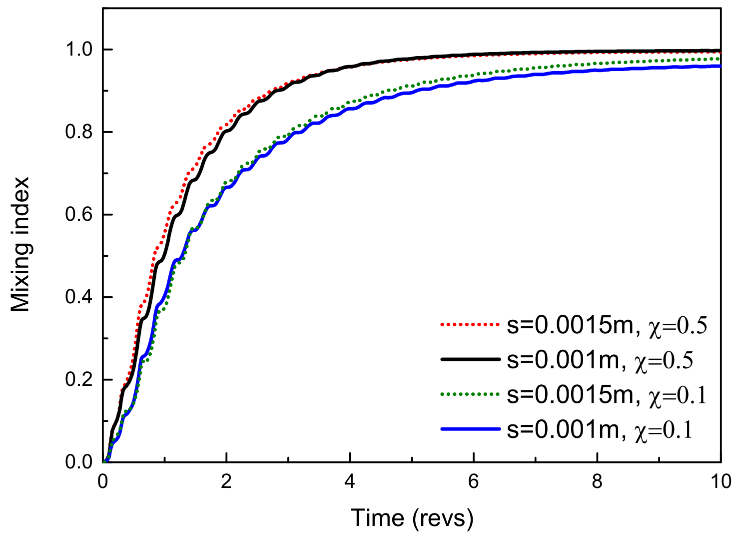

Figure 4.18: Mesh size effects on mixing index

be avoided and reasonably controlled by the model since improper mesh sizes may lead to inaccurate results. Fig.4.18 provides a possible way to reduce the mesh size effect by increasing the diffusion coefficient. As the diffusion coefficient increases from 0.1 to 0.5, the difference between the two indexes with the same χ but different mesh densities is narrowed. It can be inferred that when χ continues to increase, the mesh size effect wears off and can be finally neglected. Fig.4.18 further demonstrates that when the value of diffusion coefficient is above a threshold, the mixing index is independent of mesh size. In our case, when χ is 0.5, the gap between two mesh sizes (s = 0.001 m and s = 0.0015 m) can be negligible. However, when $\chi = 0.1$ the mixing index can still be affected by the mesh size. Our study indicates that when the mesh size is less than 1/3 L_d (diffusion length defined below), it is small enough to get a reliable mixing index independent of mesh sizes. The diffusion length can be defined as below:

$$L_d = \sqrt{D_{mid} \frac{L}{v_{mid}}}, \tag{4.18}$$

where L is the surface length of materials in the active region. D_{mid} and v_{mid} refer to the diffusivity and velocity at the middle point of L respectively.

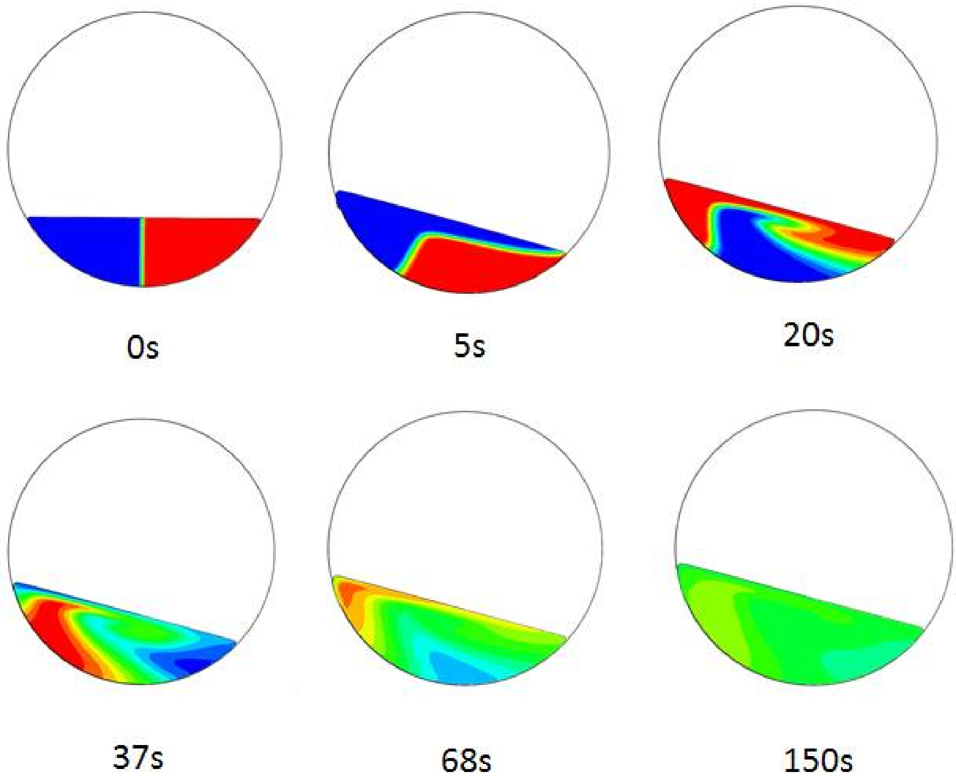

Figure 4.19: Mixing pattern evolution.

4.3.5 Mixing patterns at different filling levels

Fig.4.19 shows the mixing patterns at different stages with a lower filling level of 25%. The materials with different colours are separated at t = 0 s. Shortly after the drum starts rotating, the interface (in green) bends, curves and distorts. The stretching and expanding of interface indicates the commencement of particle mixing. As the rotation continues, the green region grows gradually because of the diffusion effect and eventually expands to the whole assumably at t = 150 s, suggesting that the system has reached an overall homogeneous mixing state. Fig.4.20 shows the pattern formation with the filling level more than one half (3/4 in our case). A final core forms in the center if the drum rotates slowly (0.05 rad/s in our case) and the material moves in an avalanche way. The pattern can be generated by different simulation methods, one of which is the famous geometrical approach by which blocks of material are transferred in the way of wedges movement (Metcalfe et al., 1995b) (shown in the lower side in Fig.4.20). FEM is also able to easily reproduce the pattern as shown in the upper side in Fig.4.20. Our results are more realistic in comparison with experiments, since FEM shows the margin that the

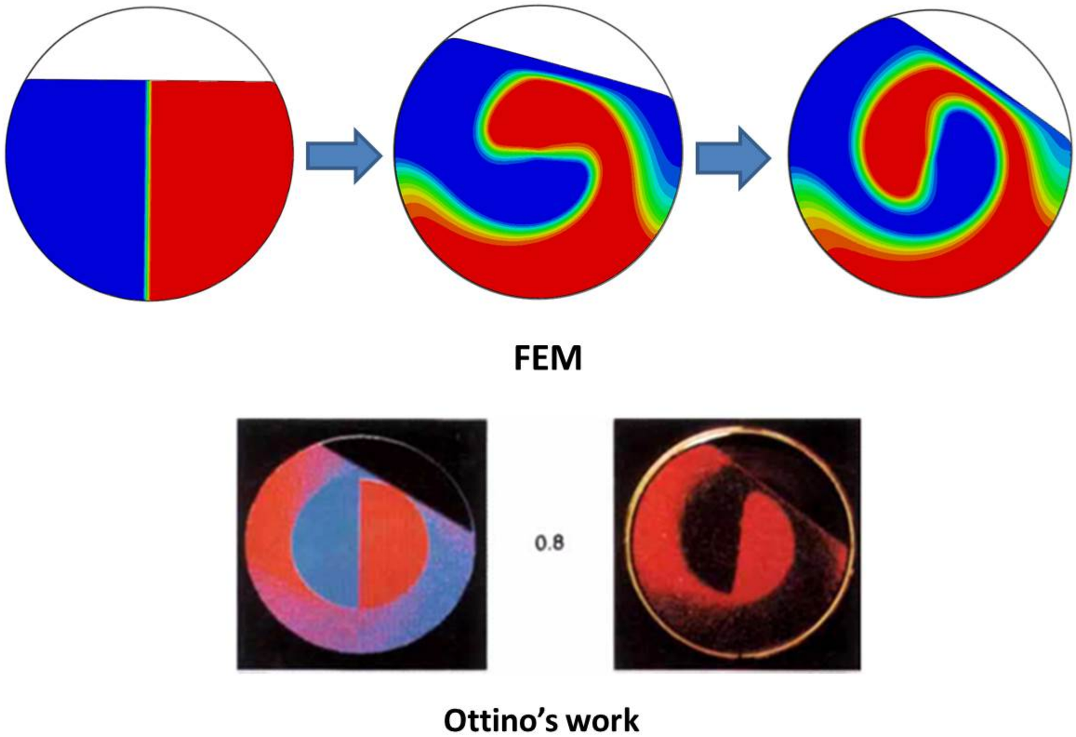

Figure 4.20: Pattern formation in the case of avalanche.

geometrical method failed to produce between the red material and the surface (lower left side in Fig.4.20).

Chaotic mixing

In fluid mixing, the interfacial area between different fluids is a commonly studied fundamental quantity which reflects how the fluid stretch and fold during the mixing process (Ottino, 1990; Christov et al., 2011; Khakhar et al., 1999). The interfacial area per unit volume of the layers is given by (Ottino, 1990; Christov et al., 2011; Khakhar et al., 1999) $a_v(x,t) = lim_{V\to 0}\frac{S}{V}$, where S is the interfacial area between fluid layers within the volume V enclosing point x at time t. For the total system, $a_v = \int a_v(x,t)dx$ and is independent of space. By definition, a larger a_v represents a better mixing. Technically in our modelling, we take the interfacial area as the number of nodes that have c_r values within the range $0.49 < c_r < 0.51$, N_{inter}. As shown in Fig.4.21, N_{inter} increases linearly with time in a circular drum. In contrast, in the case of an ellipse drum, N_{inter} increases more rapidly as an exponential function of time (Fig.4.22). It is the sign of chaotic mixing reported in (Khakhar et al., 1999) when $a_v(x,t)$ grows in an exponential way. Although the definition

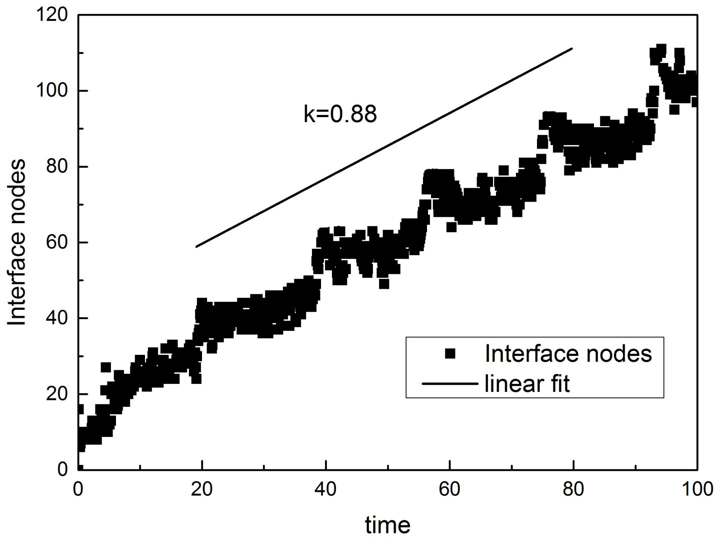

Figure 4.21: Interface nodes in a circular drum.

of N_{inter} in our method is slightly different to $a_v(x,t)$, N_{inter} can be regarded as a way of describing the chaotic mixing in a convective motion. In addition, N_{inter} is a more general quantity which can be applied in a complicated geometry such as a bladed mixer in chapter 3.

4.3.6 The diffusion effect on mixing with different parameters

The question that how diffusion influences the mixing process has intrigued many researchers. Some scholars assert that when the container diameter is much larger than the particle diameter, the influence of diffusion is not as important as a smaller mixer (Khakhar, McCarthy, Shinbrot and Ottino, 1997). As the Fig.4.17 shows, when the diffusion coefficient increases the mixing index will have a higher rate, which means when the granular diffusion is enhanced, the whole system can reach the homogenous state more quickly. The mixing index as a function of time should have the following form:

$$M = M_0 + N_0 e^{-kt} \tag{4.19}$$

where k (s^{-1}) is the mixing rate. Fig.4.23 - Fig.4.24 show the development of mixing index and the mixing rate with different diffusion coefficients for different filling levels and internal friction angles. The mixing index for Lower filling levels (20%) reaches the

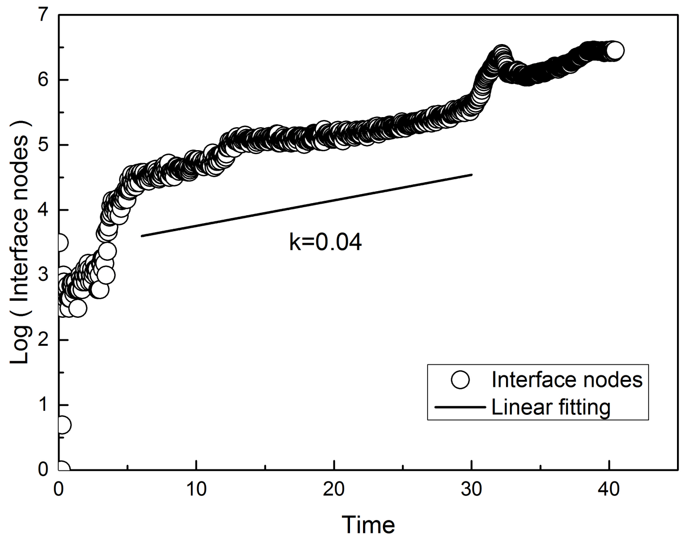

Figure 4.22: Interface nodes in an ellipse drum.

final mixed state more quickly than the other two higher filling levels (30% and 40%). It demonstrates lower filling levels result in a higher mixing rate, which can be verified in the lower part of Fig.4.23. At lower filling levels, materials have a lower surface angle and can be easily stretched, twisted, and folded, so that particles get mixed mainly by convection. For lower diffusion coefficients ($\chi = 0.05$, 0.1), the slopes of mixing rate drop as a function of filling level are almost the same. For a higher diffusion coefficient ($\chi = 0.5$), the drop has a steeper slope, which indicates diffusion helps to enhance the effect of filling level on the mixing process. It further indicates convection and diffusion are positive-correlated in this case. Fig.4.24 indicates small internal friction angles lead to a higher mixing rate. As previously analysed in Chapter 3, materials with a small internal friction angle have a good quality of fluid, which makes the granular bulk flow more flexibly. In such case, the enhanced convection can easily transfers particles to different locations where particles with different properties can be met with a high possibility. The slope of mixing rate as a function of internal friction angles is larger for the range from $\varphi = 10°$ to $\varphi = 20°$ than from $\varphi = 20°$ to $\varphi = 30°$. This phenomenon is more evident when χ increases to 0.5. This demonstrates that the effect of convection can be enhanced by diffusion especially when convection plays a dominant role in the mixing process. The two cases illustrate the two mechanisms (convection and diffusion) are interrelated. However, understanding the interaction of the them is complex and complicated and need more analyses and explanations in the future study.

4.3.7 Axial diffusion in a long cylindrical drum

It is indicated that the axial mixing of granular materials is a self-diffusive process driven by frequent collisions between particles. So it is interesting to find if the FEM diffusion model can be extended and applied to the axial mixing in a 3D case. For axial diffusion along Z axis, the diffusion equation can be described

$$\frac{\partial c}{\partial t} = D\frac{\partial^2 c}{\partial z^2} \tag{4.20}$$

Fig.4.25 plots the mixing band pattern along Z axis at two different time steps by the FEM diffusion model with the governing equation 4.20. For the binary mixing, materials with same properties but different colors are set at both sides along the Z axis at the beginning. The parameters in the 3D drum simulation are listed in Table 4.20. As the drum rotates, the band in green grows widely and the interface between two types of materials becomes blurred due to the particle penetration caused by diffusion. The average concentration c(z) along the Z axis as a function of time is compared with that of DEM. Fig.4.26 shows that with a proper diffusion coefficient ($\chi = 2 \times 10^{-2}$ in our case), the FEM results from the diffusion model basically agree with the DEM results obeying Fick's law

$$c(z,t) = \frac{1}{2}\left[1 + \mathrm{erf}\left(\frac{z}{2\sqrt{Dt}}\right)\right] \tag{4.21}$$

where D is the diffusivity and $\mathrm{erf}(x) = 2/\sqrt{\pi}\int_0^x e^{-x^2}dx$ is the error function. As the mixing process continues, the transition zone between two materials changes from a sharply narrow band with a high concentration gradient to a smoother widely material-mixed area. It indicates that the homogeneous mixing state can also be achieved via the self-diffusion mechanism. Please note that the axial diffusion coefficient is much smaller than the radial diffusion coefficient. This is because the axial diffusion is mainly driven by particles' collisions without external pressures or the effect of gravity. The investigation of material diffusivity is very important in order to understand the particle mixing performance. Previous DEM study shows the diffusivity increases with the rotation speed Ω, while increasing the drum filling level can reduce the particle diffusivity. To calculate the material

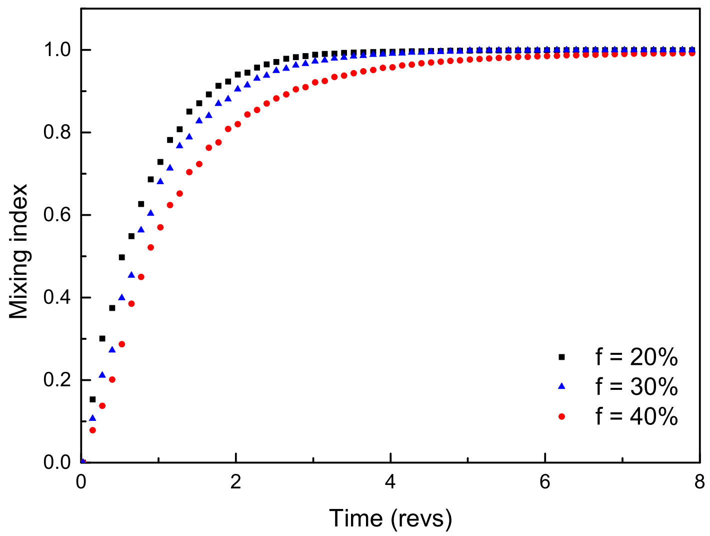

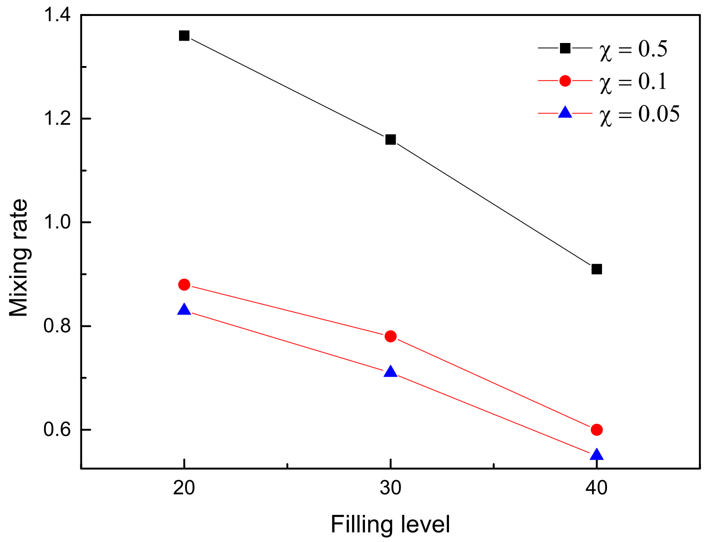

Figure 4.23: Mixing index and rate development under different filling levels with $\omega = 15$ rpm, $\varphi = 20°$.

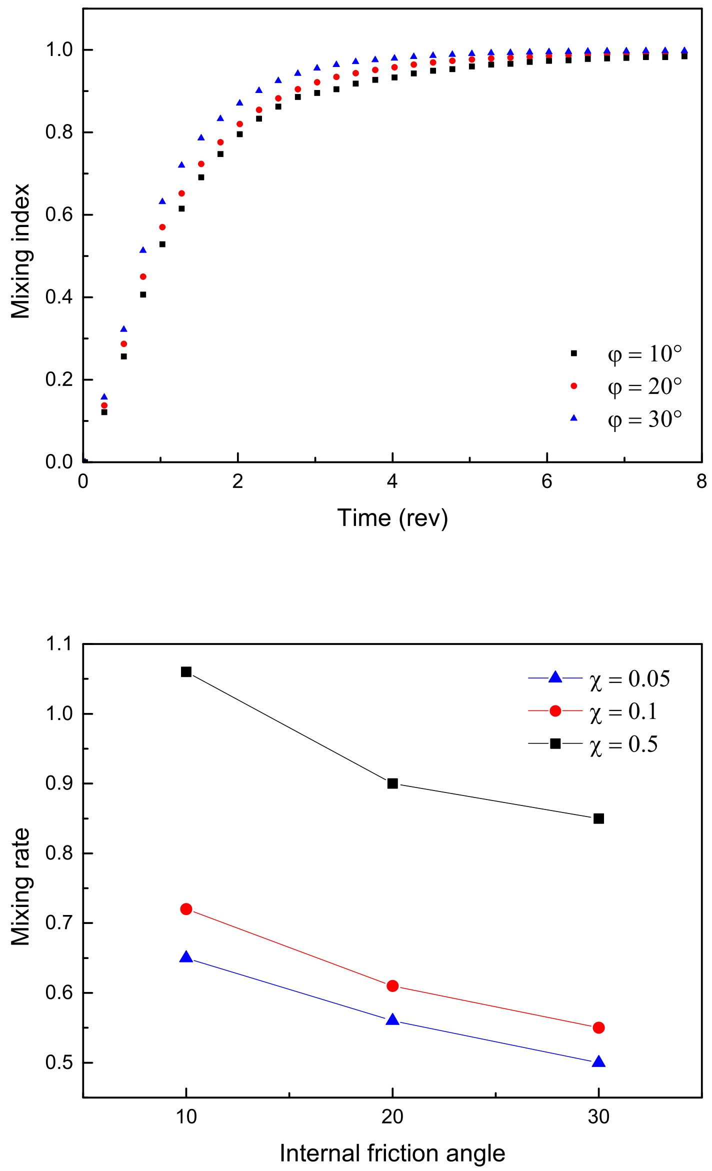

Figure 4.24: Mixing index and rate development under different internal friction angles with $\omega = 15$ rpm, $f = 40\%$.

Parameters	Symbols	Values	Range of variation
Drum diameter	d	0.07 m	-
Drum length	Z	0.078 m	-
Particle diameter	d_p	0.001 m	-
Filling level	f	35%	35% - 89%

Table 4.2: Physical parameters used in the simulation

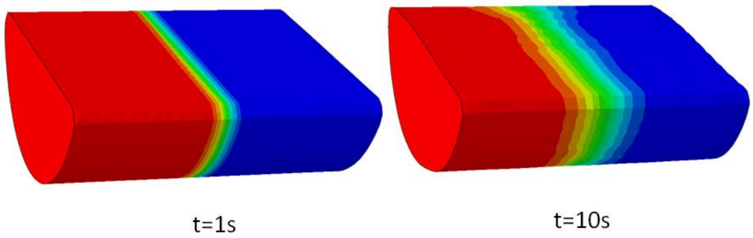

Figure 4.25: A lateral view of mixing patterns along the drum axis at different time. The materials are different in colour only (blue and red but have the same physical properties), f = 43%, $\Omega = 15$ rpm.

diffusivity, the formula

$$D = \bar{D}_F \frac{V_F}{V} \tag{4.22}$$

is adopted in the FEM diffusion model. $\bar{D}_F$ is the mean diffusivity of flow layer which is proportional to the particle size and mean shear rate $\bar{\dot{\gamma}}$. V_F and V are the volumes of the flowing layer and the entire bed respectively. Fig.4.27 and 4.28 show the changing of diffusivity when the rotation speed and filling levels vary. Both results show the trend of diffusivity development which agrees well with DEM. Lager rotation speeds cause a higher shear rate in the flowing regime which results in a larger value of diffusivity in that region. Higher filling levels lead to a smaller fraction of rapid flow layer (volume of rapid flow layer divided by total bed volume in Eq.4.22). The diffusivity in Eq.4.22 is therefore reduced. One the other hand, in Sec.4.3.6, it is analysed that materials with lowering filling levels are sensitive to the diffusivity coefficient in the 2D case. It can be predicted that the diffusion effect is also strengthened at lower filling levels in the 3D case, which brings about a larger value of particle diffusivity in Fig.4.28.

4.3.8 Conclusion

In this chapter, a general 3D FEM convection-diffusion mixing model is developed based on the operator splitting method. The diffusion term $D\nabla^2 c$ is coupled to the FEM convection

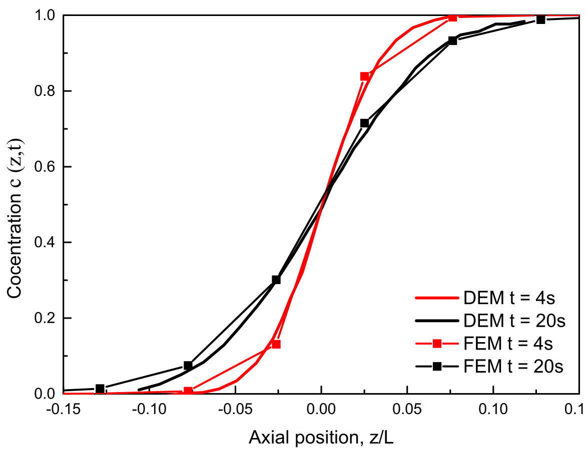

Figure 4.26: Concentration of red particles in the axial direction, f = 43%, Ω = 15 rpm, $\chi = 2 \times 10^{-3}$.

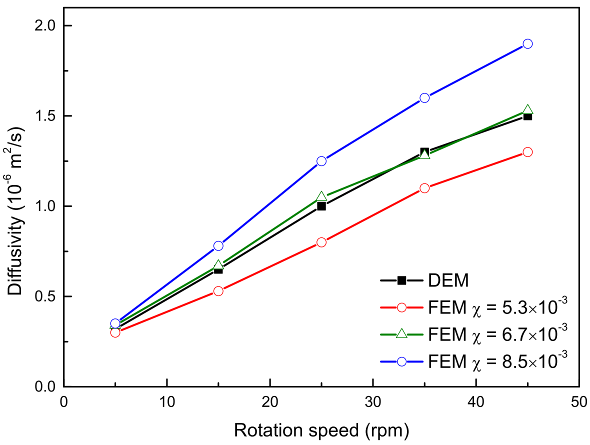

Figure 4.27: Variations of diffusivity with different rotation speeds at f = 43%.

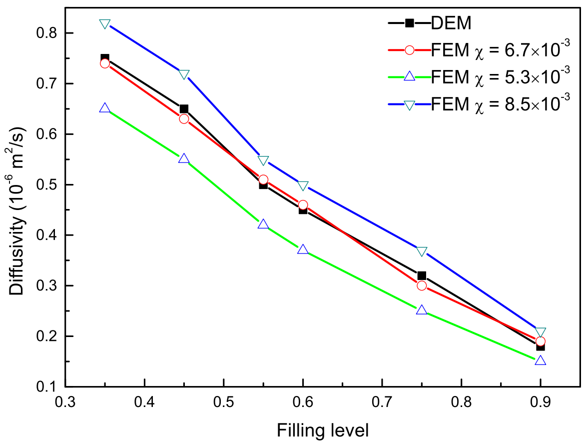

Figure 4.28: Variations of diffusivity with different filling levels at $\Omega = 15$ rpm.

model by the finite central difference method. The model is validated through 1D Gaussian pulse diffusion and 2D shear flow. The quasi 2D rotating drum in rolling regime is studied. The relationship $D = \chi\dot{\gamma}d^2$ is applied in order to determine the areas where diffusion occurs, which is consistent with the fact that mixing always happens in the flowing regime. Although this FEM mixing model is strictly tested and verified well in a quasi 2D rotating drum, it can be extended to the 3D case and applied in a more complicated granulator in the future mixing study. The FEM mixing patterns and indexes are compared with that from DEM. The influence of operational properties and material properties to diffusion mixing is studied. The following conclusions can be drawn from this study:

- The dynamics of explicit diffusion algorism is verified through 1D and 2D Gaussian pulse diffusion case and the numerical outcomes compare well with the analytical results. The dynamics of FEM diffusion can be independent of time steps and mesh sizes when the mesh size is below certain threshold value.

- In 2D drum study, diffusion take effects in the regime where the shear rate is nonzero because of the relation of diffusivity $D = \chi\dot{\gamma}d^2$ applied. $D = \chi\dot{\gamma}d^2$ is a good approximate criteria to determine passive regions and active regions in a granulator.

- The interface between two materials becomes more blurred when the diffusion algorithm is applied. The mixing index can be comparable to that from DEM when a proper fitting value of χ is chosen. The 2D FEM mixing model is independent of mesh sizes when the mesh size is less than $1/3L_d$.

- Diffusion has a positive influence on the effects of filling levels and internal friction angles on the mixing process. However, more studies and explanations are needed to understand the mechanism on diffusion dependency in the future study.

- The 2D FEM mixing model can be extended and used to study the 3D axial mixing process. The axial diffusivity is much smaller than the radial diffusivity which is confirmed by comparing results with DEM. Because the shear rate along the axial direction is almost negligible, diffusion takes more time to make the whole mixing complete than the radial mixing process. It is predicted that the general 3D FEM convection-diffusion mixing model can be used to study more complicated mixing processes in industries.

4.4 Nomenclature

ϱ bulk density of granular material [kg/m^3]

E Young's modulus [Pa]

ν Poisson's ratio [-]

φ internal friction angle [degree]

c_y shear cohesion [Pa]

c volume fraction [-]

μ Coulomb friction between granular material and drum wall [-]

μ_s sliding friction coefficient in DEM simulation [-]

N_{inter} interfacial area in form of number of nodes [-]

M mixing index [-]

σ standard deviation of concentration [-]

D diffusivity

$\dot{\gamma}$ shear rate

d_p diameter of particles

χ diffusivity coefficient

s mesh size

f filling level

Chapter 5

FEM Modelling of the size segregation of granular materials in a rotating cylinder

5.1 Introduction

Segregation of granular materials is ubiquitous and unquestionably important to many industries including chemical and pharmaceutical processes. It usually happens under external agitations when particles have different material properties such as size, density, shape or even surface roughness. Within a wide range of different conditions, size segregation is the most common and intriguing phenomenon. The famous example is "Brazil nut" effect (Williams, 1963; Rosato et al., 1987) whereby large particles of mixed nuts rise to the top in a shaken container. When particles are filled into silos or hopers by heap flow, stratified or segregated layers can be formed depending on different particle properties (Ketterhagen et al., 2007, 2008). In a rotating cylinder, the radial segregation (Cantelaube and Bideau, 1995; Dury and Ristow, 1997; Chakraborty et al., 2000; Khakhar, McCarthy and Ottino, 1997) and axial banding pattern (Hill et al., 1997; Nakagawa, 1994; Aranson et al., 1999; Gupta et al., 1991; Kuo et al., 2005) in the rolling regime have attracted substantial interest. The radial segregation states that smaller particles particles migrate towards the core of the cylinder. The axial segregation is more complex. Experiments show that the granular materials of different-sized particles segregate into bands when the speed of rotating cylinder is large enough, whereas the two materials may remix at a lower rotating speed. Hill and Kakalios (Hill et al., 1997) reported that axial segregation is strongly related to the difference of in the dynamic angles of repose between the mixed and segregated phase and it is initiated with large particles rich at the endwalls. However, those segregation phenomena are imperfectly understood and studies on continuum theory are limited. Many studies are devoted to understanding the underlying mechanism and developing predictive frameworks for size segregation and pattern formation in sheared granular flow (Fan et al., 2017). Those studies revealed basic assumed mechanism of segregation. In the dilute flow regime characterized by frequent particle binary collisions, the granular temperature gradient based on kinetic theory is able to model size segregation. In the dense flow regime, the percolation theory characterized by the percolation velocity suggests that small particles can squeeze into small voids below large particles in the flowing layer. As a result, smaller particles sink to the inner streamlines and the core of smaller particles forms after many revolutions. A mixture model extending kinetic theory in dense regime is proposed by (Gray and Thornton, 2005; Gray and Chugunov, 2006), in which two kinds of particle flows (large and small particles) interacting with each other are described by a coupled governing equations, but it still obtained qualitative agreement with discrete element method (DEM) simulations. Recently an advection-diffusion-percolation model has been proposed on a broad theoretical framework (Fan et al., 2014). The model is used to describe a wide range of segregation in several dense sheared flows including plug flow (Gray and Thornton, 2005), simple shear flow (Gray and Chugunov, 2006) and annular shear flow (Johanson et al., 2005).

The axial segregation in a long horizontal rotating cylindrical tumbler has attracted substantial attention in recent decades. Due to the complexity of the phenomenon, the fundamental onset mechanism of axial segregation is still unclear and the theoretical progress is limited. In mathematical physics, A modified phenomenological Cahn-Hilliard (CH) equation based on spinodal decomposition theory describing was postulated by Das and Puri (Das and Puri, 2003) to describe a long term cluster evolution in granular gases and was consistent with the observed morphology of clusters. In the 2D case of mixtures subject to horizontal oscillations, the CH equation was used to reproduce the stripe pattern and predicted analytically (Ciamarra et al., 2006). The travelling wave bands were successfully reproduced with a one-variable 1D CH equation coupled with convection (Inagaki and Yoshikawa, 2010). The coupling of the phase separation of the CH equation to certain fluid flow convection equation such as Navier-Stokes equation is a big interest to researchers at present (Vignal et al., 2015). The concept of "negative diffusivity" resulting from different dynamic repose angles is introduced to a diffusion equation to create a counter diffusion along the axial flow (Zik et al., 1994). But both the "spinodal decomposition" and the "negative diffusivity" may not be the right physical mechanism of band formation. Another onset mechanism based on the non-uniform distribution of axial velocity and unbalanced distribution of axial flow was proposed to demonstrate the percolation along with curved flow fields is the only physical segregation mechanism that leads to band formation along the axial direction (Chen et al., 2010, 2011).

In this work, we develop a FEM convection-diffusion-segregation model which is able to describe size segregation in granular physics. This chapter is organized as follows. Section 5.2 introduces the continuum theory of segregation including both percolation and spinodal decomposition. Section 5.3 discusses the Mohr-Coulomb elastoplastic theory and geometries and parameters used in the Eulerian FEM simulation. In section 5.4, the algorithm based on splitting operator method is discussed to couple segregation equations to dynamic FEM convection equations. In section 6.3, the results of radial segregation and axial segregation derived from percolation and CH model are discussed and compared with that from DEM. In the percolation model, the effects of percolation length and diffusion coefficient on the segregation process are studied, while as for the CH model, b_{seg} and ζ are also investigated to determine the segregation rate and degree. Finally, summaries and conclusions are presented in section 6.4.

5.2 Continuum theory of segregation

5.2.1 Percolation theory

In a binary mixture of different-sized particles, c_i denotes the volume fraction of species i ($i = l$ for large particles and $i = s$ for small particles). It can be defined as $c_i = f_i/f$ where f_i is the solids volume fraction of species i and $f = \sum f_i$. The continuum transport equation for the volume concentration of species i can be described as :

$$\frac{\partial c_i}{\partial t} + v_i \cdot \nabla c_i = \nabla \cdot \boldsymbol{D} \nabla c_i \tag{5.1}$$

where v_i is the velocity of species i and $\mathbf{D}$ is the diffusivity caused by collisions between particles. For simplicity, it is assumed that $\mathbf{D}$ is isotropic here and satisfy the relation:

$$D = \chi \dot{\gamma} d_p^2, \tag{5.2}$$

where $\dot{\gamma}$ is the shear rate and d_p is the particle diameter. In the percolation theory (Fan et al., 2014; Schlick et al., 2015), small particles driven by gravity are more likely to fall through voids between particles, which generates a percolation velocity vertical to streamlines. The percolation velocity depends on the particle size ratio, the strain rate, and the normal stress. In the cylinder case, it can be approximated as (Fan et al., 2014; Schlick et al., 2015):

$$\begin{aligned} w_l &= l_{seg} \dot{\gamma} (1 - c_l) \\ w_s &= -l_{seg} \dot{\gamma} (1 - c_s), \end{aligned}$$

where l_{seg} in the units of length is the percolation length depending both on the particle size ratio and particle sizes. It can be represented as:

$$l_{seg} = 0.26 d_s \log \left(\frac{d_l}{d_s} \right), \tag{5.3}$$

where d_l, d_s represent the size of large particles and small particles respectively. The whole transport equation taking into account convection, diffusion and percolation can be written as:

$$\frac{\partial c_i}{\partial t} + v_i \cdot \nabla c_i + \frac{\partial}{\partial z} (w_{p,i} c_i) = \nabla \cdot \boldsymbol{D} \nabla c_i \tag{5.4}$$

where z is the direction of gravity in the cylinder geometry.

5.2.2 The Cahn Hilliard equation

The Cahn-Hilliard (CH) equation phenomenologically describes the process of phase separation in mathematical physics. It originates from Ginzburg-Landau free energy:

$$\begin{aligned} F[\phi] &= \int_{\Omega_T} \Psi(\phi) f(\phi, \nabla \phi) d\Omega_T \\ &= \int_{\Omega_T} \Psi(\phi) + \frac{\zeta}{2} |\nabla \phi|^2 d\Omega_T \end{aligned}$$

where $\Omega_T \in R^d (d = 2, 3)$ is the domain which contains the binary mixture. ϕ is the phase field which effectively represents the concentration of one of the components present in the system. $\Psi(\phi) = 1/(2\theta)(\phi \log\phi + (1-\phi)\log(1-\phi)) + \phi(1-\phi)$ is the bulk free energy density that includes entropic effects. $\frac{\zeta}{2}|\nabla\phi|^2$ is the internal energy contribution to the free energy which is used to model interfacial effects. The parameter ζ is a positive constant related to the interface thickness. Euler-Lagrange equation gives that:

$$\frac{\delta F}{\delta \phi} = \frac{\delta f}{\delta \phi} - \nabla \cdot \frac{\delta f}{\delta \nabla \phi}, \tag{5.5}$$

which leads to the Cahn-Hilliard equation

$$\frac{\partial \phi}{\partial t} = \nabla \cdot (M(\phi)\nabla(\Psi'(\phi) - \zeta \nabla^2 \phi)) \tag{5.6}$$

The mobility function is defined as $M(\phi) = \phi(1-\phi)$. $\Psi'(\phi)$ represents the chemical potential given by

$$\Psi'(\phi) = \frac{1}{2\theta} \log\left(\frac{\phi}{1-\phi}\right) + 1 - 2\phi \tag{5.7}$$

The parameter θ represents the ratio between the critical and the absolute temperature with the value of 3/2 to be in the spinodal regime. In our model, the whole transport equation for small particles including the CH equation can be written as:

$$\frac{\partial c_s}{\partial t} + v_s \cdot \nabla c_s = \nabla \cdot \boldsymbol{D} \nabla c_s + \nabla \cdot (M(c_s)\nabla(\Psi'(c_s) - \zeta \nabla^2 c_s)) \tag{5.8}$$

where we assume the mobility $M(c_s)$ is irrelevant to c_s for simplicity and satisfies the relation:

$$M = b_{seg} \dot{\gamma} d_p^2, \tag{5.9}$$

where $\dot{\gamma}$ is the shear rate and d_p is the particle diameter. In this work shear rate can be expressed as the equation of strain rate in FEM:

$$\dot{\gamma} = \sqrt{2 \dot{e}^P_{i,j} \dot{e}^P_{i,j}}, \tag{5.10}$$

where $\dot{e}^P_{i,j}$ is the deviatoric plastic strain rate which can be defined as $\dot{\epsilon}^P_{i,j} - (\dot{\epsilon}^P_{kk}/3)\delta_{i,j}$

5.2.3 Boundary conditions

At the bottom and top of the flowing layer (along z axis), the segregation flux is equal to the diffusive flux (Fan et al., 2014; Schlick et al., 2015). It states that if particles leave out of the boundary at the flowing layer, it is because of the effects of convection only rather than diffusion or segregation. For the percolation model, the boundary condition for small particles at z direction can be reduced to:

$$l_{seg}(1 - c_s) + \chi d_p^2 \frac{\partial}{\partial z} c_s = 0 \tag{5.11}$$

while for the CH equation, it is expressed as:

$$\chi c_s + b_{seg}(\Psi'(c_s) - \zeta \nabla^2 c_s) = 0 \tag{5.12}$$

5.3 Granular dynamics

5.3.1 governing equations

The granular material contained inside CBM is treated as a continuum medium since the dimension of CBM is far larger than the diameter of particles. Similar to other forms of matter, granular dynamics also needs to satisfy the fundamental principles of mass, momentum and energy conservation, given by Mass conservation

$$\frac{\partial \rho}{\partial t} + \nabla \cdot (\rho \boldsymbol{\nu}) = 0 \tag{5.13}$$

Momentum conservation

$$\frac{\partial (\rho \boldsymbol{\nu})}{\partial t} + \nabla \cdot (\rho \boldsymbol{\nu} \bigotimes \boldsymbol{\nu}) = \nabla \cdot \sigma + \rho \boldsymbol{b} \tag{5.14}$$

Energy conservation

$$\frac{\partial (\rho \epsilon)}{\partial t} + \nabla \cdot (\epsilon \boldsymbol{\nu}) = \boldsymbol{\sigma} : \dot{\boldsymbol{\epsilon}} \tag{5.15}$$

where ρ refers to the bulk density of granular material, $\boldsymbol{\sigma}$ is Cauchy stress tensor, $\boldsymbol{b}$ is body force, $\boldsymbol{v}$ is velocity vector and ϵ is the internal energy per unit volume. $\dot{\boldsymbol{\epsilon}} =$

$(1/2)(\nabla v + (\nabla v)^T)$represents the strain rate.

5.3.2 Mohr-Coulomb model

In the Mohr-Coulomb elastoplastic model, a linear relation between stress and elastic strain is described as:

$$\sigma_{ij} = D^{el}_{ijkl}\epsilon^{el}_{kl} \tag{5.16}$$

where σ_{ij} is the total stress; ϵ^{el}_{kl} is the elastic strain; and D^{el}_{ijkl} is the fourth-order tensor of elasticity.
The yield condition is given by:

$$R_{mc}q - p\tan\varphi - c = 0 \tag{5.17}$$

where

$$R_{mc} = \frac{1}{\sqrt{3}\cos\varphi}\sin(\Theta + \frac{\pi}{3}) + \frac{1}{3}\cos(\Theta + \frac{\pi}{3})\tan\varphi$$

φ is the slope of the Mohr-Coulomb yield surface in the $p - R_{mc}q$ stress plane, which is commonly referred to as the friction angle of the material and can depend on temperature and predefined field variables. $p = -\frac{1}{3}\mathrm{trace}(\sigma_{ij})$ is the first invariant of stress representing the equivalent pressure; $q = \sqrt{\frac{3}{2}S_{ij}S_{ij}}$ is the Mises equivalent stress and S_{ij} is the deviatoric stress; φ and c are the angles of internal friction and and the cohesion of granular material, respectively. Θ is the deviatoric polar angle defined as $\cos(3\Theta) = (r/q)^3$ where $r = (\frac{9}{2}S_{ji}S_{jk}S_{ki})^{\frac{1}{3}}$ is an invariant measure of deviatoric stress. The friction angle, φ, controls the shape of the yield surface in the deviatoric place. The friction angle range is $0° \leq \varphi < 90°$. In the case of $\varphi = 0°$ the Mohr-Coulomb model reduces to the pressure-independent Tresca model with a perfectly hexagonal deviatoric section. In the case of $\varphi = 90°$, the Mohr-Coulomb model reduces to the "tension cutoff" Rankine model with a triangular deviatoric section and $R_{mc} = \infty$.
Granular flow can be well described as flow rules. The flow potential G is chosen to be a hyperbolic function in the meridional stress plane and a smooth elliptic function in the

deviatoric stress plane, defined by:

$$G = \sqrt{(\epsilon c\mid_0 \tan\psi)^2 + (R_{mw}q)^2} - p\tan\psi \tag{5.18}$$

and

$$R_{mw} = \frac{4(1-e^2)\cos^2\Theta + (2e-1)^2}{2(1-e^2)\cos\Theta + (2e-1)\sqrt{4(1-e^2)\cos^2\Theta + 5e^2 - 4e}} \times \frac{3-\sin\varphi}{6\cos\varphi} \tag{5.19}$$

where ψ is the dilatancy angle of material, $c|_0$ is the initial cohesion yield stress, ϵ is a parameter that characterizes the eccentricity of the flow potential. e referred to as the deviatoric eccentricity, describing the "out-of-roundedness" of the deviatoric section in terms of the ratio between the shear stress along the extension meridian and the shear stress along the compression meridian, is a function of the internal friction angle φ, given as $e = (3-\sin\varphi)/(3+\sin\varphi)$.

An additive strain rate decomposition is assumed:

$$d\boldsymbol{\varepsilon} = d\boldsymbol{\varepsilon}^{el} + d\boldsymbol{\varepsilon}^{pl}, \tag{5.20}$$

where $d\boldsymbol{\varepsilon}$ is the total strain rate, $d\boldsymbol{\varepsilon}^{el}$ is the elastic strain rate, and $d\boldsymbol{\varepsilon}^{pl}$ is the inelastic (plastic) strain rate.

The constitutive flow rule can be written as:

$$d\boldsymbol{\varepsilon} = \frac{d\boldsymbol{\varepsilon}}{g}\frac{\partial G}{\partial \boldsymbol{\sigma}}, \tag{5.21}$$

where g can be written as

$$g = \frac{1}{c}\boldsymbol{\sigma} : \frac{\partial G}{\partial \boldsymbol{\sigma}} \tag{5.22}$$

Three dimensional (3D) thick drums and quasi-2D thin drums are the two typical commonly studied drums in many literatures (Zheng and Yu, 2015b; Santos et al., 2013; Khakhar, McCarthy, Shinbrot and Ottino, 1997). In a 3D drum, particle flow in the middle can be hardly influenced by the friction with walls at both ends of the drum, while the interaction with walls plays an important role in the flowing process in a 2D drum. However, in order to simplify the numerical simulation, a quasi-2D thin drum is adopted under the

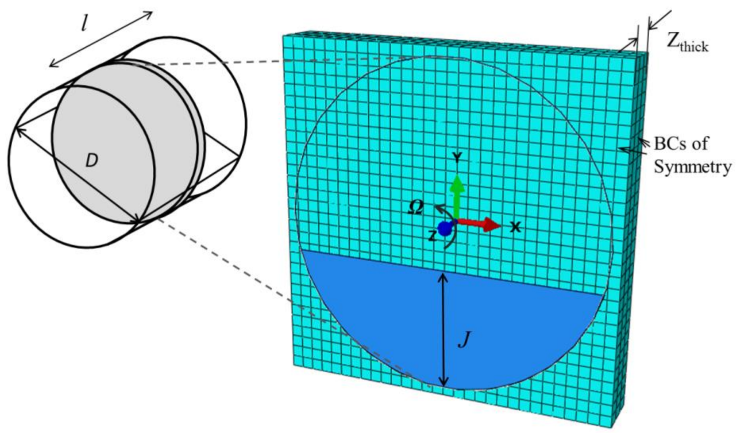

Figure 5.1: Drum geometry and mesh condition (Zheng and Yu, 2015b).

Parameters	Symbols	Values	Range of variation
Drum diameter	D	0.16 m	0.16 m - 0.28 m
Drum thickness	Z	0.01 m	-
Particle diameter	d_p	0.001 m	-
Particle density	ρ	1500 kg/m^3	-
Poisson's ratio	ν	0.3	-
Young's modulus	E	1×10^6 Pa	-
Internal friction angle	φ	20°	15° - 30°
Friction coefficient of material-wall interaction	μ	0.3	0.1 - 0.3
Cohesion yield stress	c_y	0 Pa	-
Diffusion coefficient	χ	0.1	0.1 - 1
Percolation length	l_{seg}	0.001 m	0.001 m - 0.005 m
Mesh size	m_s	0.001 m	0.001 m - 0.002 m
Rotation speed	ω	15 rpm	-
Filling level	f	43%	-

Table 5.1: Parameters used in the simulation

periodic boundary condition (BC) treatment in this work. Granular flow is described by the Mohr-coulomb elastic-plastic modelling. The geometry and mesh condition are similar to the work (Zheng and Yu, 2015b) (shown in Fig.5.1). The parameters of the drum and the granular material are listed in Table 5.1.

5.4 Implementation of segregation in FEM

A operator splitting method (Karlsen et al., 2001; Lanser and Verwer, 1999; Fan et al., 2014) which decomposes a complex equation into two parts for obtaining numerical solutions is applied in this work. The concentration equation 5.4, 5.8 can be split into the LHS part which indicates the convection mechanism during the mixing process and the RHS part representing the diffusion term. So that the whole concentration equation for small particles can be decomposed into a couple of differential equations:

$$
\begin{aligned}
\frac{\partial c}{\partial t} &= -v \cdot \nabla c \quad \text{(convection)} && (5.23)\\
\frac{\partial c}{\partial t} &= \nabla \cdot \boldsymbol{D} \nabla c - \frac{\partial}{\partial z}(w_{p,s} c) \quad \text{(diffusion+percolation)} && (5.24)\\
&= \nabla \cdot \boldsymbol{D} \nabla c + \nabla \cdot (M(c) \nabla (\Psi'(c) - \zeta \nabla^2 c)) \quad \text{(diffusion+CH equation)} && (5.25)
\end{aligned}
$$

The numerical solution of concentration $c_{i,j}^{t_c}$ of the LHS convection part (Eq.5.23) at each time step t and the node $(i,\, j)$ can be derived from the FEM dynamics and obtained by ABAQUS. The RHS diffusion-percolation part (Eq.5.24) can be solved numerically by the Finite Central Difference Method (FCDM). A 1D case of FCDM can be illustrated as the way bellow. The diffusion-percolation term in form of continuous space and time is broken down into a set of discrete quantities located at the nodes of the FEM grid :

$$
\begin{aligned}
\left(\frac{\partial c}{\partial x}\right)_{i,j} &= \frac{c_{i+1,j} - c_{i-1,j}}{2\triangle x} + O(\triangle x), && (5.26)\\
\left(\frac{\partial^2 c}{\partial x^2}\right)_{i,j} &= \frac{c_{i+1,j} - 2c_{i,j} + c_{i-1,j}}{(\triangle x)^2} + O((\triangle x)^2), && (5.27)\\
\left(\frac{\partial^4 c}{\partial x^4}\right)_{i,j} &= \frac{c_{i+2,j} - 4c_{i+1,j} - 4c_{i-1,j} + 6c_{i,j} + c_{i-2,j}}{(\triangle x)^4} + O((\triangle x)^2), && (5.28)
\end{aligned}
$$

where i, j are the node numbers of the mesh created by FEM and $\triangle x$ is the length of interval between two nodes. $O(\triangle x)^2$ stands for infinitesimal of high orders. The parts of percolation $c_{i,j}^{t_p}$, diffusion $c_{i,j}^{t_d}$, and CH $c_{i,j}^{t_{CH}}$ can be obtained by Eq.5.23, 5.24, 5.25, 5.26, 5.27 and 5.28:

$$
\begin{aligned}
c_{i,j}^{t_d} &= D * dt * \frac{c_{i+1,j}^{t_c} - 2c_{i,j}^{t_c} + c_{i-1,j}^{t_c}}{(\triangle x)^2} && (5.29)\\
c_{i,j}^{t_p} &= l_{seg} * dt * \frac{c_{i+1,j}^{t_p} - c_{i-1,j}^{t_p}}{2\triangle x} && (5.30)\\
c_{i,j}^{t_{CH}} &= M * dt * \frac{\Psi'(c_{i+1,j}^{t_c}) - 2\Psi'(c_{i,j}^{t_c}) + \Psi'(c_{i-1,j}^{t_c})}{(\triangle x)^2}\\
&\quad - \zeta * dt * \frac{c_{i+2,j}^{t_c} - 4c_{i+1,j}^{t_c} - 4c_{i-1,j}^{t_c} + 6c_{i,j}^{t_c} + c_{i-2,j}^{t_c}}{(\triangle x)^4} && (5.31)
\end{aligned}
$$

As the flow chart (Fig.5.3) indicates, the whole FEM diffusion dynamics is processed explicitly via the ABAQUS solver. To get the concentration of each node at time step t+1, the concentration $c_{i,j}^{t_c}$ at each time step t calculated by FEM convection dynamics continues to be updated through the following algorithm.

For the percolation mechanism,

$$\begin{aligned} c_{i,j}^{t+1} &= c_{i,j}^{t_c} + c_{i,j}^{t_d} + c_{i,j}^{t_p} \\ &= c_{i,j}^{t_c} + D * dt * \frac{c_{i+1,j}^{t_c} - 2c_{i,j}^{t_c} + c_{i-1,j}^{t_c}}{(\triangle x)^2} + l_{seg} * dt * \frac{c_{i+1,j}^{t_p} - c_{i-1,j}^{t_p}}{2\triangle x}. \end{aligned} \tag{5.32}$$

For the CH equation,

$$\begin{aligned} c_{i,j}^{t+1} &= c_{i,j}^{t_c} + c_{i,j}^{t_d} + c_{i,j}^{t_{CH}} \\ &= c_{i,j}^{t_c} + D * dt * \frac{c_{i+1,j}^{t_c} - 2c_{i,j}^{t_c} + c_{i-1,j}^{t_c}}{(\triangle x)^2} \\ &\quad + M * dt * \frac{\Psi'(c_{i+1,j}^{t_c}) - 2\Psi'(c_{i,j}^{t_c}) + \Psi'(c_{i-1,j}^{t_c})}{(\triangle x)^2} \\ &\quad + \zeta * dt * \frac{c_{i+2,j}^{t_c} - 4c_{i+1,j}^{t_c} - 4c_{i-1,j}^{t_c} + 6c_{i,j}^{t_c} + c_{i-2,j}^{t_c}}{(\triangle x)^4}. \end{aligned} \tag{5.33}$$

, where $c_{i,j}^{t+1}$ refers to the material concentration at time step $t+1$. The updated $c_{i,j}^{t+1}$ will be involved in a new round of convection calculation by the ABAQUS solver. For the calculation of boundary condition, the elements out of boundary adjacent to the elements inside the boundary can be calculated through Eqs.5.11 and 5.12 as

For percolation:

$$c_s^{z+1} = c_s^z - \frac{m_s l_{seg}}{\chi d_p^2} c_s^z (1 - c_s^z) \tag{5.34}$$

$$c_s^{z-1} = c_s^z + \frac{m_s l_{seg}}{\chi d_p^2} c_s^z (1 - c_s^z), \tag{5.35}$$

in which the relation $0.1 < \frac{m_s l_{seg}}{\chi d_p^2} < 1$ should be satisfied.

For CH:

$$c_s^{i+1} = 2c_s - c_s^{i-1} - \frac{m_s^2}{\gamma_i}\left(\frac{\chi}{d_{seg}} c_s + \Psi'(c_s)\right), \tag{5.36}$$

where $i = x, y, z$.

The whole coupling procedure is implemented via the user subroutine VUSDFLD.

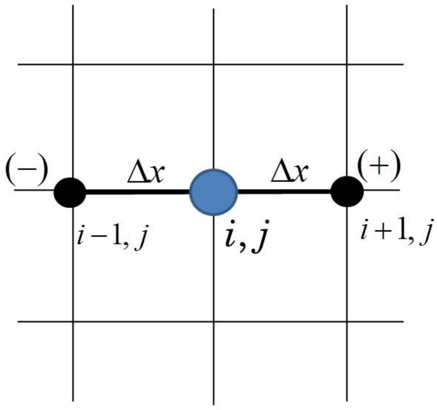

Figure 5.2: The integration grids in FEM mesh configuration.

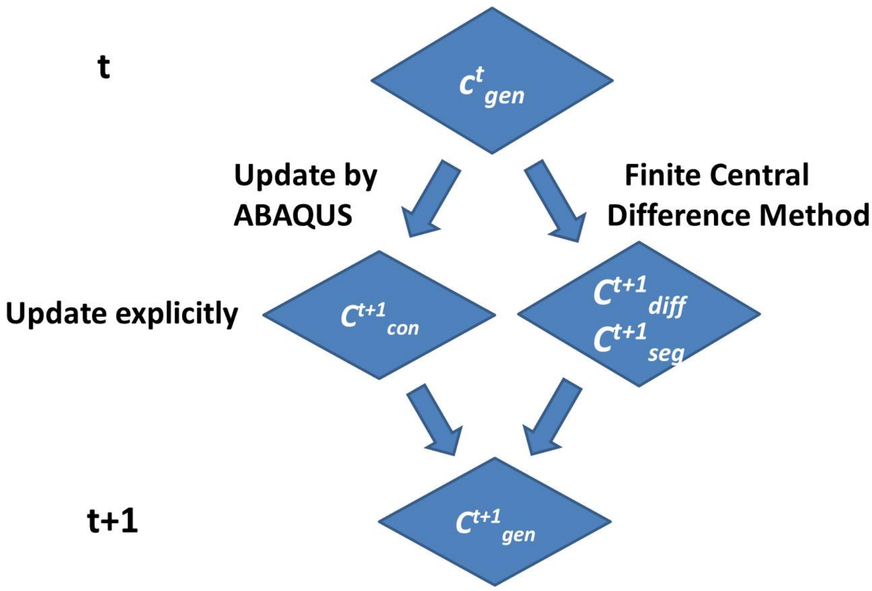

Figure 5.3: The algorithm of updating variables by the FEM explicit solver.

5.5 Results and discussion

5.5.1 Radial segregation with 2D FEM percolation model

Pattern formation and segregation index

The eulerian material with volume fraction of 0.5 (actually a small fluctuation around 0.5 is applied at the calculating grid nodes) fills the 2D drum until 50% level is satisfied. The drum with radius 0.14 m starts to rotate at 0.4 rad/s. After 1/4 revolution, the congregation of small particles appears in the middle of the granular bulk. The top of Fig.5.4 shows the pattern evolution of small particle concentration at 4 different time steps in form of rotations (1/4 rotation - 1 rotation). In the flowing layer, small particles travel down to the bottom through voids between particles and gather in the core center of particle beds. On the contrary, large particles float upward to the top of the flowing layer and accumulate at the surface near the wall. After 1/2 rotation, most of small particles are segregated and concentrate at the core in the center. After 1 rotation, more segregated particles contribute to the core formation and the degree of segregation is thereby enhanced compared to the case at 1/2 rotation. The segregating pattern is compared with experiments shown at the bottom of Fig.5.4. In the experiment, the mixture contains 1 mm small black particles and 3 mm white large particles. With no adjustable fitting parameters in FEM model, only qualitative agreement between model and experiment has been reached. The core of small particles representing segregation can be easily noticed, but the radius of the core is much smaller than that from experiment. Despite the quantitative failure, the qualitative similarity is still able to show the success of the FEM segregation model to some extent. To make the prediction of FEM model quantitatively matches the DEM simulation unseasonably well, the percolation length l_{seg} needs to become adjustable. Fig.5.6 shows the comparison of segregation indexes between FEM and DEM when l_{seg} changes from 0.01 mm to 0.08 mm. The case of $l_{seg} = 0.06$ mm presents a relatively good consistency with DEM in segregation index and pattern formation as well. The case is shown in Fig.5.5 and Fig.5.6 in which the core size of small particles is large enough in comparison with DEM. The segregation index can be defined in FEM model:

$$I = \sqrt{\frac{\sigma^2}{\sigma_0^2}}, \tag{5.37}$$

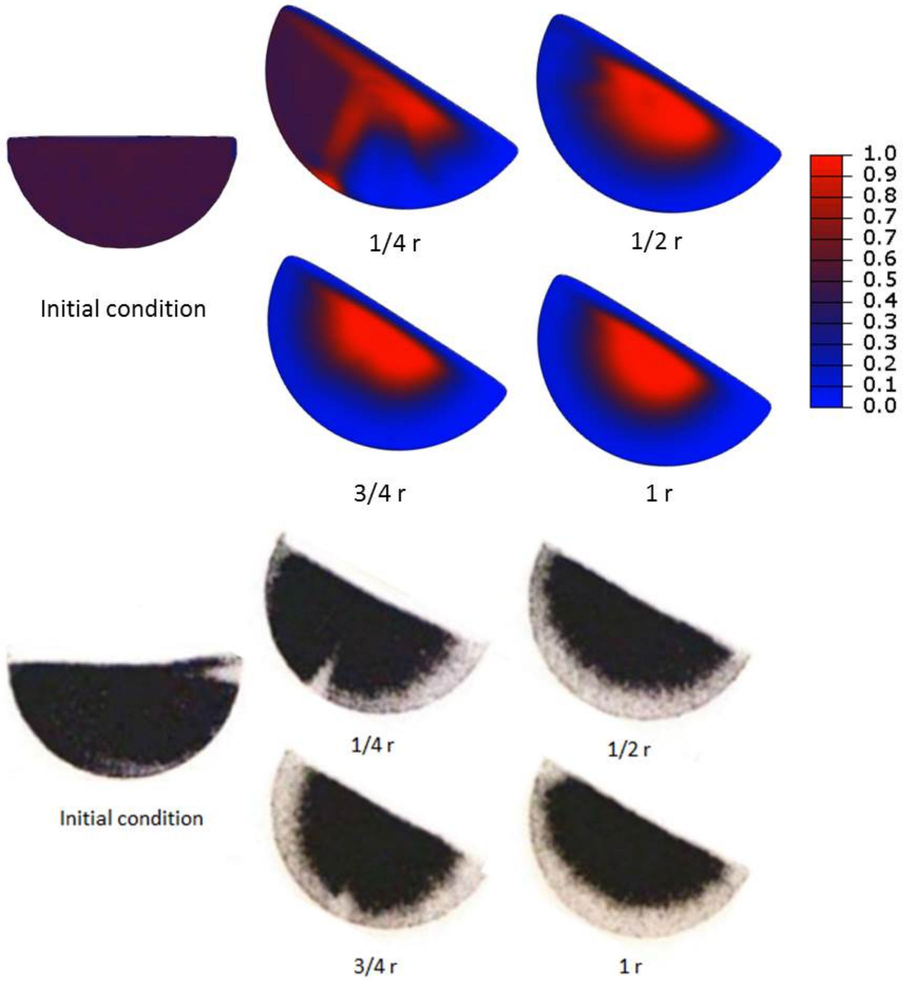

Figure 5.4: Pattern evolution of segregation in the particle-filled portion of the tumbler. Top: FEM pattern. The contour shows the concentration of small particles. Bottom: Experiment results (Schlick et al., 2015). $\omega = 0.4$ rad/s, $D_{drum} = 0.28$ m, $\chi = 0.1$, $l_{seg} = 0.001$ m.

,where σ is defined as:

$$\sigma = \sqrt{\frac{1}{N}\sum_{i=1}^{n}(c_i - \bar{c}_t)^2},$$

N is the total number of nodes. c_i is the concentration of particle at the node i. σ_0^2 is the variance of fully-segregated state and σ^2 is the variance of the mixture at time t, where $\sigma_0^2 = c(1-c)$ and c represents the particle number ratio of the target particles to the total particle number in the binary mixture. $\bar{c}_t$ represents the average of c_i at time t. I equals 0 at the initial stage because particles are well mixed at the homogeneous state ($\sigma = 0$) and equals 1 when the particles are completely mixed ideally ($\sigma = \sigma_0$). In our work, the sampling points are collected from the FEM computational grids.

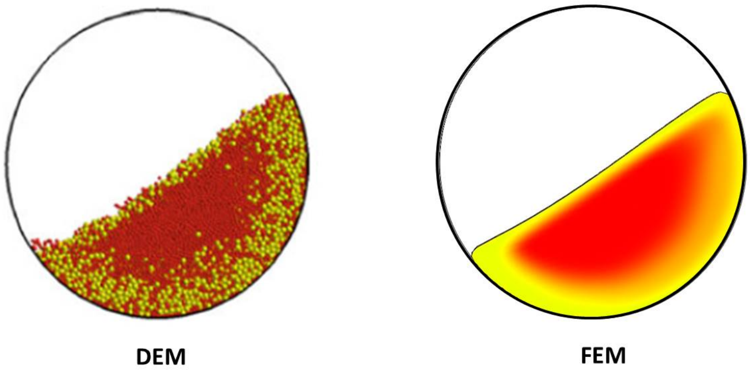

Figure 5.5: Comparison of core formation in the tumbler with DEM. The contour shows the concentration of small particles. Left: DEM (Liu et al., 2013b). Right: FEM. $\omega = 15$ rpm, $D_{drum} = 0.104$ m, $\chi = 0.1$, $l_{seg} = 0.06$ m.

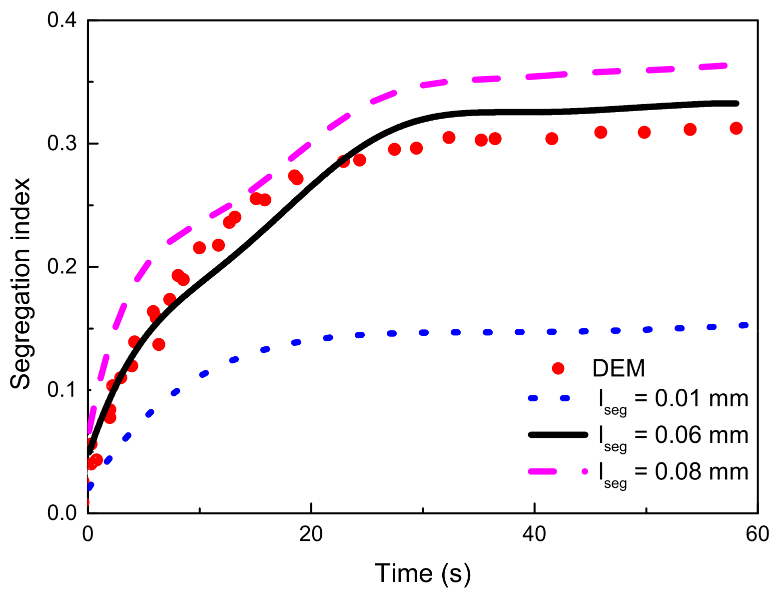

Figure 5.6: Comparison of segregation index in the tumbler with DEM when the percolation length is adjustable. $\omega = 15$ rpm, $D_{drum} = 0.104$ m, $\chi = 0.1$.

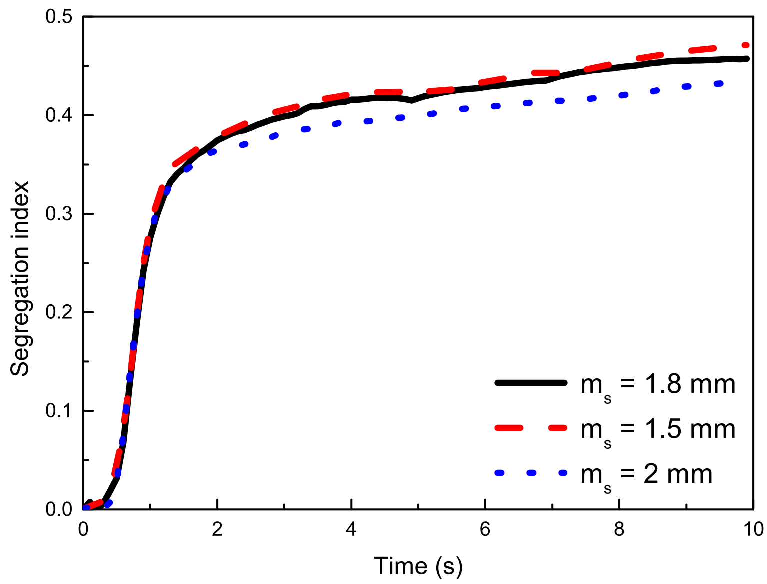

Figure 5.7: Mesh size dependency of segregation index. $\omega = 0.4$ rad/s, $D_{drum} = 0.28$ m, $l_{seg} = 1$ mm, $l_{diff} = 4$ mm.

Dependency of segregation index on mesh size

The discussion of mesh size dependency is an important step in model verification. To ensure a high accuracy of numerical simulation, the grid sensitivity and mesh dependency need to be tested at the beginning. For the FEM convection model in chapter 3, the mixing index is largely influenced by the mesh size. For the FEM convection-diffusion model in chapter 4, the mixing index stays independent of grid density when the mesh size is less than 1/3 diffusion length. For the FEM convection-diffusion-segregation model, the mesh size effect on the evolution of segregation index is shown in Fig.5.7, in which three cases with different percolation lengths (2 mm, 1.8 mm, 1.5 mm) are calculated. The evolution of segregation index tends to become faster as the mesh becomes finer. It shows little changes and reaches the convergency independent of mesh sizes and standing for a high resolution after the mesh size is below 1.5 mm. So for further analyses, the mesh size of 1.5 mm is fine enough and chosen as the criteria of calculation in the FEM segregation model. However, the quantitative relationship between the minimum mesh size required, diffusion length and percolation length is unclear and has not been decided yet and needs further investigation.

Parametric study of FEM percolation model

After a satisfied FEM model verification discussed in 5.5.1 and 5.5.1, a further parametric study is needed. In this section, the effects of percolation length, diffusion coefficient and internal friction angle on the segregation process will be explored.

In Fig.5.8, the segregation index I is plotted for the three cases of different percolation lengths. Initially, I equals zero which indicates the whole mixing is in its homogeneous state. As t increases, particles are segregated gradually and the value of I becomes larger. As t tends to become infinite, I approaches approximately a steady value which means the evolution of segregation process ends up with a partially segregated state with the segregation index less than 1. The segregation rate keeps increasing as the percolation length changes its value from $l_{seg} = 0.1$ mm to 0.3 mm. This is because the increase of percolation length means more particles penetrating into the bottom of flowing layer at every time step. Fig.5.9 shows that when the diffusion coefficient increases, the final steady value of segregation index decreases by a large amount. By contrast, the segregation rate can be less influenced than the segregation degree. The diffusion mechanism can largely cause the remixing of the segregated particles at the border between the two different-sized particles at the bottom of flowing layer. The penetration process depends less on diffusion than percolation, so that the segregation index I can be rarely changed when the diffusion effect becomes stronger. Fig.5.10 shows the evolution of segregation index when the internal friction angle changes. The segregation rate decreases with the increase of φ. A higher friction angle result in a lower segregation rate. It demonstrates a more intense convection accelerates not only the mixing process but also the segregation process. Material with a smaller φ tends to behave like liquid, leading to a larger area of flowing layer within which a great number of particles travel at a relatively rapid speed. So that with a higher percolation velocity, the percolation effect becomes prominent. On the other hand, as discussed in Chapter 4, according to the FEM diffusion model, the diffusion effect on material with a lower friction angle is largely reduced. The segregation process, as a result, is promoted finally. On the contrary, higher friction angles hinder the process of reverse diffusion.

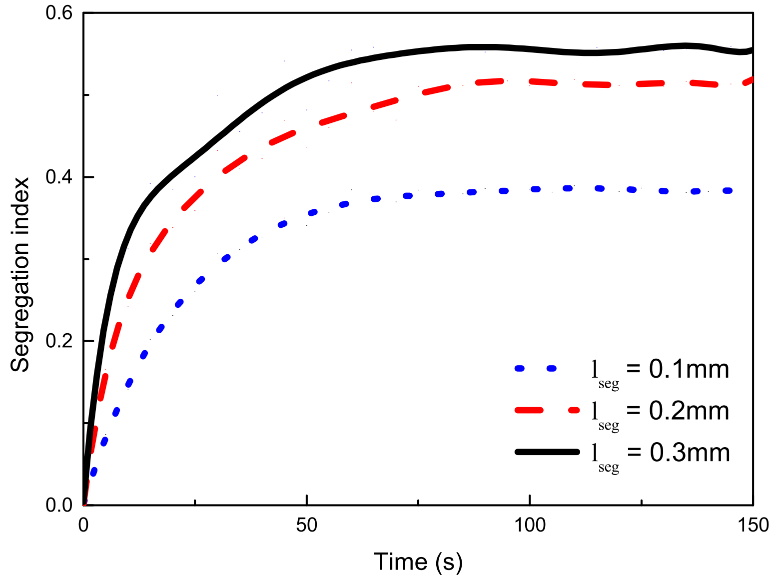

Figure 5.8: Evolution of segregation index in the tumbler for different percolation lengths. $\omega = 0.4$ rad/s, $D_{drum} = 0.28$ m, $\chi = 0.1$.

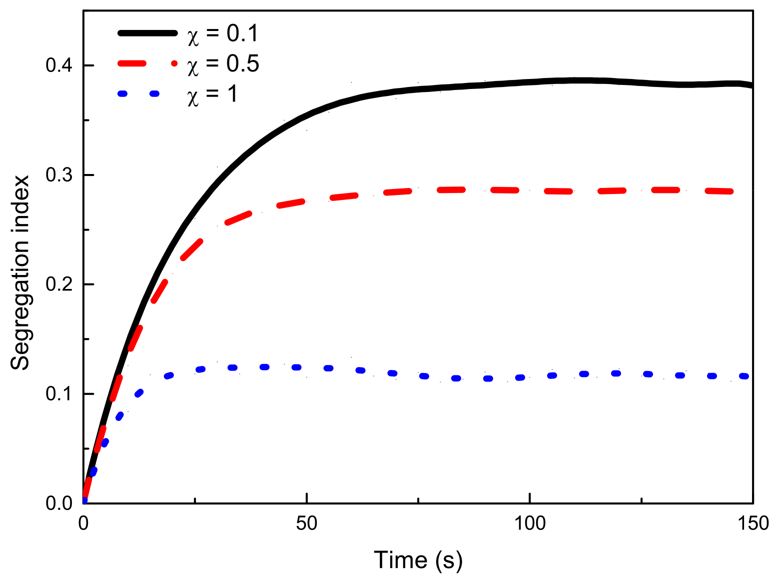

Figure 5.9: Evolution of segregation index in the tumbler for different diffusion coefficients. $\omega = 0.4$ rad/s, $D_{drum} = 0.28$ m, $l_{seg} = 0.1$ mm.

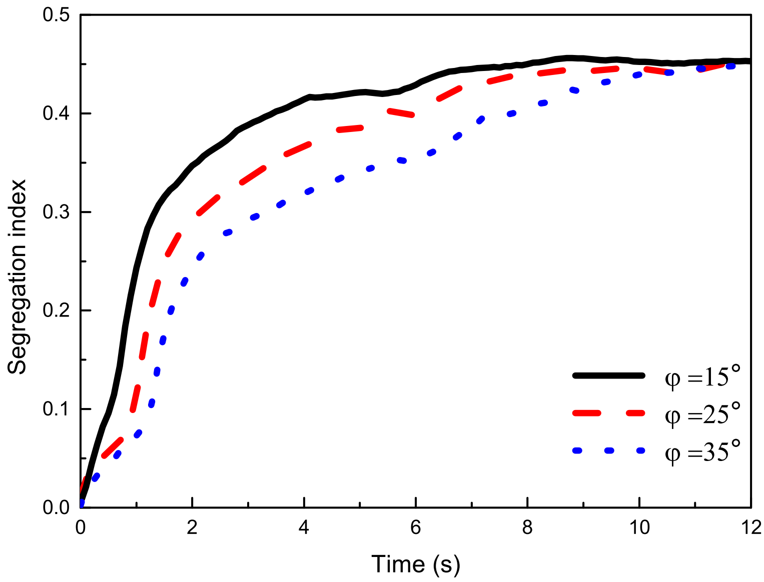

Figure 5.10: Evolution of segregation index in the tumbler for different internal friction angles. $\omega = 0.4$ rad/s, $D_{drum} = 0.28$ m, $l_{seg} = 0.1$ mm.

5.5.2 Axial segregation with 3D FEM percolation model

The axial segregation, also called band formation, has a long history of investigation. When a long thin cylindrical tumbler filled with homogeneously mixed particles with different sizes rotates at a certain speed above a threshold, the particles with the same size congregate and separate from particles of a different size. After hundreds of revolutions (usually more than 200 revs), several transverse bands vertical to the axis emerge at the surface of the granular bulk. Early research shows there are three critical factors contributing to this intriguing phenomenon: the friction between particles and wall, the repose angle of particles, and the percolation mechanism. No band formation can be observed if any one of the three conditions is absent. In this section, the 3D FEM percolation model is applied to explore the simulation of 3D axial segregation and try to unveil a better understanding toward the potential mechanism behind this.

As the geometry is shown in Fig.5.11, a 3D tumbler with the diameter of $D = 0.2$ m and length of $L = 0.5$ m is partially filled with equal-volumed but different-sized particles, rotating at the speed of 1 rad/s. In order to characterize the different repose angles for particles of different sizes, the different friction angles are introduced to apply to material nodes related to the concentration. The friction angles of different sized particles are set to be $\varphi_s = 35°$ for small sized particles, and $\varphi_l = 15°$ for large sized particles. This is based on the research fact that particles with small sizes and large internal friction angles should have a larger repose angle (Zhou et al., 2002). It is assumed in our model that the concentration at certain grid point can be calculated by the linear relation $\varphi = c_s\varphi_s + c_l\varphi_l$. The pattern evolution of axial segregation at certain time steps are shown in Fig.5.12. In the first stage (1 r - 2 r), big particles with a lower concentration of small particles (in blue) congregate at the verge of the wall. At the stage of 3 r - 5 r, core formation in radial segregation appears in the inner part of the bulk. Higher concentration of small particles can be observed alongside the blue band near the wall and in the middle of the long particle assembly. At the next stage (6 r - 10 r), the concentration beneath the surface can be higher and more evident as the process continues and bands of small particles turn out to show up above the surface. The bridges between two small particle bands are noticeable and will not disappear for the rest of revolutions. The final steady state is shown at 12 r. Three red bands in high concentration of small particles are remarkably distinguishable. A relatively lower concentration in the vicinity of 0.4 meaning large particle gathering is found at either end of the wall. Different repose angles of assembly (33.69° for small particles , 30° for mixing particles) are demonstrated by the cross-section as shown in Fig.5.14.

The formation of band can be explained by the axial velocity field caused by wall friction and different dynamic angle of repose. Fig.5.15 shows the curved velocity field on the band surface. Because of the frictional end walls, particles near the wall in the upstream have a higher repose angle and move away in the flowing layer and move back in the downstream. During the moving process, some small particles are transferred to the solid regime and never flow back to the wall in the downstream. In this way, more large particles congregate at the end of the wall. The difference of repose angle leads to a further curved flow field, which contributes to the stable band of small particles in the middle. However, some problems still remain unsolved. Compared to the band formation of DEM results provided in Fig.5.13, the band of large particles adjacent to the middle band of small particles is still absent and the cause of bands in the middle is complex and remain mysterious for the percolation theory gives limited explanations. All of these phenomena and explanations need further study in future work.

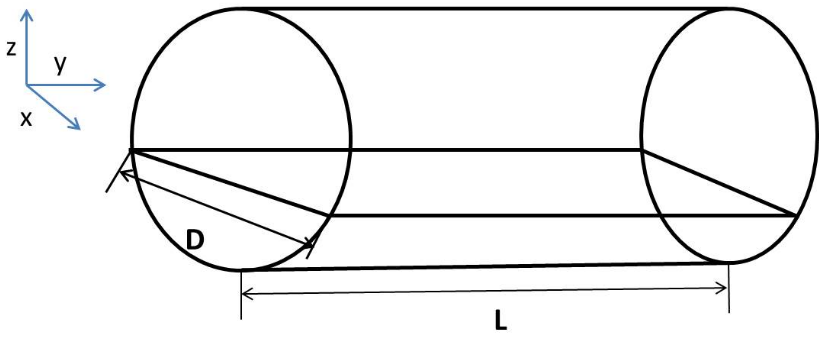

Figure 5.11: The geometry of the 3D tumbler. $D_{drum} = 0.2$ m, $L = 0.5$ m.

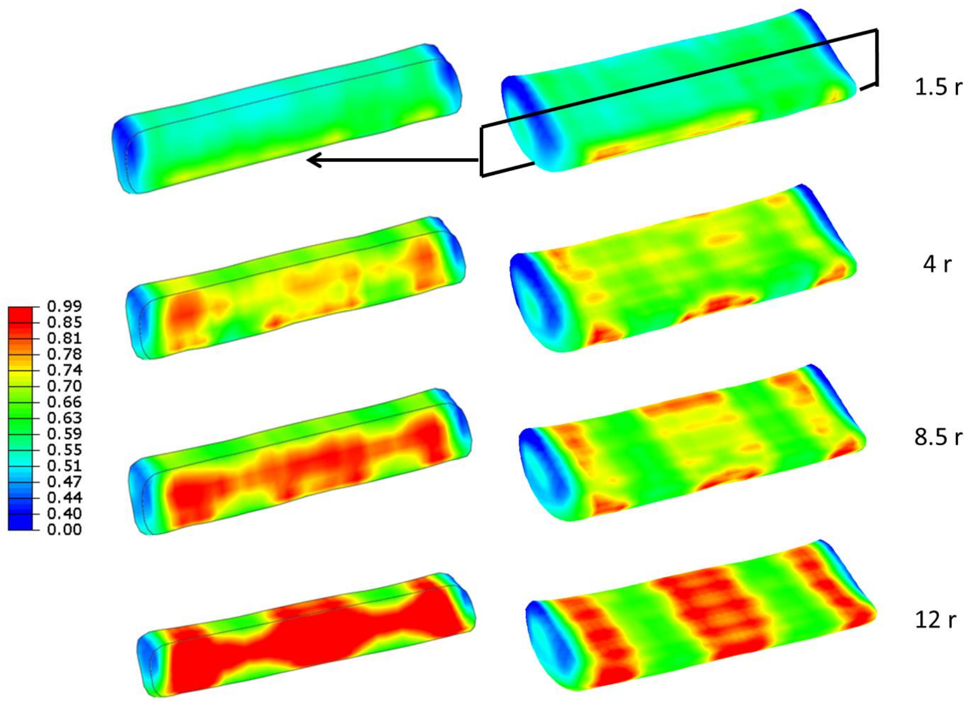

Figure 5.12: The evolution of band formation in the 3D tumbler. The contour shows the concentration of small particles. The left is a vertical plane in the middle of the granular bulk. $D_{drum} = 0.2$ m, $L = 0.5$ m, $\omega = 1$ rad/s, $l_{seg} = 0.1$ mm.

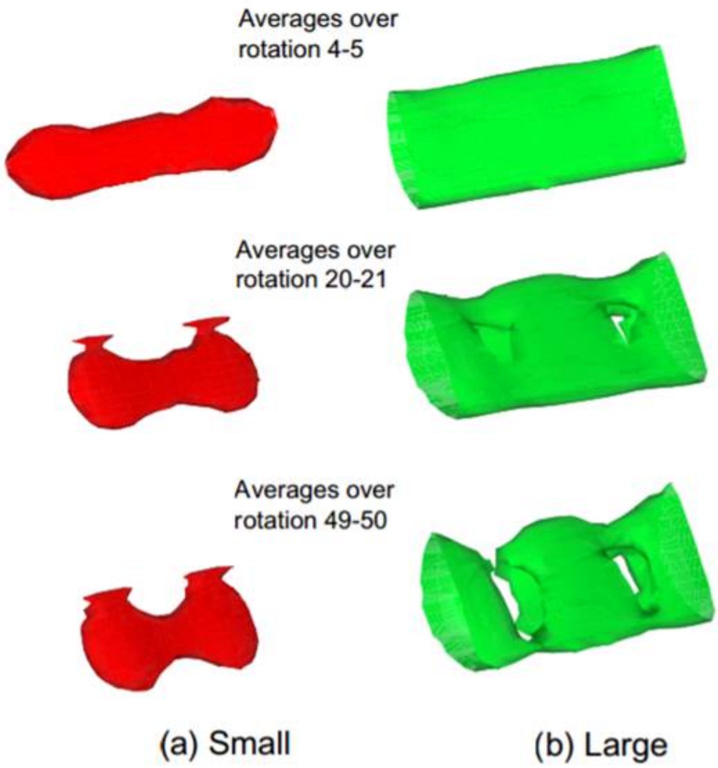

Figure 5.13: DEM results of the evolution of band formation in the 3D tumbler (Chen et al., 2011). The red material (left) refers to small particles and the green material (right) refers to large particles

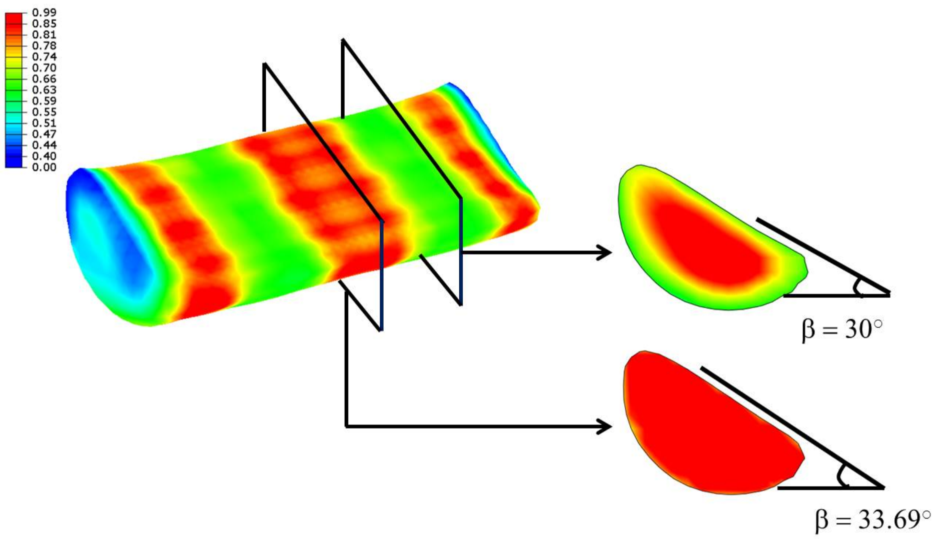

Figure 5.14: Intersection of bands with different repose angles.

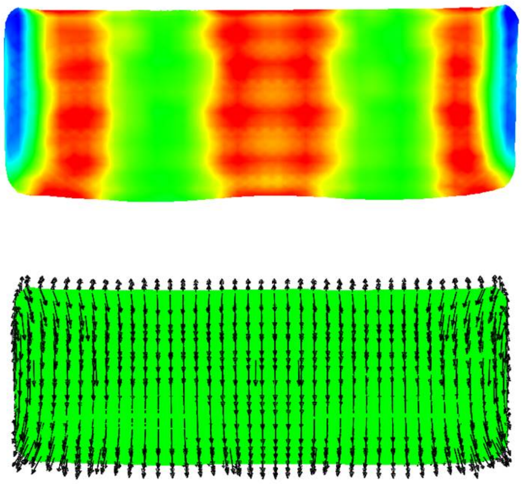

Figure 5.15: The curved flow field related to the axial bands.

5.5.3 Radial segregation with 2D FEM CH model

Since a lot of research indicates that the evolution of granular coarsening and band structure in a 3D cylinder is analogous to the spinodal decomposition and can be described by the CH equation (Van Noije and Ernst, 2000; Orza et al., 1997; Wakou et al., 2002; Puri and Hayakawa, 2001b,a), it is interesting to apply the FEM CH model to study granular segregation and test its applicability. Prior to the 3D study, the 2D CH FEM segregation model is tested in a rotating tumbler with the initially mixed materials at the filling level of 40% as shown in Fig.5.16. The drum starts to rotate at 10 rpm at the beginning before a small core representing small sized particles appears in the center at 1.5 revs. The core gets bigger as the drum continues to rotate until it is stabilized at 10.5 revs.

Fig.5.17 and 5.18 shows I as a function of time for different values of b_{seg} and ζ. Parametric study shows if b_{seg} changes to a lager value, the process has a higher segregation rate while the segregation degree remains unchanged. On the contrary, the large value of ζ leads to a lower segregation degree with segregation rate unchanged. If both b_{seg} and ζ are adjustable, the segregation index I from FEM matches that from DEM by the fitting method as the Fig.5.19 shows. However, some undesired nonphysical results show up. As shown in Fig.5.18, when ζ stays at a small value ($\zeta = 1$), the core formation of segregation can be produced by the FEM CH model. If ζ increases to a lager value ($\zeta = 8$), a complete segregation which separates two kinds of particles in two sides can be noticed in the pattern. So far the side by side segregation pattern has not been observed in either simulations or experiments.

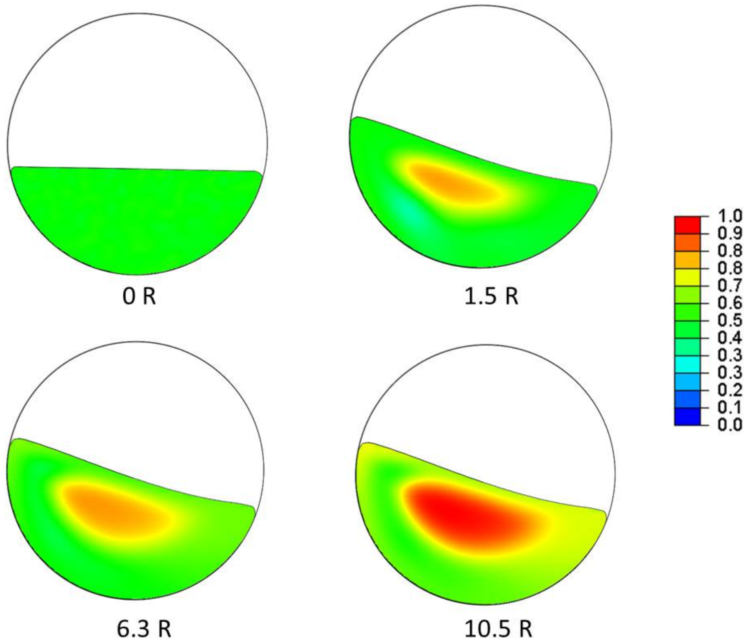

Figure 5.16: The evolution of core formation in 2D tumbler. The contour shows the concentration of small particles. $\omega = 10$ rpm, $D_{drum} = 0.15$ m, $\chi = 0.1$, $b_{seg} = 0.1$, $\zeta = 1$.

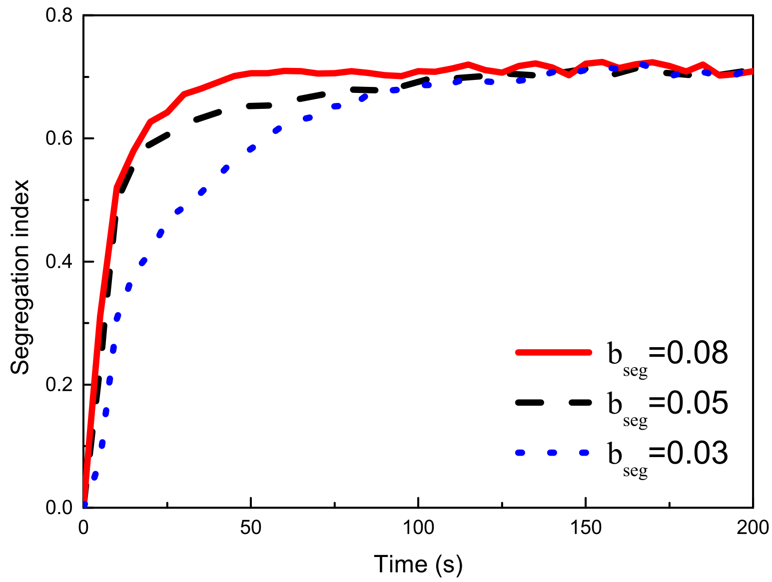

Figure 5.17: Time evolutions of segregation index in the tumbler for different diffusion coefficients. $\omega = 10$ rpm, $D_{drum} = 0.15$ m, $b_{seg} = 0.1$, $\zeta = 1$.

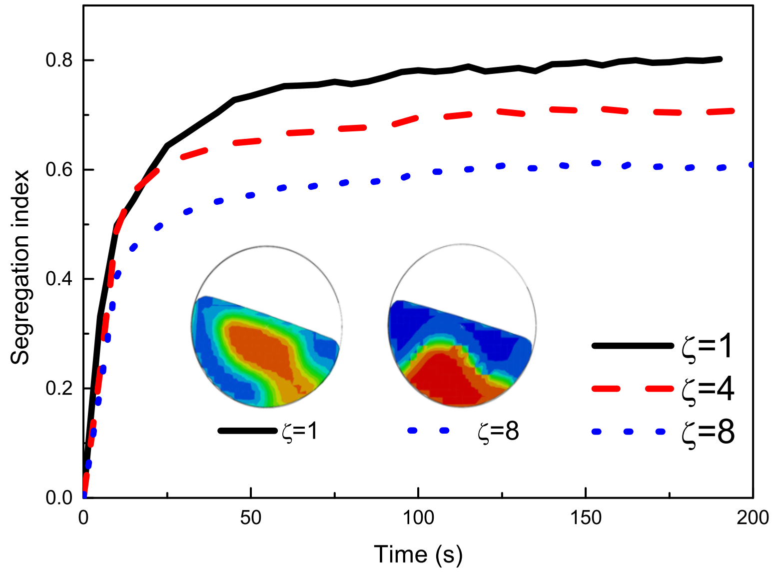

Figure 5.18: Time evolutions of segregation index in the tumbler for different segregation coefficients. $\omega = 10$ rpm, $D_{drum} = 0.15$ m, $\chi = 0.1$, $\zeta = 1$.

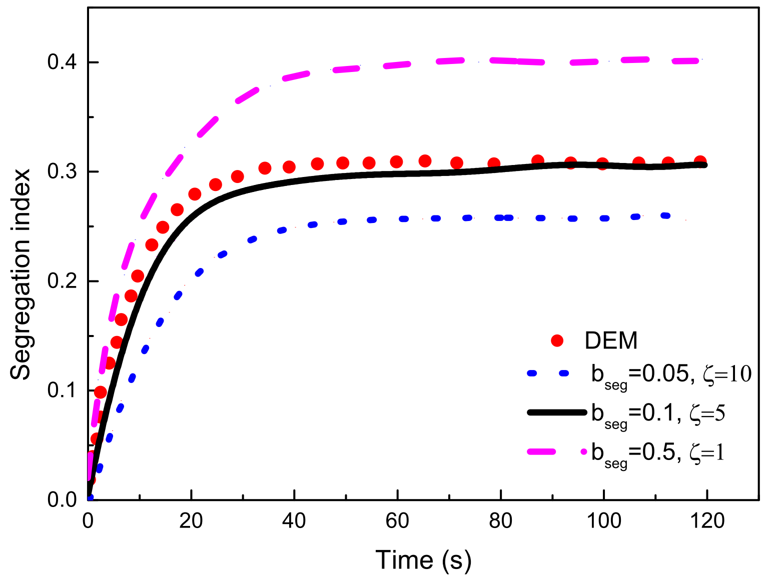

Figure 5.19: Comparison of segregation index in the tumbler with DEM $\omega = 15$ rpm, $D_{drum} = 0.104$ m, $\chi = 0.1$, $\zeta = 1$.

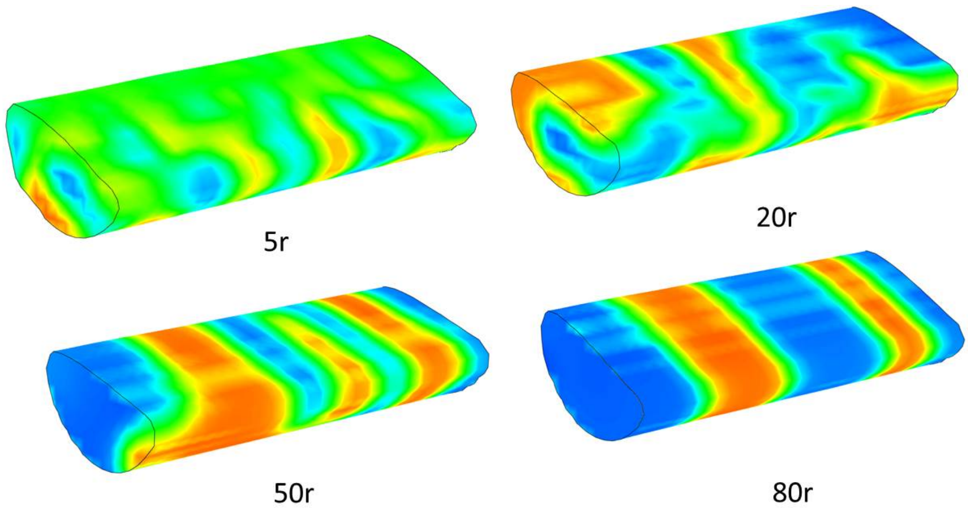

Figure 5.20: The evolution of band formation with CH FEM model in the 3D tumbler. The contour shows the concentration of small particles. The legend is the same as in Fig.5.16. $D_{drum} = 0.2$ m, $L = 0.5$ m, $\omega = 1$ rad/s, $b_{seg} = 0.1$, $\chi = 0.1$, $\zeta = 1$.

5.5.4 Axial segregation with 3D FEM CH model

The 3D CH FEM model is used to simulate the axial band formation in a long cylindrical drum. The no flux boundary condition in axial direction is applied, so walls are absent at both ends and axial flow does not exist. As the Fig.5.20 shows, the particles start to segregate into small clusters by spinodal decomposition at 5 revs. Those clusters with the same species move together, forming large islands at 20 revs. Influenced by the flow field, the islands are stretched into long thin stripes at 50 revs. As the drum continue to rotates, the long thin stripes coalesce into wide bands and finally merge into five stable bands at 80 revs at the final stage. Although 5 bands can be carried out, the physical meaning of segregation is unclear and can not be well understood by the current CH model. Fig.5.21 shows the transverse section of spinodal decomposition in the granular bulk. Unlike the core and bridge formation beneath the surface shown in Fig.5.12, the spinodal decomposition also occurs inside. It is the nonphysical and undesired numerical results that should be avoided in the segregation model.

5.6 Conclusions

In this chapter, A general 3D FEM convection-diffusion-segregation mixing model is developed based on the operator splitting method. The segregation term is established based on the percolation theory, which is coupled to the FEM convection part by the finite central

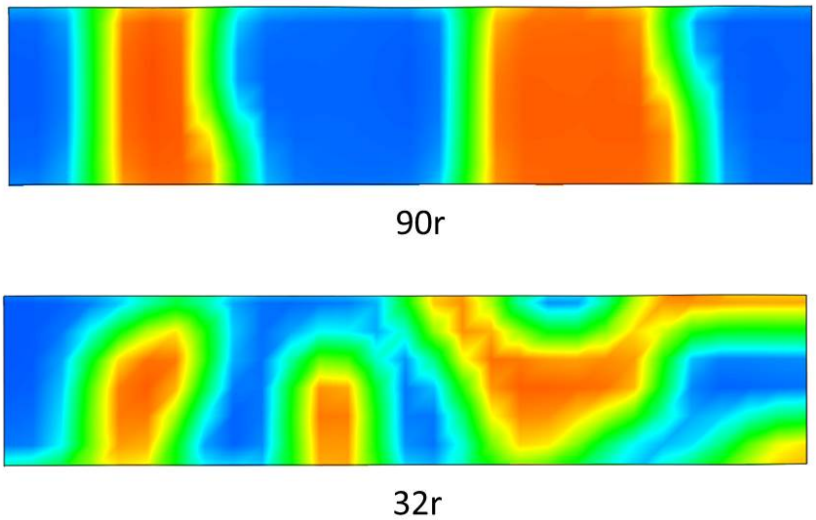

Figure 5.21: Transverse-section of band formation with CH FEM model in the 3D tumbler. Parameters are the same as in Fig.5.20.

difference method. The percolation model is validated through the test of radial segregation in a 2D rotating drum by comparison of DEM. Parametric studies are carried out to investigate the effect of percolation length and diffusion coefficient on the segregation rate and degree. The axial segregation regarding band formation is studied by the 3D FEM percolation model and CH model respectively. The results are discussed and compared with DEM simulation. The following conclusions can be drawn from this study:

- The pattern of radial segregation produced by the percolation model is consistent with that from DEM. The segregation indices of FEM can match that of DEM match if the percolation length is adjustable. The percolation length determines the segregation rate and degree while the diffusion coefficient largely affects the segregation degree. Small friction angles representing fast speeds of flow and strong convection accelerate the segregation process by increasing the segregation rate.

- Only by the percolation model, the 3D axial segregation can be produced qualitatively. The band formation results from three critical factors: radial segregation, wall interaction, and different particle repose angles. However, the number of stripes and the band width of large particles can not match the experiment results quantitatively.

- Compared with the percolation model, the CH segregation model reproduces a more reasonable surface strips profile. However, nonphysical and undesired results by spinodal decomposition are noticeable, which should be avoided in a further model development and case study.

5.7 Nomenclature

ϱ bulk density of granular material [kg/m^3]

E Young's modulus [Pa]

ν Poisson's ratio [-]

φ internal friction angle [degree]

c_y shear cohesion [Pa]

c volume fraction [-]

μ Coulomb friction between granular material and drum wall [-]

μ_s sliding friction coefficient in DEM simulation [-]

N_{inter} interfacial area in form of number of nodes [-]

M mixing index [-]

σ standard deviation of concentration [-]

D diffusivity

D_{drum} drum diameter

$\dot{\gamma}$ shear rate

d_p diameter of particles

χ diffusivity coefficient

m_s mesh size

l_{seg} segregation length

I segregation index

Chapter 6

Application of FEM model for Mipro mixer

6.1 Introduction

Granular mixing is a vital unit operation encountered with a variety of manufacturing processes such as food, cosmetics, and pharmaceutical industries. It has also been a great interest of research for many years. The purpose of mixing is to blend fully separated particles with different material properties into a homogenous mixture. For various industries, the types of mixers are very important and should be carefully selected. Of the diverse mixers in application, more emphasis of research has been put on bladed mixers for its ability to generate high shear forces which are advantageous for obtaining a high quality of mixing.

The MiPro mixer (Procept, Belgium) (Nguyen et al., 2014; Watson et al., 2009; Khalilitehrani et al., 2015; Darelius et al., 2008b, 2007) is such a bladed cylindrical mixer consisting of a central shaft with three blades at the rake angle of 45° by default. During the mixing process, both the operational conditions and material properties highly influence the mixing rate and the final mixture property. In a two-bladed cylindrical mixer, Chandratilleke et.al. (Chandratilleke et al., 2010, 2009) studied the effects of a wide range of blade speeds (2-100 rpm), blade rake angle and gap on the local flow structure and the mixing rate. They found that the changes of those factors imposed a significant effect on the bed profile, recirculation zone, force structure, blade torque, and even mixing rate in terms of revolutions. Despite the extensive study on bladed mixer in the past, lots of investigations are still needed because of the complicated geometrical structure of the granulator and the complex phenomena of flow and mixing generated by it.

A number of researchers have pointed out that the lack of qualitative analysis and fundamental understanding of granular flow structure and mixing behaviour makes it difficult to design mixers and control mixing processes. PEPT experiments and DEM simulation are the two most commonly used particle-scale methods that are able to track particle trajectories for determining flow fields and provide in-depth perspectives towards the force structures. The continuum methods recently developed overcome the disadvantages of experiments and the limitation of computational power for large-scale simulations with DEM. The Eulerian finite element method (FEM) based on Mohr-Coulomb elastic-plastic theory is a promising continuum approach to describe the solid-fluid dual behavior and overcome the problem of mesh distortion in the traditional Lagrangian method. Its validation has been testified in a variety of geometries from sandpile to bladed mixers (Zheng and Yu, 2014, 2015a,b; Bai et al., 2017). Recently, a convection mixing model has been established based on the FEM granular flow model and validated in a bladed cylindrical mixer in Chapter 3. The mechanisms of diffusion and segregation have been added on the basic convection equation using finite difference algorithms. The FEM mixing model has been developed and verified in a rotating drum in Chapter 4 and Chapter 5. In this chapter, the FEM based convection-diffusion-segregation mixing model will be applied in a complicated 3D commercial granulator in industry, i.e. the Mipro mixer. The effect of a wide range of operational parameters such as blade speed and rake angle are studied comprehensively. This chapter is organized as follows. Section 6.2 introduces the Eulerian Finite Element Method based on the Mohr-Coulomb elasto-plastic (MCEP) theory. Section 6.2.3 introduces the convection-diffusion-segregation equation in the transient mixing model. The results and discussions on the effects of operational parameters on the mixing and segregation process will be presented in Section 6.3. Finally, Section 6.4 is devoted to summaries and conclusions.

6.2 Theory and numerical simulation method

6.2.1 Governing equations of granular flow

The granular material inside Mipro is treated as a continuum medium since the container's dimension is far larger than the diameter of particles. Similar to other forms of matter, granular dynamics also needs to satisfy the fundamental principles of mass, momentum and energy conservation, given by Mass conservation

$$\frac{\partial \rho}{\partial t} + \nabla \cdot (\rho \boldsymbol{\nu}) = 0$$

Momentum conservation

$$\frac{\partial (\rho \boldsymbol{\nu})}{\partial t} + \nabla \cdot (\rho \boldsymbol{\nu} \bigotimes \boldsymbol{\nu}) = \nabla \cdot \sigma + \rho \boldsymbol{b}$$

Energy conservation

$$\frac{\partial (\rho \epsilon)}{\partial t} + \nabla \cdot (\epsilon \boldsymbol{\nu}) = \boldsymbol{\sigma} : \dot{\boldsymbol{\epsilon}}$$

where ρ refers to the bulk density of granular material, $\boldsymbol{\sigma}$ is Cauchy stress tensor, $\boldsymbol{b}$ is body force, $\boldsymbol{v}$ is velocity vector and ϵ is the internal energy per unit volume. $\dot{\boldsymbol{\epsilon}} = (1/2)(\nabla v + (\nabla v)^T)$represents the strain rate.

The boundary conditions (BC) of no inflow and free outflow are used in this work.

No inflow BC

Material or void can flow into the Eulerian domain through the specified boundary. The normal component of the velocity is set to zero if the velocity is directed inward at the boundary, while the tangential component of the velocity remains unchanged.

Free outflow BC

Material can flow out of the Eulerian domain freely; and the material content and the state of each outflow material are equal to that which presently exists within the element.

6.2.2 Mohr-Coulomb model of granular rheology

In the Mohr-Coulomb elastoplastic model, a linear relation between stress and elastic strain is adopted as:

$$\sigma_{ij} = D^{el}_{ijkl}\epsilon^{el}_{kl} \tag{6.1}$$

where σ_{ij} is the total stress; ϵ^{el}_{kl} is the elastic strain; and D^{el}_{ijkl} is the fourth-order tensor of elasticity.

The yield condition is given by:

$$R_{mc}q - p\tan\varphi - c = 0 \tag{6.2}$$

where

$$R_{mc} \quad = \quad \frac{1}{\sqrt{3}\cos\varphi}\sin(\Theta + \frac{\pi}{3}) + \frac{1}{3}\cos(\Theta + \frac{\pi}{3})\tan\varphi$$

φ is the slope of the Mohr-Coulomb yield surface in the $p - R_{mc}q$ stress plane, which is commonly referred to as the friction angle of the material and can depend on temperature and predefined field variables. $p = -\frac{1}{3}\text{trace}(\sigma_{ij})$ is the first invariant of stress representing the equivalent pressure; $q = \sqrt{\frac{3}{2}S_{ij}S_{ij}}$ is the Mises equivalent stress and S_{ij} is the deviatoric stress; φ and c are the angles of internal friction and and the cohesion of granular material, respectively. Θ is the deviatoric polar angle defined as $\cos(3\Theta) = (r/q)^3$ where $r = (\frac{9}{2}S_{ji}S_{jk}S_{ki})^{\frac{1}{3}}$ is an invariant measure of deviatoric stress. The friction angle, φ, controls the shape of the yield surface in the deviatoric place. The friction angle range is $0^\circ \leq \varphi < 90^\circ$. In the case of $\varphi = 0^\circ$ the Mohr-Coulomb model reduces to the pressure-independent Tresca model with a perfectly hexagonal deviatoric section. In the case of $\varphi = 90^\circ$ the Mohr-Coulomb model reduces to the "tension cutoff" Rankine model with a triangular deviatoric section and $R_{mc} = \infty$.

Granular flow can be well described as flow rules. The flow potential G is chosen to be a hyperbolic function in the meridional stress plane and a smooth elliptic function in the deviatoric stress plane, defined by:

$$G = \sqrt{(\epsilon c \mid_0 \tan\psi)^2 + (R_{mw}q)^2} - p\tan\psi \tag{6.3}$$

and

$$R_{mw} = \frac{4(1-e^2)\cos^2\Theta + (2e-1)^2}{2(1-e^2)\cos\Theta + (2e-1)\sqrt{4(1-e^2)\cos^2\Theta + 5e^2 - 4e}} \times \frac{3-\sin\varphi}{6\cos\varphi} \tag{6.4}$$

where ψ is the dilatancy angle of material, $c|_0$ is the initial cohesion yield stress, ϵ is a parameter that characterizes the eccentricity of the flow potential. e referred to as the deviatoric eccentricity, describing the "out-of-roundedness" of the deviatoric section in terms of the ratio between the shear stress along the extension meridian and the shear stress along the compression meridian, is a function of the internal friction angle φ, given as $e = (3-\sin\varphi)/(3+\sin\varphi)$.

An additive strain rate decomposition is assumed:

$$d\boldsymbol{\varepsilon} = d\boldsymbol{\varepsilon}^{el} + d\boldsymbol{\varepsilon}^{pl},$$

where $d\boldsymbol{\varepsilon}$ is the total strain rate, $d\boldsymbol{\varepsilon}^{el}$ is the elastic strain rate, and $d\boldsymbol{\varepsilon}^{pl}$ is the inelastic (plastic) strain rate.

The constitutive flow rule can be written as:

$$d\boldsymbol{\varepsilon} = \frac{d\boldsymbol{\varepsilon}}{g_m}\frac{\partial G}{\partial \boldsymbol{\sigma}},$$

where g_m can be written as

$$g_m = \frac{1}{c}\boldsymbol{\sigma} : \frac{\partial G}{\partial \boldsymbol{\sigma}}$$

6.2.3 Transient mixing model

General mixing equation

The general scalar transport equation governing the mixing process (Khakhar, 2011) is shown in Eq.6.5, where c is the concentration of granular materials of one kind and v is the corresponding velocity. The left hand side refers to the traditional convection only and the right hand side indicates the diffusion mechanism.

$$\frac{\partial c}{\partial t} + v \cdot \nabla c = \nabla \cdot (\boldsymbol{D}\nabla c) \tag{6.5}$$

The symbol D in front of the gradient operator stands for the diffusivity which can be interpreted as a tensor (Campell, 1997). In our work, for simplicity, we assume it is a scalar. In the dilute region (Fan et al., 2015), the relationship between diffusivity and particle diameter and granular temperature can be expressed as:

$$D \sim d_p\sqrt{T} \tag{6.6}$$

where d_p is the particle diameter and T is the granular temperature. Alternatively, in the dense region of granular material (Hajra and Khakhar, 2005), the linear relationship can be represented as:

$$D = \chi\dot{\gamma}d_p^2 \tag{6.7}$$

where $\dot{\gamma}$ and χ are the local shear rate of material and diffusion coefficient respectively. In Charpter 4, we demonstrate that diffusion can be heterogenous when the mixing model extends to the 3D case. However, for simplicity we assume that D is a homogenous scalar in the 3D Mipro simulation.

For the mixing process, the zero-flux boundary condition at all boundaries is adopted throughout the work as described bellow.

$$\nabla \cdot \boldsymbol{D}\nabla \boldsymbol{c} = 0 \tag{6.8}$$

The size segregation process in this chapter is described by 3D percolation model similar to that in chapter 5. The whole transport equation of small particles including convection, diffusion and percolation can be written as:

$$\frac{\partial c}{\partial t} + v \cdot \nabla c + \frac{\partial}{\partial z}(w_p c) = \nabla \cdot \boldsymbol{D}\nabla c \tag{6.9}$$

where z is the direction of gravity in the mixer geometry and w_p can be written in the following form:

$$w_p \quad = \quad -l_{seg}\dot{\gamma}(1-c_p),$$

, where l_{seg} in the units of length is the percolation length depending on the particle size ratio and particle sizes.

Mixing index

Mixing index characterizes quantitatively the extent of particle mixing, with values between 0 (totally segregated state) and 1 (fully mixed state). Lacey (Zhou et al., 2004) proposed a popular index based on the local sampling variance, which is however mainly suitable for discrete studies. In this continuum study, the intensity of mixing proposed for characterizing the liquid mixing efficiency (Zhendong et al., 2012) is selected as the mixing index, written as

$$M = 1 - \sqrt{\frac{\sigma^2}{\sigma^2_{max}}},$$

,where σ is defined as:

$$\sigma = \sqrt{\frac{1}{N}\sum_{i=1}^{n}(c_i - c_m)^2},$$

N is the total number of sampling points. c_i is the concentration of particle at the sampling point i. $c_m = 0.5$ is the optimal mixing fraction, which also stands for the average concentration of the whole material assembly. σ is the standard deviation of concentration at certain time, and σ_{max} is the maximum standard deviation during the whole mixing process. M equals 0 at the initial stage when particles are completely separated ($\sigma = \sigma_{max}$) and equals 1 at the final homogeneous mixed state ($\sigma = 0$). In our work, the sampling points are taken as the computational grids of FEM meshes, so the value of M may be affected by the mesh density.

Segregation index

The segregation index can be defined in a similar way:

$$I = \sqrt{\frac{\sigma^2}{\sigma_0^2}}, \tag{6.10}$$

,where σ is defined as:

$$\sigma = \sqrt{\frac{1}{N}\sum_{i=1}^{n}(c_i - \bar{c}_t)^2},$$

N is the total number of nodes. c_i is the concentration of particle at the node i. σ_0^2 is the variance of fully-segregated state and σ^2 is the variance of the mixture at time t, where $\sigma_0^2 = c(1-c)$ and c represents the particle number ratio of the target particles to the total particle number in the binary mixture. $\bar{c}_t$ represents the average of c_i at time t. I equals 0 at the initial stage because particles are well mixed at the homogeneous state ($\sigma = 0$) and equals 1 when the particles are completely mixed ideally ($\sigma = \sigma_0$). In our work, the sampling points are collected from the FEM computational grids.

6.2.4 Simulation conditions

The MiPro high shear mixer (Procept, Belgium) considered here consists of a 1900 ml vessel and a three-bladed bevelled impeller with the blade rake angle of 45°. The granular material has the physical properties of Nonparil 200 (250-150 μm) with the density of 0.72 g/mL. The geometry of mixer and mesh condition are shown in Fig.6.1. The container and rotating blades are all modelled as Lagrangian parts (element type R3D4) in FEM. The cohesionless particles, regardless of size and shape, are treated as a continuous Eulerian part (element type EC3D8R). To guarantee accuracy, a high mesh density with mesh size of 0.5 cm (the optimized mesh size in (Bai et al., 2017)) is employed throughout the simulation. More information about the Eulerian FEM technique can be found in (Zheng and Yu, 2014). When simulation starts, the material (260g) is set up in the middle of the vessel with the height of 0.02 m suspending over the impeller and settles down under gravity to cover the bottom of the container, before blades rotate about the shaft driving the material to flow within the Eulerian elements. The simulation usually needs to last for a while until the solid flow becomes steady. The data of various physical quantities are then collected and analysed. The parameters of the drum and the granular material are listed in Table 6.1. Please note that the density used here is the bulk density of particles.

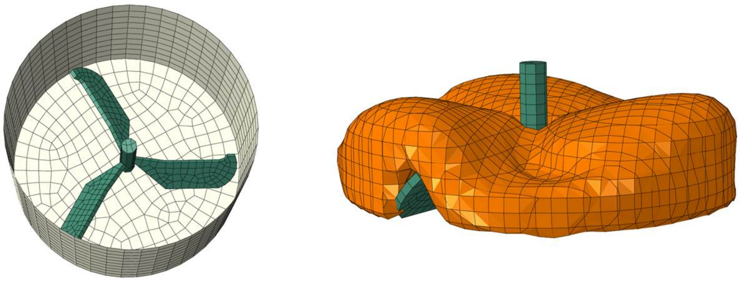

Figure 6.1: The geometry of Mipro mixer and mesh condition.

Parameters	Values	Range of variation
Mixer diameter	0.15 m	-
Bulk height	0.02 m	-
Particle diameter	0.001 m	-
Particle density	432 kg/m^3	-
Poisson's ratio	0.3	-
Young's modulus	1×10^6 Pa	-
Internal friction angle	17°	15° - 30°
Cohesion yield stress	0 Pa	-
Diffusion coefficient	0.1	0.1 - 1
Percolation length	0.1 mm	0.1 mm - 0.25 mm
Mesh size	0.005 m	-
Rotation speed	20 rpm	20 rpm - 300 rpm
Blade angle	45°	45° - 135°

Table 6.1: Physical parameters used in the simulation

6.3 Results and discussion

6.3.1 Comparison of simulation with experiments

Fig.6.2 shows the magnitude, tangential and axial components of velocity profiles at the vessel wall derived from experiment, CFD (Nguyen et al., 2014) and FEM. The values by FEM simulation are calculated by averaging the material velocities in all grids adjacent to the wall at specific vessel heights. In contrast to the over-predicted results from CFD, the velocity components by FEM are much closer to the experiment. The work in (Nguyen et al., 2014) attributed the over prediction to the under-estimated frictional interaction between particles and the coarse approximation of the slip coefficient in the partial slip boundary condition. In Mohr-Coulomb theory, the materials friction is described by the internal friction angle φ which is determined according to the relationship between φ and the sliding friction coefficient in a shear test (Bai et al., 2017; Zheng and Yu, 2015b,a). The only changeable parameter in FEM is the interaction between particles and the vessel wall. In the FEM model, a general contact including tangential behaviour and normal behaviour is used to describe the interaction between different materials. If the contact friction coefficient increases (in this case, μ = 0.5), the curve of velocity profile is much similar to that from experiments. However, discrepancies from the experiment can still be noticeable. This is probably because the constitutive law provided by Mohr-Coulomb elastoplastic model fails to describe the transition state of granular flow, which needs further theoretical development of rheology.

6.3.2 Effects of blade speed

Flow pattern

Fig.6.3 shows the bed profile at different rotating speed (20 rpm, 50 rpm, 100 rpm) in the simulated cylindrical bladed mixer. Three obvious heaps emerge in the vicinity of blades and exhibit different patterns for different speeds. As the shaft speed increases, the altitude of heaps becomes higher and the slope of the heaps turn to be sharper. When ω = 100 rpm, small vacancies appear near the central shaft. This is because more particles travel outward due to the strong centrifugal force and congregate at the outer part of the

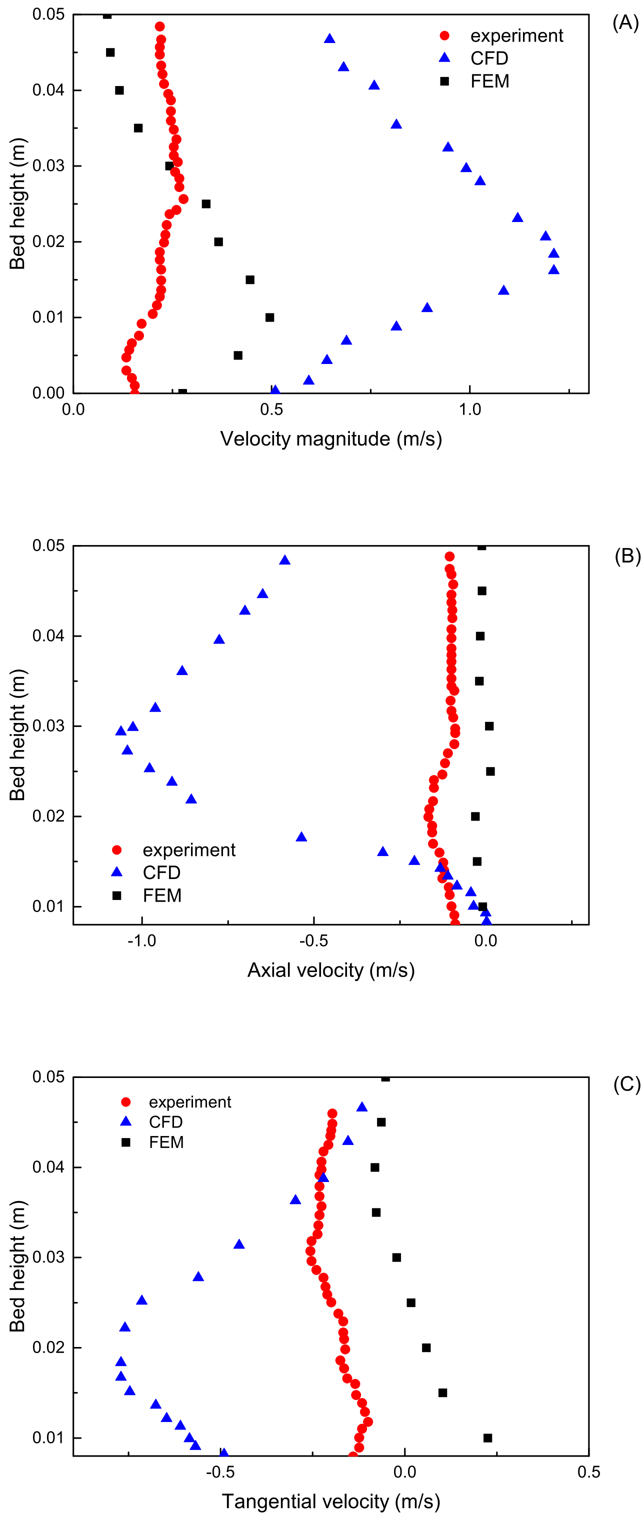

Figure 6.2: Comparison of velocity profiles at the vessel wall. $\omega = 300$ rpm. (A) Velocity magnitude; (B) Axial velocity; (C) Tangential velocity;

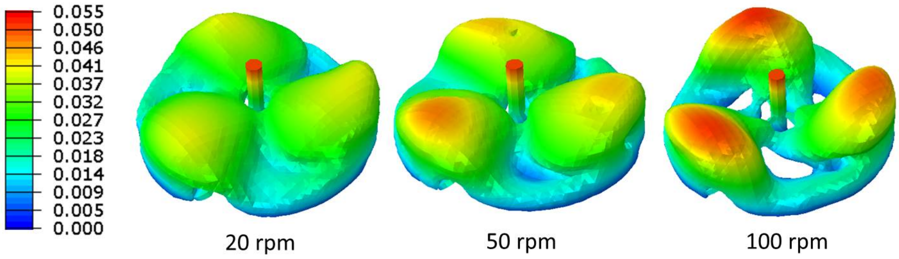

Figure 6.3: Bed profiles obtained by FEM at different rotating speeds. The legend shows the altitude of bed in units of m

blade near the vessel due to the recirculation zone where the minority of particles flow over the blade, moving backwards and forming a vortex of flow field.

Statistical distribution

Fig.6.4, 6.5 show the probability density distribution as a function of magnitude of velocity, radial velocity, tangential velocity, Mises equivalent stress $q = \sqrt{\frac{3}{2}\mathbf{S}:\mathbf{S}}$ and equivalent pressure $p = -\frac{1}{3}\text{trace}(\boldsymbol{\sigma})$ where $\boldsymbol{\sigma}$ and $\mathbf{S}$ are the stress and deviatoric stress tensors respectively. The data is collected when the whole system evolves into a steady state. The data to calculate the probability density function (PDF) can be defined in the following way:

$$f(\beta) = \frac{number \quad of \quad nodes \quad \in [\beta, \beta + \triangle\beta]}{total \quad number \quad of \quad nodes} \times \frac{1}{\triangle\beta} \tag{6.11}$$

, where β is the random variable falling within the small interval $[\beta, \beta + \triangle\beta]$ in the statistical distribution. The interval $\triangle\beta$ is chosen according to the random variable range defined in 6.11. It is observed that as for the velocity distributions, all the three peak values become lower and wider when the rotating speed increases, which suggests the distribution of velocity magnitude gets decentralized and disperse. This can be better explained by the flow bed profile in Fig.6.3. The vacancies in the vicinity of the shaft demonstrate the majority of particles are dynamically mobile and travelling at a faster velocity. Only a small group of particles stay stationary at the bed. The PDF of tangential velocity shifts to the right side as ω becomes larger, which indicates more particles travel in the same direction with the blade rotation. It also indicates the recirculating zone becomes smaller with the increase of the blade speed. Both the PDF of Miese equivalent stress and equivalent pressure show a wider range of force distribution. Most of forces are observed to fall within the range of 0 to 400 pa. Both peaks stay at a small value of forces, which indicates most particles in motion interact through small contact forces with their neighboring particles. The particles with large forces are mainly distributed around the blade because of the impact of blade impelling as Fig.6.6 shows. When ω increases from 20 rpm to 100 rpm, the peak of contact force becomes lower and shifts slightly to the higher force range, implying many particles are propelled by large forces at contact surface. Considering the relationship between Mises and pressure $\mathbf{S} = \boldsymbol{\sigma} + p\mathbf{I}$, it is not surprising to see the similarity of their distributions.

Effect of diffusion on the mixing pattern

Fig.6.7 shows the evolution of mixing process with different diffusion coefficients. The contour value shown in Fig.6.7 represents the concentration of red particles c_r, with $c_r = 1$ for cells full of red particles and $c_r = 0$ for cells full of blue particles. Naturally, $c_r = 0.5$ means a complete mixing state. The particles of the same material properties but different colours are arranged side by side at the initial stage. As the blades rotate, the two kinds of particles are blended and mixed due to the convection diffusion mechanism in Eq.6.5. It can be observed that at first particles are transferred to different locations via convection and the diffusion effect is not yet significant since $\chi = 0.1$ and $\chi = 0.5$ are almost identical at t = 1s. As the process continues, the two cases have a similar pattern such as the shape of curves and contour but different distribution of C. Both of the colour become lighter under a higher diffusion effect ($\chi = 0.5$) at t = 3s, 5s, which indicates that the larger diffusivity results in faster particle mixing.

Effects of speed on the mixing index

Fig.6.8 shows the effect of blade speed on the mixing evolution of index. If the mixing index is expressed as a function of the number of blade revolutions, it reaches the fully mixed state earlier at slow blade speeds than at fast blade speeds. With different diffusion coefficients, the evolution of mixing index exhibits different trends. With a lower diffusion coefficient ($\chi = 0.1$), the mixing index for $\omega = 50$ rpm evolves more slowly than $\omega = 20$ rpm at the first 2 revs. The two indexes collapse into a single curve after 3 revs. When diffusion is weak, mixing occurs by transport of material bulk in the recirculation zone. The similarity of pressure distribution at a lower rotating speed in Fig.6.5 indicates the yield condition in Eq.6.2 is not changed. As a result, the volume of granular chunk for

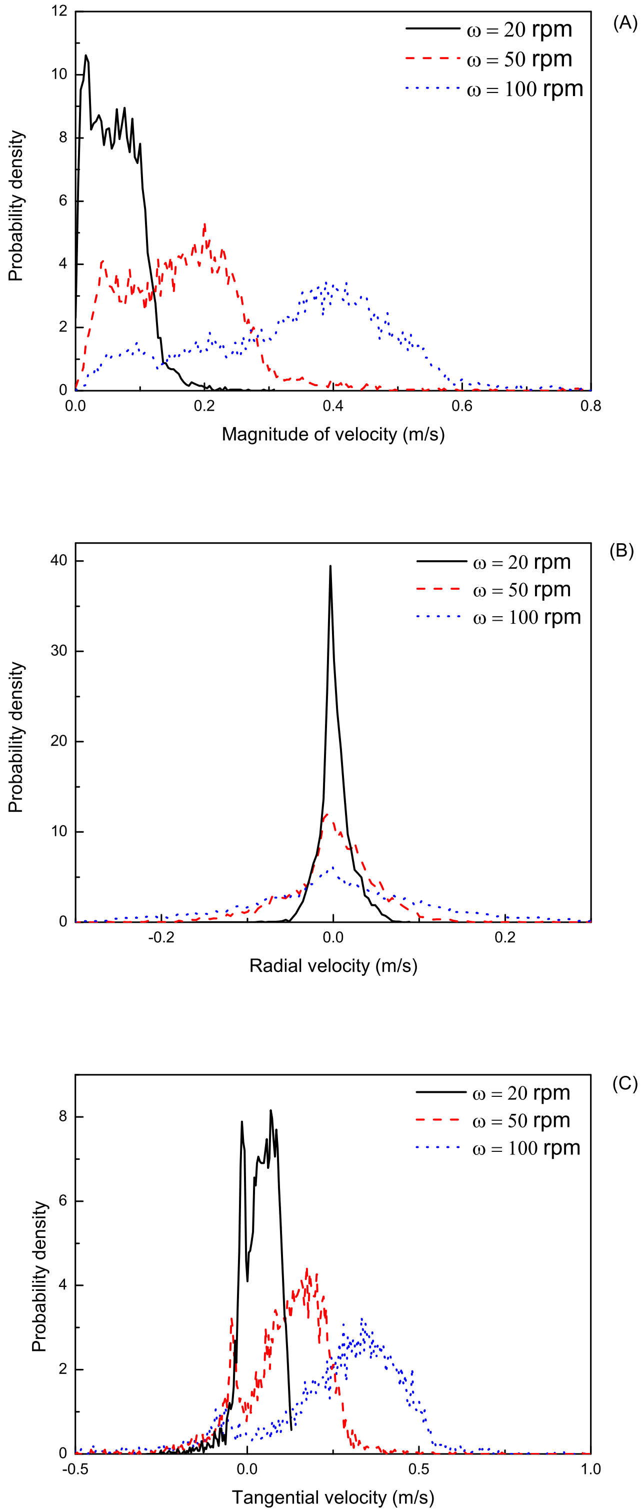

Figure 6.4: The statistical velocity distribution of probability density with different rotating speeds. (A) Magnitude of velocity; (B) Radial velocity; (C) Tangential velocity.

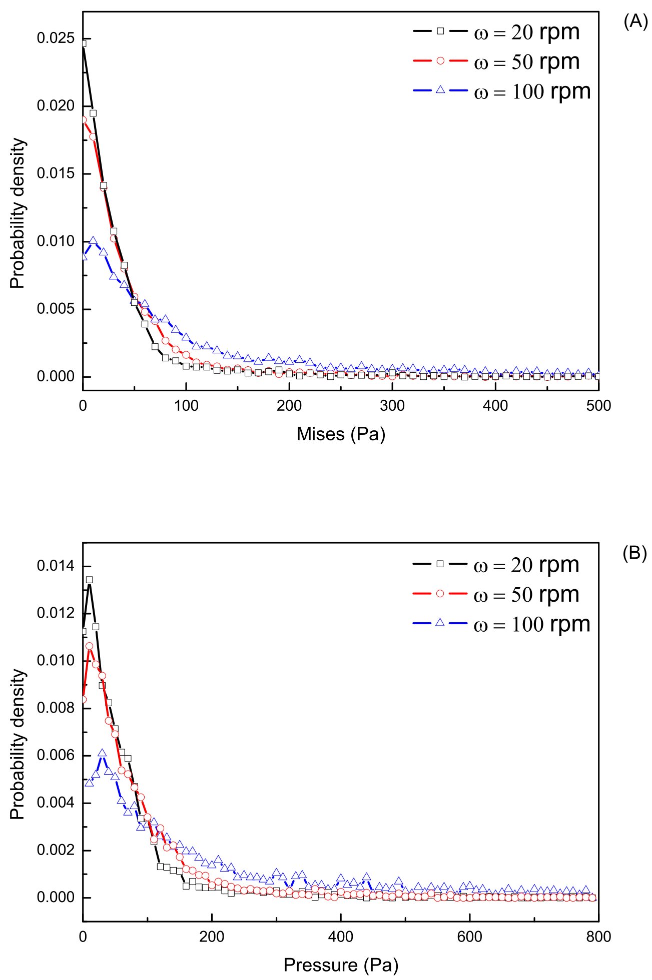

Figure 6.5: The statistical distribution of stress with different rotating speeds. (A) Mises; (B) Pressure.

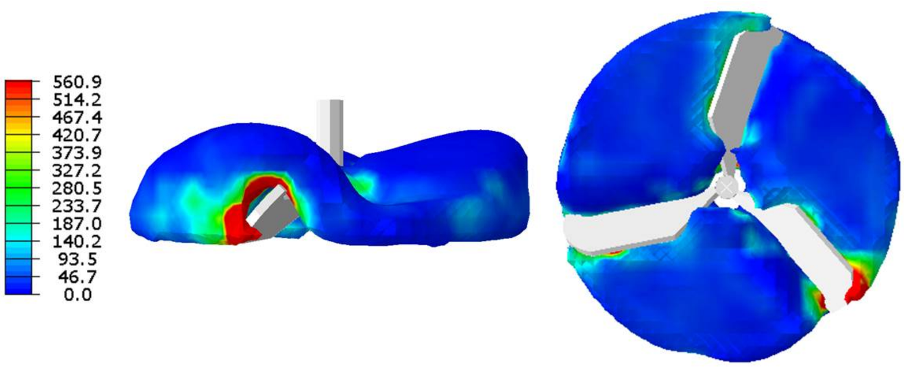

Figure 6.6: Mises shear stress profiles obtained by FEM. The legend shows the stress in units of N

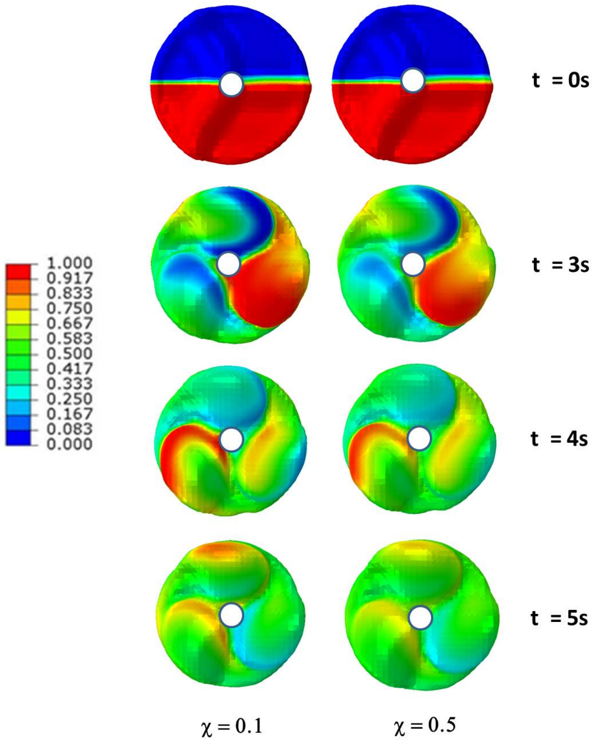

Figure 6.7: Mixing pattern evolution with different diffusion coefficients. ω = 20 rpm.

transport stays stable. As most mixing happens within the chunk, the mixing rate is actually a function of the anular displacement the blade passes rather than time. When χ increases to 0.5, the trend of mixing index evolution keeps the same as that of small χ at the first 2 revs. However, the mixing index for ω = 50 rpm evolves more quickly than ω = 20 rpm after 3 revs and reaches the steady mixed state first. The crossover of the two indexes can be clearly seen in Fig.6.8. It indicates that among the three cases, the mixing process takes the greatest advantage of diffusion effect at the rotating speed of ω = 50 rpm.

6.3.3 Effects of blade rake angle

The blade rake angle α is defined as the angle between the front blade surface and horizontal vessel bottom (shown in Fig.6.9). Three rake angles (45°, 90°, 135°) are studied in this section.

Statistical distribution

Figs.6.10 and 6.11 show the probability density distribution of velocity magnitude, radial velocity, tangential velocity, Mises equivalent stress, and equivalent pressure with different

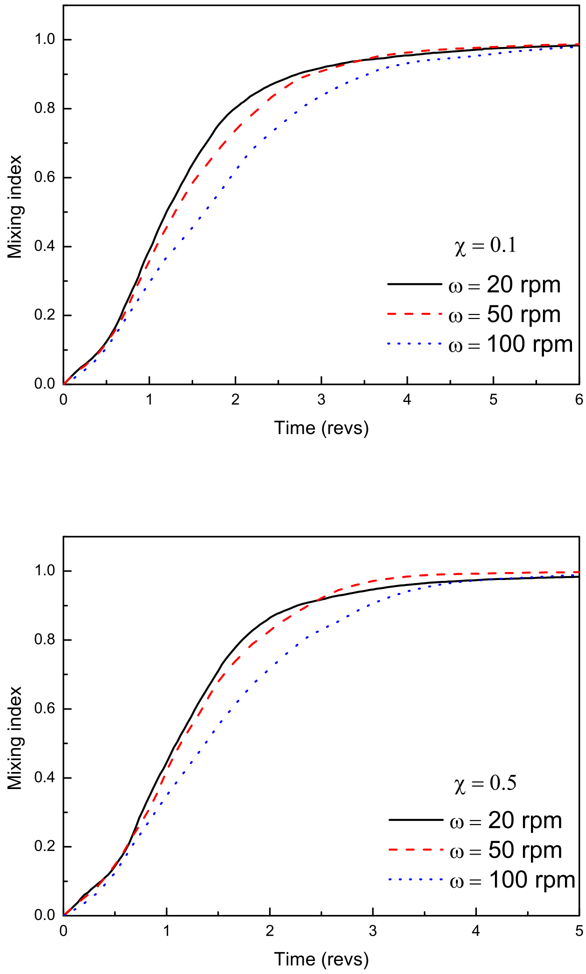

Figure 6.8: Mixing index evolution with different diffusion coefficients.

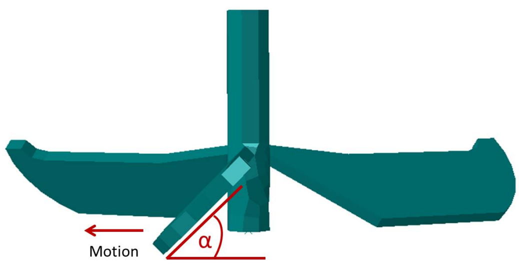

Figure 6.9: Definition of blade rake angle in Mipro Mixer

blade rake angles ($\alpha = 45°$, $90°$, $135°$) at the rotating speed of $\omega = 50$ rpm. The curves of speed distribution for $\alpha = 45°$, $90°$ are almost identical. In case of $\alpha = 90°$, there is a small group of particles travelling at a faster speed. This is probably because the blade height of $\alpha = 90°$ is higher than the other two, which causes a slightly higher altitude of recirculating zone, thus particles flow down from a high plateau and gain a faster speed. Generally, the difference of speed distribution between the three cases is small, suggesting that the granular flow field is almost independent of blade rake angle. However, as for each component of the velocity, the trends can be different. The PDFs of radial velocity for $\alpha = 90°$, $135°$ are similar with a wider distribution than that of $\alpha = 45°$. It demonstrates that particles tend to be dispersed in different directions when the blade rake angle becomes blunt, leading to a lager recirculating zone. The PDFs of tangential velocity for $\alpha = 45°$, $90°$ are much similar while in case of $\alpha = 135°$, many particles move in an opposite direction to the blade rotation. The flow field is complex when the blade angle is close to $90°$ because of the reduced areas above the bottom of container and underneath the blades. In this area, particles are squeezed harshly and confined with little freedom of motion. The contact forces in this regime are therefore intense, as further illustrated in Fig.6.12.

When the blade rake angle is small ($\alpha = 45°$, $90°$), the force statistical distributions of Mises and pressure are quite similar. The peak of probability density curve is very high and occurs at small force, indicating that the interaction forces between particles are mostly small. When the blade rake angle increases to the obtuse angle, the curve shifts to a higher force range, indicating slightly larger inter-particle forces between most particles. This can be better explained by the dynamics of flow shown in Fig.6.12. When $\alpha = 45°$, the majority of particles move in the same direction of the blade, creating a small heap in front of the blade. When $\alpha = 135°$, the particles beneath obtuse blade are trapped and hence form a recirculation zone, characterised by the vortex flow field in front of the blade. The volume of this zone is larger than that in the case of $\alpha = 45°$. The bulk imparts a higher stress density to the blade as shown in Fig.6.12, in which the areas with Mises over 1000 Pa is much larger for $\alpha = 135°$.

Fig.6.13 shows the evolution of the applied torque on the reference point of shaft. The torque experiences large oscillations for the first several seconds before reaching a relatively stable value. Although the blade with the angle of $135°$ receives larger forces, the torque variations and tendencies for both $\alpha = 45°$ and $\alpha = 135°$ almost overlap. This is because the torque depends not only on the magnitude of the contact forces but also on the distances from the shaft axis to the granular material contact points on the blade. For $\alpha = 90°$, the large blade height causes a great number of particles within higher forces congregating near the forepart of the blade, which increases the number of torques in higher values for each material grid.

Mixing evolution

Fig.6.14 shows the effect of blade rake angle the mixing index evolution. When the diffusion coefficient is low ($\chi = 0.1$), the inclined blade ($\alpha = 45°, 135°$) gives a slower mixing rate than that of vertical blade ($\alpha = 90°$). By contrast, when the diffusion coefficient is higher ($\chi = 0.5$), the mixing indexes almost collapse into a single curve, which suggests that the mixing index is independent of blade rake angle when diffusion plays a dominant role in the mixing process. When the value of χ is small, which indicates the effect of convection is dominant, the vertical blade with the angle of 90° gives a strong recirculating flow in the vicinity of blades. It leads to a faster mixing process than other blade angles ($\alpha = 45°, 135°$). When the value of χ is higher, diffusion affects the mixing process very much. As a result, in all three cases ($\alpha = 45°, 90°, 135°$), all the mixing rates increases with χ. The mixing rates for $\alpha = 45°, 135°$ grow faster than that for $\alpha = 90°$. This is probably because in the mixing process of $\alpha = 45°, 135°$, convection is weaker and diffusion is more important. In those areas where $\alpha = 90°$ and convection is strong, the effect of diffusion may be overwhelmed by convection and becomes less effective.

6.3.4 Effects of blade gap on the mixing process

The blade gap is another factor that can influence the mixing rate in the bladed mixer. Some research on this issue has been done in two-bladed mixer by (Chandratilleke et al., 2009). In this section, we yield a similar conclusion in the Mipro mixer. As Fig.6.15 shows, when the gap increases (from g = 0 R to g = 0.1 R. R is the radius of the vessel), the effect on the initial rate of mixing is not noticeable at first, but it can finally reduce the degree of mixing. Increasing the gap to g = 0.2 R changes the mixing rate heavily, but the final mixing uniformity changes little in comparison with the case of g = 0.1 R. The mixing pattern in Fig.6.16 illustrates that at t = 0.3 s, most particles above the blade are well

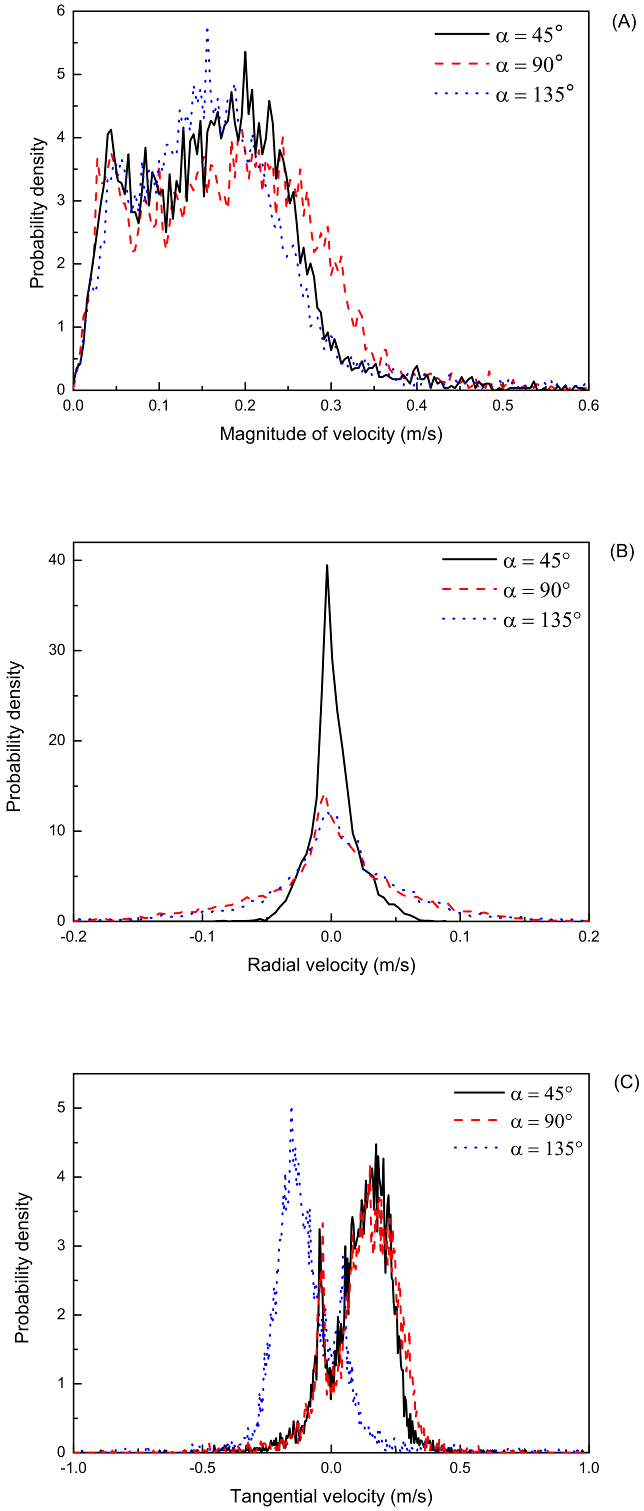

Figure 6.10: Mixing index evolution with different diffusion coefficients. $\omega = 50$ rpm. (A) Magnitude of velocity; (B) Radial velocity; (C) Tangential velocity.

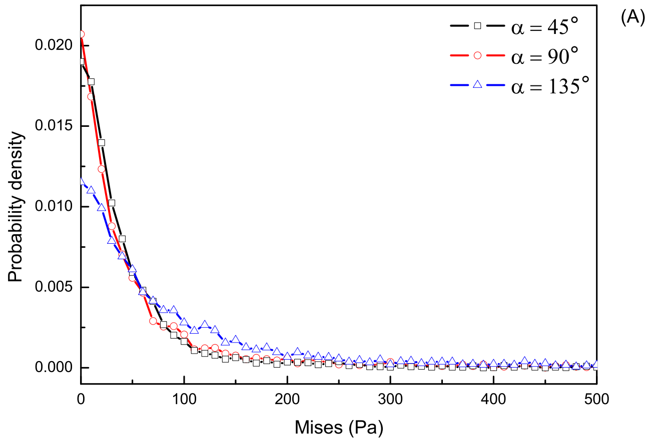

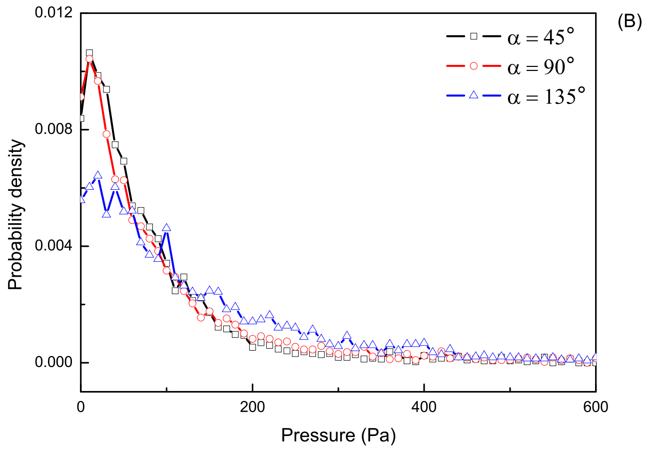

Figure 6.11: Mixing index evolution with different diffusion coefficients. $\omega = 50$ rpm. (A) Mises; (B) Pressure.

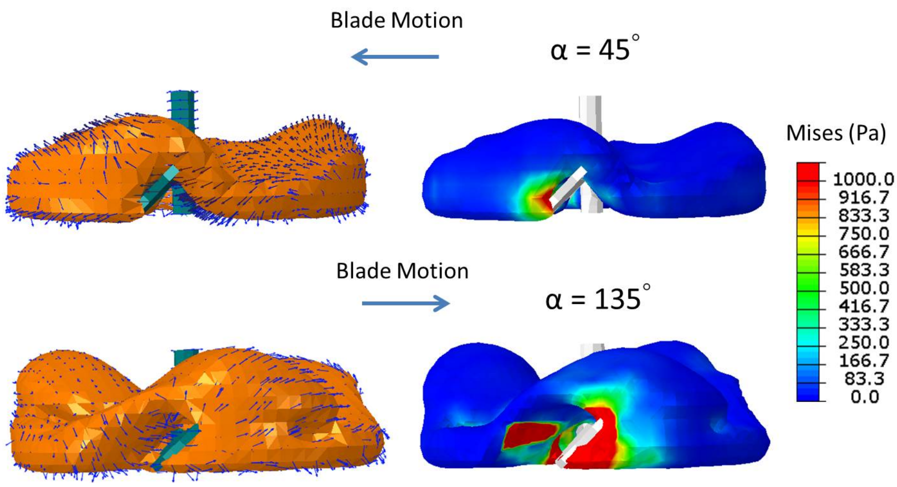

Figure 6.12: Granular flow and forces on the blade.

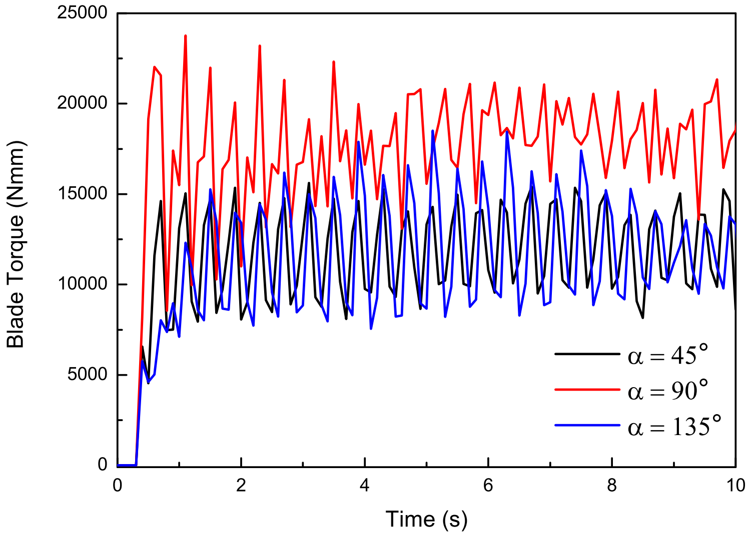

Figure 6.13: Evolution of the total torque acting on the blades for different blade rake angles. $\omega = 50$ rpm.

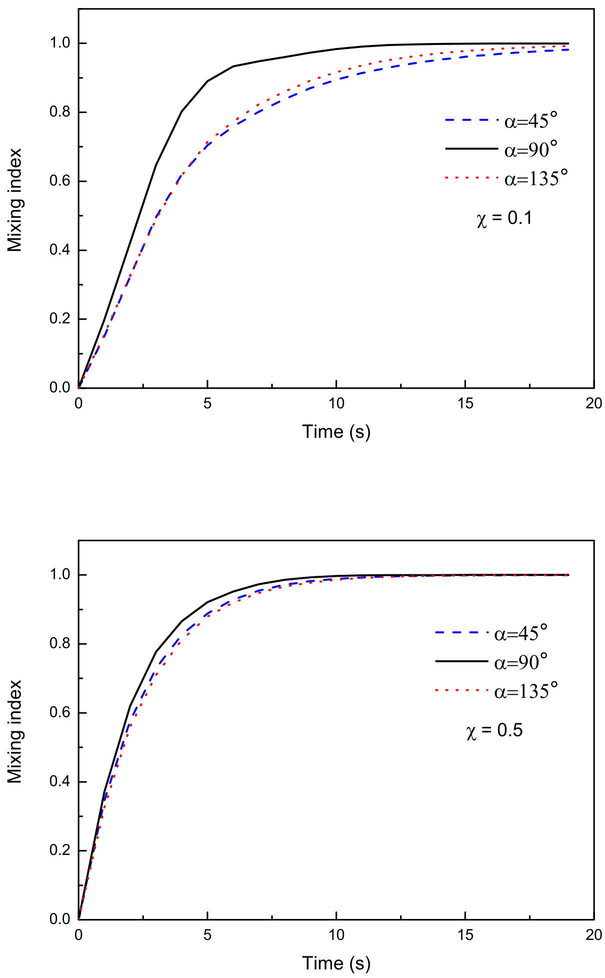

Figure 6.14: Evolution of mixing index with different diffusion coefficients. $\omega = 50$ rpm.

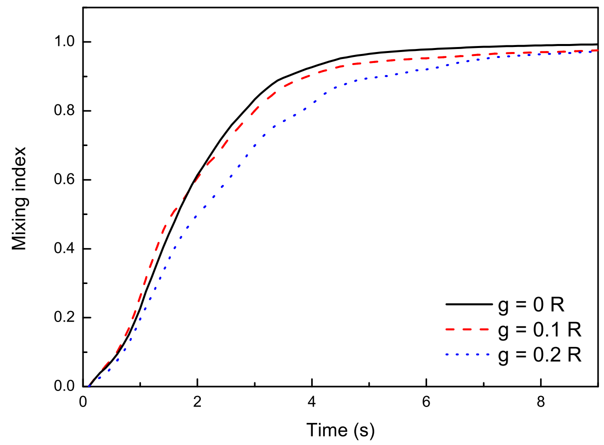

Figure 6.15: Mixing index evolution with different blade gaps. ω = 50 rpm, χ = 0.05, α = 90°.

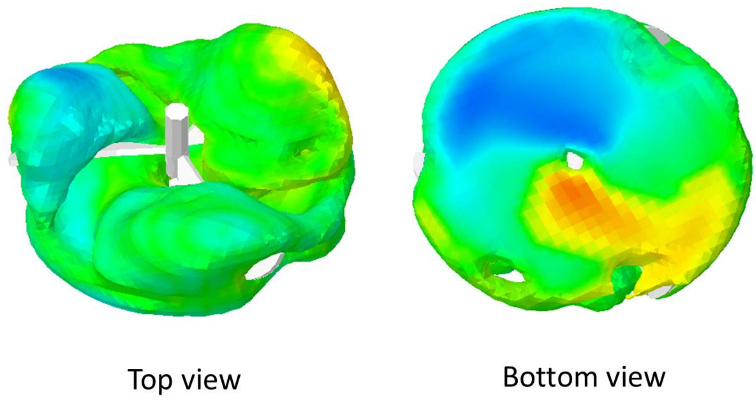

Figure 6.16: Mixing pattern at t = 0.3 s. g = 0.2 R, ω = 50 rpm, χ = 0.05.

mixed due to the intense convection effect there. However, some particles under the blade are confined at the bottom and cannot move up into the recirculation zone. They can only get mixed by the Taylor shear mixing (Bridgwater, 2012) which could last a longer period. So the lower mixing degree at the bottom slows down the overall mixing rate.

6.3.5 Size segregation with the 3D percolation model

The size segregation phenomenon in a bladed mixer has been studied by (Zhou et al., 2003) using DEM. It is found that large particles are mainly distributed in the top and outer regions due to the upward buoyancy forces, and small particles usually stay in the inner and bottom region. In this section, the 3D FEM percolation model is used to study the size segregation in the Mipro mixer.

Fig.6.17 shows the distribution of particle concentration in the simulated Mipro mixer. It is observed from both top view and cross-section view that the large particles pop up to the top and outer regions, while small particles penetrate downward to the bottom and are enclosed large-sized particles. The bottom view illustrates the percolation of small particles first occurs around the blades where the shear rate is high. With the rotation of blades, at 1 rev, the small particles form a circle along the vessel circumference before more small particles settle at the centre of bottom at 3 revs. This observation is similar to the results given by DEM. Finally they end up settling at the bottom of the mixer. Fig.6.18 shows the evolution of segregation index with four different percolation lengths. It is sensible that large percolation length leads to a higher rate of segregation which is similar to the segregation happening in the 2D rotating drum. Note that the segregation index may not be linearly dependent on the percolation length because the segregation of $l_{seg} = 0.1\ mm$ is apparently much slower than the other three cases. Fig.6.19 shows the evolution of segregation index at different blade rotating speeds. It is reasonable that higher blade speeds result in a higher segregation rate when the segregation rate is evaluated in terms of time rather than revolutions. This is due to the higher shear rate in the vicinity of blades, which is caused by a higher density of shear forces brought by the strong blade rotation impact. Differing from the segregation rate, the final degree of segregation is not much subject to the rotating speed. When the segregation index is plotted against the number of revolutions, the three curves show marginal difference and are independent of blade speed.

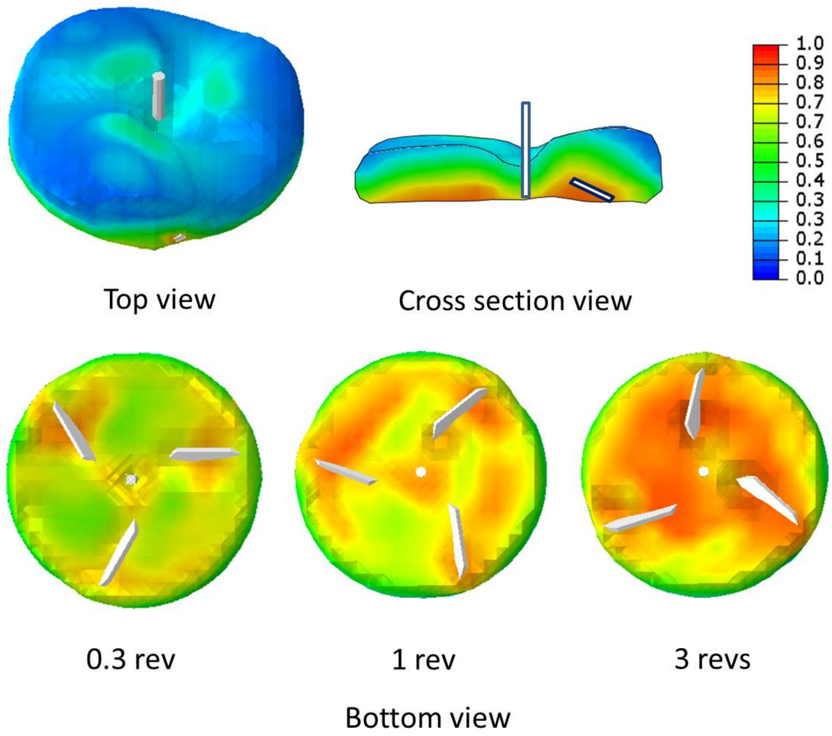

Figure 6.17: Segregation pattern with 3D percolation model. The contour shows the concentration of small-sized particles. $\omega = 1$ rad/s, $\chi = 0.1$, $l_{seg} = 0.25$ mm

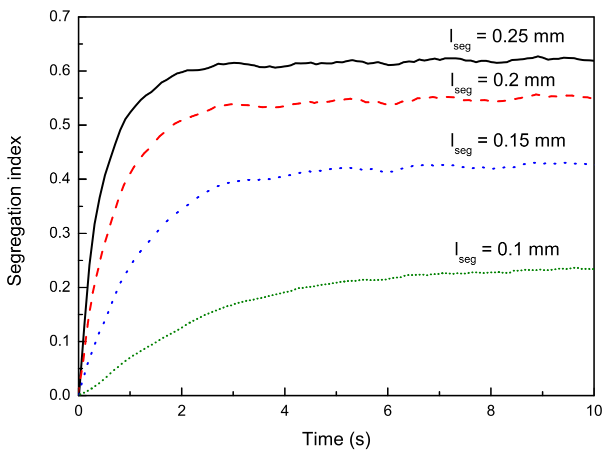

Figure 6.18: Segregation index evolution with different segregation lengths. $\omega = 1$ rad/s, $\chi = 0.1$.

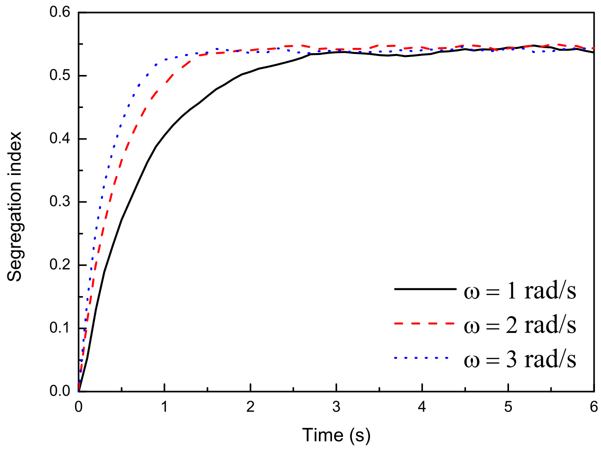

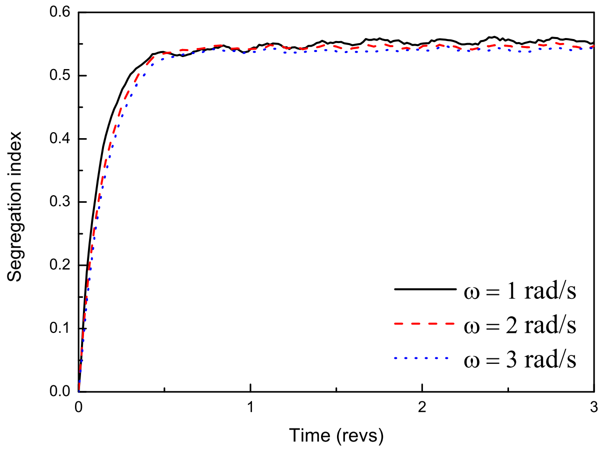

Figure 6.19: Segregation index evolution with different rotating speed. l_{seg} = 0.2 mm, χ = 0.1.

6.4 Conclusions

The 3D FEM-based convection-diffusion-segregation model of granular mixing is used to investigate the mixing efficiency of a Mipro mixer. The velocity profiles obtained by FEM is firstly validated by comparing with that of experiment. The effects of various operational parameters, such as blade speed and rake angle on the mixing process are studied, with attention to the statistical distributions of velocities and stresses as well as the mixing index evolution. The segregation in this mixer is considered by using a percolation model. Several conclusions can be drawn from this chapter:

- The FEM result of velocity profile at the circumference of vessel is closer to experiments than that from CFD. However, The difference between numerical and experimental results has not been completely overcome. Probably new rheology should be introduced and added in the current Mohr-Coulomb model to make it quantitatively agreed with experiments in the future study.

- Statistical distributions of velocity and stress show that as the blade speed increases, more particles become mobile and dynamic, travelling in the same direction of blade rotation at a faster speed. The recirculation zone breaks down as the uni-direction movement is dominant among most particles, which provides a good explanation to the counter-intuitive slow mixing rate as a function of blade revolutions.

- The speed distribution is not sensitive to blade rake angle, but it changes the distribution of radial and tangential velocity. When the blade angle becomes obtuse, more particles can be easily transferred in multiple directions and the flow field becomes more complicated in the area under the blade where the force density is higher, which could impose damage to the blade.

- In the Mipro, small particles tend to be separated and congregate at the centre of vessel bottom. Increasing the blade speed can increase the segregation rate but the degree of segregation remains the same. However, when the segregation rate is evaluated in term of the revolution number, it is hardly influenced by the rotating speed.

6.5 Nomenclature

ϱ	bulk density of granular material [kg/m^3]
E	Young's modulus [Pa]
ν	Poisson's ratio [-]
φ	internal friction angle [degree]
c_y	shear cohesion [Pa]
c	volume fraction [-]
μ	Coulomb friction between granular material and drum wall [-]
M	mixing index [-]

σ	standard deviation of concentration [-]
D	diffusivity
R	radius of drum
g	blade gap
α	blade rake angle
ω	blade speed
$\dot{\gamma}$	shear rate
d_p	diameter of particles
χ	diffusivity coefficient
l_{seg}	segregation length
I	segregation index

Chapter 7

Conclusion and future work

The granular flow and mixing processes have been investigated at the continuum level. A FEM-based mixing model has been developed and verified against DEM results and experiments in rotating drums and bladed mixers. The chapters of the thesis are organised and sequenced by the mixing mechanisms: convection, diffusion and segregation. The first three chapters are devoted to the three mechanisms individually and the final chapter focuses on the application of the developed mixing model in a commercial mixer Mipro. The conclusions can be drawn and classified in the following three categories:

7.1 Convection

The convection of particles is highly dependant on granular flow. The flow model in FEM is based on the Mohr-Coulomb elastic-plastic theory which is able to describe the solid-liquid dual behaviour of granular material. The applicability of flow model is verified in a bladed mixers (CBM). The main conclusions can be made as follows:

- The FEM modelling can reproduce a series of main features of complex granular flow such as the counter-wise recirculation flow in front of blades in CBM, which contributes to a higher mixing rate, and more statistically scattered velocity fields. Those simulation results agree with previous DEM study both qualitatively and quantitatively. The distribution of velocity fields can also agree with the analytical results in some special condition when granular friction is extremely high (φ =89°) and particle-wall interaction is minor (μ = 0.05). As for the mixing, the curve of mixing index as a function of time generated by FEM can qualitatively agree with that from DEM. This method may help overcome the scale-up issues prevalent in bulk solid handling industries, owing to its high computational efficiency.

- Material properties such as internal friction angle and wall friction significantly influence the performance of the mixer. Different material parameters generate completely different flow behaviours and mixing efficiency. A material with a large internal friction angle moves in the system more like a rigid body and hence is more difficult to mix. Wall friction, on the other hand, can prevent such rigid body motion and promote particle mixing. It is therefore suggested that rough walls and flowable materials are optimal choices for mixing in industrial applications.

- In Mipro mixer, the FEM results of velocity are closer to experiments than that from CFD. However, difference between FEM and experiment has not been completely eliminated. New rheology may be introduced to make FEM simulation better agree with experiments in the future. A wide range of operational parameters including blade speeds, blade rake angles are investigated. Statistical distributions of velocity and stress show that with the increase of blade speed, more particles become mobile and dynamic, travelling in the same direction of blade rotation with a faster speed. The recirculation zone breaks down as the uni-direction movement is dominant among most particles, which provides a good explanation to the counter-intuitive decrease in mixing rate per revolution number as blade speed increases. The resultant velocity is not much sensitive to the blade rake angle, but the components of radial velocity and tangential velocity are. For obtuse blade angles, particles tend to be transferred in multiple directions, and the flow field becomes more complicated in the areas under the blade where contact forces are more intense, and probably cause damage to the blades.

7.2 Diffusion

Although the convection dominates the blending in a complex mixer, some challenges exist in this model. Particle diffusion must be considered to give a more reasonable prediction. In order to solve the problem, the convection model is extended to account for diffusion mechanism, using a second order differential equation term $D\nabla^2 c$ and an operator splitting method. The model is validated in 1D Gaussian pulse diffusion, 2D shear flow, and rolling flow regime in a 3D rotating drum, against the results of mixing patterns and indexes obtained previously DEM. The following conclusions can be drawn from this study:

- The modelling results are consistent with the analytical solution in 1D and 2D Gaussian pulse diffusion cases. The developed method is independent of time steps and mesh sizes given that the mesh size is below certain threshold value.
- The interface between two materials is blurred when diffusion is applied to the convection model, resulting that materials penetrate to each other. The obtained mixing index can match that from DEM when the value of χ as a fitting parameter is chosen properly. The FEM mixing index is independent of mesh sizes when the mesh size is less than $1/3L_d$, where L_d is the diffusion length.
- Diffusion has a positive influence on the mixing process, especially in certain range of parameters. When the diffusion coefficient increases, the effects of filling levels and internal friction angles on the mixing process are more obvious. In Mipro mixer, when diffusion comes into effect, the mixing index at $\omega = 50$ rpm shows significant increase above that at $\omega = 20$ rpm within just 2.5 revs. This represents the most effective and optimised mixing condition among different blade speeds. The difference of mixing indexes for different blade rake angles narrows when χ increases. Different blade rake angles cause different convection flow fields, but the effects can be weakened when diffusion plays a role.
- The 2D FEM mixing model can be extended and used to study the 3D axial mixing process. The axial diffusivity is much smaller than the radial diffusivity, which is confirmed by comparing results with DEM. Because the shear rate along the axial direction is almost negligible, it takes more time to disperse particles along the axial direction than in the radial direction.

7.3 Segregation

The attention is now turned to the mixing of materials with different properties. Segregation is the most salient feature and controversial issue in research of particle mixing. In this thesis, the scope was confined to mixing of particles with different sizes. Two theories: percolation and spinodal decomposition described by Cahn-Hilliard equation were incorporated into the FEM model. Both 2D radial segregation and 3D axial segregation in a rotating drum were reproduced by either percolation model or Cahn-Hilliard equation under certain conditions. The effects of percolation length and diffusion coefficient on the segregation rate and segregation index degree are explored. The following conclusions can be drawn:

- The pattern of radial segregation (core formation) produced by the percolation model bears a high level of resemblance with the DEM results. If the percolation length is adjustable, the segregation index of FEM is able to match that of DEM. The percolation length determines the segregation rate while the diffusion coefficient largely influences the final segregation degree.

- The axial segregation in a 3D drum can be only produced qualitatively by the percolation model. Three critical factors, namely radial segregation, wall interaction, and different particle repose angles, contribute to the formation of alternative stripes of small-sized and big-sized particles. However, the number and width of stripes still show a quantitative discrepancy from the experiment results.

- The CH segregation model generates a more reasonable surface strips profile. However, undesired patterns of stripe by spinodal decomposition are noticeable at the vertical cross-sections of granular bulk.

- The 3D size segregation in a bladed mixer is studied by the percolation model. It reproduced the scenario that large particles go upward and get together at the top and outer area of the granular bulk, while small particles stay inside and at the bottom.

7.4 Future work

In terms of the flow dynamics, the FEM model also warrants further developments to account for the various unconventional behaviours of granular materials, including the effects of microscopic grain size, the rate-dependent internal friction, the non-coaxiality of stress and deformation rate, hardening/softening and dilatancy as well as many possible pressure and density effects. The known shear banding behaviour is also neglected due to the lack of a microscopic length in the present model. These aspects are important for improving the quantitative accuracy of the FEM approach and require further studies in future.

The general diffusion mechanism in form of $D\nabla^2 c$ was introduced and used in the current FEM mixing model. The diffusivity itself can vary in different geometric conditions. In the dilute gas region, diffusivity is related to the particle diameter and granular temperature with the relation $D \sim dT^{1/2}$. In the dense region, diffusivity can also be shear rate independent (Fan et al., 2015). More broadly, in some cases such as a long drum mixer granular mixing can exhibit a anomalous diffusive behaviour like sub-diffusion or super-diffusion, namely, indicating the mean squared displacement of particles follows a power law in time with exponent more or less than unity (Khan and Morris, 2005; Christov and Stone, 2012). Considering those complicated mathematical terms of diffusion and diffusivity in the FEM model is an intriguing area of further research.

In the chapter of segregation, it is demonstrated that the axial band formation has not been well explained either by percolation or CH equation. In my view, a new segregation mechanism along the axis should be introduced to the current model while keeping unchanged the percolation responsible for radial segregation. The shear-induced segregation mechanism is a promising candidate model which has been established based on the mixture theory (Gray and Thornton, 2005; Gray and Chugunov, 2006) and developed by (Fan and Hill, 2011a,b) in a vertical shear cell. It is interesting to build a segregation model with combined two directional (radial and axial) segregation mechanisms to further obtain deep understanding of the segregation phenomenon.

References

Ai, J., Chen, J.-F. and Ooi, J. Y. (2013). Finite element simulation of the pressure dip in sandpiles, *International Journal of Solids and Structures* **50**(6): 981–995.

Aranson, I. and Tsimring, L. (2006). Patterns and collective behavior in granular media: Theoretical concepts, *Reviews of Modern Physics* **78**(2): 641–692.

Aranson, I., Tsimring, L. and Vinokur, V. (1999). Continuum theory of axial segregation in a long rotating drum, *Physical Review E* **60**(2): 1975.

Bai, L., Zheng, Q. J. and Yu, A. B. (2017). FEM simulation of particle flow and convective mixing in a cylindrical bladed mixer, *Powder Technology* **313**: 175–183.

Bouzid, M., Trulsson, M., Claudin, P., Clment, E. and Andreotti, B. (2013). Nonlocal rheology of granular flows across yield conditions, *Physical Review Letters* **111**(23).

Bridgwater, J. (2012). Mixing of powders and granular materials by mechanical meansa perspective, *Particuology* **10**(4): 397–427.

Campell, C. S. (1997). Self-diffusion in granular shear flow, *J. Fluid Mech.* **348**: 85–101.

Cantelaube, F. and Bideau, D. (1995). Radial segregation in a 2d drum: an experimental analysis, *EPL (Europhysics Letters)* **30**(3): 133.

Chakraborty, S., Nott, P. R. and Prakash, J. R. (2000). Analysis of radial segregation of granular mixtures in a rotating drum, *The European Physical Journal E: Soft Matter and Biological Physics* **1**(4): 265–273.

Chandratilleke, G. R., Yu, A. B. and Bridgwater, J. (2012). A DEM study of the mixing of particles induced by a flat blade, *Chemical Engineering Science* **79**: 54–74.

Chandratilleke, G. R., Yu, A. B., Stewart, R. L. and Bridgwater, J. (2009). Effects of blade rake angle and gap on particle mixing in a cylindrical mixer, *Powder Technology* **193**(3): 303–311.

Chandratilleke, G. R., Zhou, Y. C., Yu, A. B. and Bridgwater, J. (2010). Effect of blade speed on granular flow and mixing in a cylindrical mixer, *Industrial and Engineering Chemistry Research* **49**(11): 5467–5478.

Chandratilleke, R., Yu, A. B., Bridgwater, J. and Shinohara, K. (2014). Flow and mixing of cohesive particles in a vertical bladed mixer, *Industrial and Engineering Chemistry Research* **53**(10): 4119–4130.

Chen, P., Ottino, J. M. and Lueptow, R. M. (2010). Onset mechanism for granular axial band formation in rotating tumblers, *Phys Rev Lett* **104**(18): 188002.

Chen, P., Ottino, J. M. and Lueptow, R. M. (2011). Granular axial band formation in rotating tumblers: a discrete element method study, *New Journal of Physics* **13**(5): 055021.

Christov, I. C., Lueptow, R. M. and Ottino, J. M. (2011). Stretching and folding versus cutting and shuffling: An illustrated perspective on mixing and deformations of continua, *American Journal of Physics* **79**(4): 359.

Christov, I. C. and Stone, H. A. (2012). Resolving a paradox of anomalous scalings in the diffusion of granular materials, *Proceedings of the National Academy of Sciences* **109**(40): 16012–16017.

Ciamarra, M. P., Coniglio, A. and Nicodemi, M. (2006). Dynamically induced effective interaction in periodically driven granular mixtures, *Phys Rev Lett* **97**(3): 038001.

Cleary, P. W., Metcalfe, G. and Liffman, K. (1998). How well do discrete element granular flow models capture the essentials of mixing processes?, *Applied Mathematical Modelling* **22**(12): 995–1008.

Darelius, A., Rasmuson, A., Niklasson Bjrn, I. and Folestad, S. (2007). Lda measurements of near wall powder velocities in a high shear mixer, *Chemical Engineering Science* **62**(21): 5770–5776.

Darelius, A., Rasmuson, A., van Wachem, B., Bjorn, I. N. and Folestad, S. (2008a). CFD simulation of the high shear mixing process using kinetic theory of granular flow and frictional stress models, *Chemical Engineering Science* **63**(8): 2188–2197.

Darelius, A., Rasmuson, A., van Wachem, B., Bjorn, I. N. and Folestad, S. (2008b). CFD simulation of the high shear mixing process using kinetic theory of granular flow and frictional stress models, *Chemical Engineering Science* **63**(8): 2188–2197.

Das, S. K. and Puri, S. (2003). Pattern formation in the inhomogeneous cooling state of granular fluids, *EPL (Europhysics Letters)* **61**(6): 749.

Ding, J. and Gidaspow, D. (1990). A bubbling fluidization model using kinetic theory of granular flow, *AIChE journal* **36**(4): 523–538.

Dury, C. M. and Ristow, G. H. (1997). Radial segregation in a two-dimensional rotating drum, *Journal de Physique I* **7**(5): 737–745.

Fan, Y. and Hill, K. M. (2011a). Phase transitions in shear-induced segregation of granular materials, *Physical Review Letters* **106**(21).

Fan, Y. and Hill, K. M. (2011b). Theory for shear-induced segregation of dense granular mixtures, *New Journal of Physics* **13**(9): 095009.

Fan, Y., Jacob, K. V., Freireich, B. and Lueptow, R. M. (2017). Segregation of granular materials in bounded heap flow: A review, *Powder Technology* **312**: 67–88.

Fan, Y., Schlick, C. P., Umbanhowar, P. B., Ottino, J. M. and Lueptow, R. M. (2014). Modelling size segregation of granular materials: the roles of segregation, advection and diffusion, *Journal of Fluid Mechanics* **741**: 252–279.

Fan, Y., Umbanhowar, P. B., Ottino, J. M. and Lueptow, R. M. (2015). Shear-rate-independent diffusion in granular flows, *Physical Review Letters* **115**(8).

Gidaspow, D. (1994). *Multiphase flow and fluidization: continuum and kinetic theory descriptions*, Academic press.

Goldschmidt, M., Beetstra, R. and Kuipers, J. (2004). Hydrodynamic modelling of dense gas-fluidised beds: comparison and validation of 3d discrete particle and continuum models, *Powder Technology* **142**(1): 23–47.

Gray, J. M. N. T. and Chugunov, V. A. (2006). Particle-size segregation and diffusive remixing in shallow granular avalanches, *Journal of Fluid Mechanics* **569**: 365–398.

Gray, J. and Thornton, A. (2005). A theory for particle size segregation in shallow granular free-surface flows, *Proceedings of the Royal Society of London A: Mathematical, Physical and Engineering Sciences*, Vol. 461, The Royal Society, pp. 1447–1473.

Gupta, S. D., Khakhar, D. and Bhatia, S. (1991). Axial segregation of particles in a horizontal rotating cylinder, *Chemical engineering science* **46**(5-6): 1513–1517.

Hajra, S. K. and Khakhar, D. V. (2005). Radial mixing of granular materials in a rotating cylinder: Experimental determination of particle self-diffusivity, *Physics of Fluids* **17**(1): 013101.

Hashemnia, K. and Spelt, J. K. (2015). Finite element continuum modeling of vibrationally-fluidized granular flows, *Chemical Engineering Science* **129**: 91–105.

Henann, D. L. and Kamrin, K. (2013). A predictive, size-dependent continuum model for dense granular flows, *Proceedings of the National Academy of Sciences of the United States of America* **110**(17): 6730–6735.

Hill, K. M., Caprihan, A. and Kakalios, J. (1997). Axial segregation of granular media rotated in a drum mixer: Pattern evolution, *Physical Review E* **56**(4): 4386–4393.

Inagaki, S. and Yoshikawa, K. (2010). Traveling wave of segregation in a highly filled rotating drum, *Phys Rev Lett* **105**(11): 118001.

Jiang, Y. and Liu, M. (2003). Granular elasticity without the coulomb condition, *Physical Review Letters* **91**(14).

Johanson, K., Eckert, C., Ghose, D., Djomlija, M. and Hubert, M. (2005). Quantitative measurement of particle segregation mechanisms, *Powder technology* **159**(1): 1–12.

Jop, P., Forterre, Y. and Pouliquen, O. (2006). A constitutive law for dense granular flows, *Nature* **441**(7094): 727–30.

Kamrin, K. (2010). Nonlinear elasto-plastic model for dense granular flow, *International Journal of Plasticity* **26**(2): 167–188.

Kamrin, K. and Koval, G. (2012). Nonlocal constitutive relation for steady granular flow, *Physical Review Letters* **108**(17).

Karlsen, K. H., Lie, K. A., Natvig, J. R., Nordhaug, H. F. and Dahle, H. K. (2001). Operator splitting methods for systems of convectiondiffusion equations: Nonlinear error mechanisms and correction strategies, *Journal of Computational Physics* **173**(2): 636–663.

Ketterhagen, W. R., Curtis, J. S., Wassgren, C. R. and Hancock, B. C. (2008). Modeling granular segregation in flow from quasi-three-dimensional, wedge-shaped hoppers, *Powder Technology* **179**(3): 126–143.

Ketterhagen, W. R., Curtis, J. S., Wassgren, C. R., Kong, A., Narayan, P. J. and Hancock, B. C. (2007). Granular segregation in discharging cylindrical hoppers: A discrete element and experimental study, *Chemical Engineering Science* **62**(22): 6423–6439.

Khakhar, D., McCarthy, J. and Ottino, J. (1997). Radial segregation of granular mixtures in rotating cylinders, *Physics of Fluids* **9**(12): 3600–3614.

Khakhar, D. V. (2011). Rheology and mixing of granular materials, *Macromolecular Materials and Engineering* **296**(3-4): 278–289.

Khakhar, D. V., McCarthy, J. J., Gilchrist, J. F. and Ottino, J. M. (1999). Chaotic mixing of granular materials in two-dimensional tumbling mixers, *Chaos* **9**(1): 195–205.

Khakhar, D. V., McCarthy, J. J., Shinbrot, T. and Ottino, J. M. (1997). Transverse flow and mixing of granular materials in a rotating cylinder, *Physics of Fluids* **9**(1): 31.

Khalilitehrani, M., Abrahamsson, P. J. and Rasmuson, A. (2013). The rheology of dense granular flows in a disc impeller high shear granulator, *Powder Technology* **249**: 309–315.

Khalilitehrani, M., Abrahamsson, P. J. and Rasmuson, A. (2014). Modeling dilute and dense granular flows in a high shear granulator, *Powder Technology* **263**: 45–49.

Khalilitehrani, M., Gomez-Fino, E. M., Abrahamsson, P. J. and Rasmuson, A. (2015). Continuum modeling of multi-regime particle flows in high-shear mixing, *Powder Technology* **280**: 67–71.

Khan, Z. S. and Morris, S. W. (2005). Subdiffusive axial transport of granular materials in a long drum mixer, *Physical review letters* **94**(4): 048002.

Kuo, H., Hsu, R. and Hsiao, Y. (2005). Investigation of axial segregation in a rotating drum, *Powder technology* **153**(3): 196–203.

Lacey and P.M.C. (1954). Developments in the theory of particle mixing, *Journal of Applied Chemistry* **4**: 257–268.

Lanser, D. and Verwer, J. G. (1999). Analysis of operator splitting for advectiondiffusion-reaction problems from air pollution modelling, *Journal of Computational and Applied Mathematics* **111**(1): 201–216.

Liu, P. Y., Yang, R. Y. and Yu, A. B. (2013a). DEM study of the transverse mixing of wet particles in rotating drums, *Chemical Engineering Science* **86**: 99–107.

Liu, P. Y., Yang, R. Y. and Yu, A. B. (2013b). The effect of liquids on radial segregation of granular mixtures in rotating drums, *Granular Matter* **15**(4): 427–436.

Lu, L.-S. and Hsiau, S.-S. (2008). DEM simulation of particle mixing in a sheared granular flow, *Particuology* **6**(6): 445–454.

Lun, C. K. K., Savage, S. B., Jeffrey, D. J. and Chepurniy, N. (1984). Kinetic theories for granular flow: inelastic particles in couette flow and slightly inelastic particles in a general flowfield, *Journal of Fluid Mechanics* **140**: 223C256.

McCathy, J. (1996). Mixing of granular materials in slowly rotated containers, *particle technology and fluidization* .

Metcalfe, G., Shinbrot, T., J.J.McCarthy and M.Ottino, J. (1995a). Avalanche mixing of granular solids, *Nature* .

Metcalfe, G., Shinbrot, T., J.J.McCarthy and M.Ottino, J. (1995b). Avalanche mixing of granular solids, *Nature* **374**.

Montanero, J. M., V., G., Santos, A. and Brey, J. J. (1999). Kinetic theory of simple granular shear flows of smooth hard spheres, *Journal of Fluid Mechanics* **389**: 391–411.

M.Poux, P.Fayolle, J.Bertrand, D.Bridoux and J.Bousquet (1991). Powder mixing: Some practical rules applied to agitated systems, *Powder Technology* **68**: 213–234.

Musha, H., Dong, K., Chandratilleke, G. R., Bridgwater, J. and Yu, A. B. (2013). Mixing behaviour of cohesive and non-cohesive particle mixtures in a ribbon mixer, pp. 731–734.

Nakagawa, M. (1994). Axial segregation of granular flows in a horizontal rotating cylinder, *Chemical Engineering Science* **49**(15): 2540–2544.

Nedderman, R. M. (2005). *Statics and kinematics of granular materials*, Cambridge University Press.

Ng, B. H., Ding, Y. L. and Ghadiri, M. (2009). Modelling of dense and complex granular flow in high shear mixer granulatora CFD approach, *Chemical Engineering Science* **64**(16): 3622–3632.

Nguyen, D., Rasmuson, A., Niklasson Bjorn, I. and Thalberg, K. (2014). CFD simulation of transient particle mixing in a high shear mixer, *Powder Technology* **258**: 324–330.

Orza, J., Brito, R., Van Noije, T. and Ernst, M. (1997). Patterns and long range correlations in idealized granular flows, *International Journal of Modern Physics C* **8**(04): 953–965.

Ottino, J. M. (1990). Mixing, chaotic advection, and turbulence, *Annual Review of Fluid Mechanics* **22**: 207–253.

Ottino, J. M. and Khakhar, D. V. (2000). Mixing and segregation of granular materials, *Annual Review of Fluid Mechanics* **32**: 55–91.

Puri, S. and Hayakawa, H. (2001a). Radial and axial segregation of granular mixtures in the rotating-drum geometry, *Advances in Complex Systems* **4**(04): 469–479.

Puri, S. and Hayakawa, H. (2001b). Segregation of granular mixtures in a rotating drum, *Physica A: Statistical Mechanics and its Applications* **290**(1): 218–242.

Rao, K. K. (2006). Statics and kinematics of granular materials. by r. m. nedderman. cambridge university press, 1992. 352 pp. ?0, *Journal of Fluid Mechanics* **286**: 405–405.

Reis, P. and Mullin, T. (2002). Granular segregation as a critical phenomenon, *Physical Review Letters* **89**(24).

Rosato, A., Strandburg, K., Prinz, F. and Swendsen, R. (1987). Why the brasil nuts are on top: Size segregation of particulate matter by shaking, *Physical Review Letters* **58**: 1038.

Rycroft, C. H., Kamrin, K. and Bazant, M. Z. (2009). Assessing continuum postulates in simulations of granular flow, *Journal of the Mechanics and Physics of Solids* **57**(5): 828–839.

Santos, D. A., Petri, I. J., Duarte, C. R. and Barrozo, M. A. S. (2013). Experimental and CFD study of the hydrodynamic behavior in a rotating drum, *Powder Technology* **250**: 52–62.

Savage, S., Nedderman, R., Tüzün, U. and Houlsby, G. (1983). The flow of granular materials-iii rapid shear flows, *Chemical Engineering Science* **38**(2): 189–195.

Schlick, C. P., Fan, Y., Umbanhowar, P. B., Ottino, J. M. and Lueptow, R. M. (2015). Granular segregation in circular tumblers: theoretical model and scaling laws, *Journal of Fluid Mechanics* **765**: 632–652.

Srivastava, A. and Sundaresan, S. (2003). Analysis of a frictional–kinetic model for gas–particle flow, *Powder technology* **129**(1-3): 72–85.

Steward, R., Bridgwatera, J. and Parkerb, D. J. (2001). Granular flow over a flat-bladed stirrer, *Chemical Engineering Science* .

Stewart, R. L., Bridgwatera, J., Zhou, Y. C. and A.B.Yu (2001). Simulated and measured flow of granules in a bladed mixera detailed comparison, *Chemical Engineering Science* **56**.

Tjakra, J. D., Bao, J., Hudon, N., and Runyu, Y. (2012). Studies of particulate system dynamics in rotating drums using markov chains.

Tjakra, J. D., Bao, J., Hudon, N. and Yang, R. (2013). Collective dynamics modeling of polydisperse particulate systems via markov chains, *Chemical Engineering Research and Design* **91**(9): 1646–1659.

van Beijeren, H. and Ernst, M. H. (1979). Kinetic theory of hard spheres, *Journal of Statistical Physics* **21**(2): 125–167.

Van Noije, T. and Ernst, M. (2000). Cahn-hilliard theory for unstable granular fluids, *Physical Review E* **61**(2): 1765.

Vignal, P., Sarmiento, A., Crtes, A. M. A., Dalcin, L. and Calo, V. M. (2015). Coupling navier-stokes and cahn-hilliard equations in a two-dimensional annular flow configuration, *Procedia Computer Science* **51**: 934–943.

Vun, S., Naser, J. and Witt, P. (2010). Extension of the kinetic theory of granular flow to include dense quasi-static stresses, *Powder Technology* **204**(1): 11–20.

Wakou, J., Brito, R. and Ernst, M. (2002). Towards a landauginzburg-type theory for granular fluids, *Journal of statistical physics* **107**(1): 3–22.

Wang, X., Zhu, H. P., Luding, S. and Yu, A. B. (2013). Regime transitions of granular flow in a shear cell: A micromechanical study, *Physical Review E* **88**(3).

Wang, X., Zhu, H. P. and Yu, A. B. (2012). Microdynamic analysis of solid flow in a shear cell, *Granular Matter* **14**(3): 411–421.

Watson, N., Xu, B. H., Ding, Y., Povey, M. J. W., Reynolds, G. K., Claybourn, M., Weir, S., Nakagawa, M. and Luding, S. (2009). DEM simulation of particle motion in a mipro granulator, pp. 679–682.

Williams, J. (1963). The segregation of powders and granular materials, *Fuel Soc. J* **14**: 29–34.

Yang, R. Y., Zou, R. P. and Yu, A. B. (2003). Microdynamic analysis of particle flow in a horizontal rotating drum, *Powder Technology* **130**(1-3): 138–146.

Yang, R., Yu, A. B., McElroy, L. and Bao, J. (2008). Numerical simulation of particle dynamics in different flow regimes in a rotating drum, *Powder Technology* **188**(2): 170–177.

Zhendong, L., Yangcheng, L., Jiawei, W. and Guangsheng, L. (2012). Mixing characterization and scaling-up analysis of asymmetrical t-shaped micromixer: Experiment and CFD simulation, *Chemical Engineering Journal* **181-182**: 597–606.

Zheng, Q. J. and Yu, A. B. (2015a). Finite element investigation of the flow and stress patterns in conical hopper during discharge, *Chemical Engineering Science* **129**: 49–57.

Zheng, Q. J. and Yu, A. B. (2015b). Modelling the granular flow in a rotating drum by the eulerian finite element method, *Powder Technology* **286**: 361–370.

Zheng, Q. and Yu, A. (2014). Why have continuum theories previously failed to describe sandpile formation?, *Phys Rev Lett* **113**(6): 068001.

Zhou, Y. C., Yu, A. B. and Bridgwater, J. (2003). Segregation of binary mixture of particles in a bladed mixer, *Journal of Chemical Technology and Biotechnology* **78**(2-3): 187–193.

Zhou, Y. C., Yu, A. B., Stewart, R. L. and Bridgwater, J. (2004). Microdynamic analysis of the particle flow in a cylindrical bladed mixer, *Chemical Engineering Science* **59**(6): 1343–1364.

Zhou, Y., Xu, B., Yu, A. and Zulli, P. (2002). An experimental and numerical study of the angle of repose of coarse spheres, *Powder Technology* **125**(1): 45 – 54.

Zik, O., Levine, D., Lipson, S., Shtrikman, S. and Stavans, J. (1994). Rotationally induced segregation of granular materials, *Physical Review Letters* **73**(5): 644–647.